This volume is the property of the University of Oklahoma, but the literary rights of the author are a separate property and must be respected. Passages must not be copied or closely paraphrased without the previous written consent of the author. If the reader obtains any assistance from this volume, he or she must give proper credit in his own work.

I grant the University of Oklahoma Libraries permission to make a copy of my thesis upon the request of individuals or libraries. This permission is granted with the understanding that a copy will be provided for research purposes only, and that requestors will be informed of these restrictions.

NAME [redacted]

DATE 08/02/2012

A library which borrows this thesis for use by its patrons is expected to secure the signature of each user.

This thesis by AVINASH MOHAPATRA has been used by the following persons, whose signatures attest their acceptance of the above restrictions.

NAME AND ADDRESS	DATE

OU-138-2

Downloaded from SHAREOK. Persistent Handle URL: https://hdl.handle.net/11244/51925

UNIVERSITY OF OKLAHOMA

GRADUATE COLLEGE

SEISMIC SIGNATURE OF SEDIMENTARY ROCKS WITH CO_2 FLOODING

A THESIS

SUBMITTED TO THE GRADUATE FACULTY

in partial fulfillment of the requirements for the

Degree of

MASTER OF SCIENCE

By

AVINASH MOHAPATRA
Norman, Oklahoma
2012

UNIVERSITY OF OKLAHOMA LIBRARIES

OU
THESIS
MOH
COP.1

SEISMIC SIGNATURE OF SEDIMENTARY ROCKS WITH CO_2 FLOODING

A THESIS APPROVED FOR THE
MEWBOURNE SCHOOL OF PETROLEUM AND GEOLOGICAL ENGINEERING

BY

[redacted]

Dr. Chandra S. Rai, Chair

[redacted]

Dr. Carl H. Sondergeld

[redacted]

Dr. Deepak Devegowda

© Copyright by AVINASH MOHAPATRA 2012
All Rights Reserved.

This work is dedicated to my beloved parents, younger brother and friends who encouraged me to live life to its fullest.

Acknowledgements

My deep gratitude can never be expressed in mere words to people who were with me to achieve my goal. The least I can do is to thank them to my heartiest.

Foremost, I would like to express my sincere gratitude to my adviser **Dr. Chandra S. Rai** for guiding and inspiring me throughout this study. I am thankful for his consistent support and motivation towards this study with a constant strive of perfection and passion. The vital mix of his caring attitude, immense knowledge and deep patience makes him the best adviser and mentor, anyone can imagine. I always look upto and will try to have a similar outlook on my life and work.

My co-adviser, **Dr. Carl H. Sondergeld** is a man of great vivacity and positive energy. His humor with constructive criticism and scholastic advice kept me in high spirits and exceptional enthusiasm.

I would like to thank my committee member, **Dr. Deepak Devegowda** for his thoughtful suggestions, encouragement and insight comments. He not only helped me with my thesis by also all other aspects of academic life as a professor, a graduate liaison and more important as a friend.

My deep regards to **Mr. Trevor Richards**, without whom this study would have been incomplete and insignificant to industries. I heartily thank him for his cooperation and priority to provide field data for this study.

I would like to thank all members of the **Experimental Rock Physics Consortium** and **Denbury Resources Inc.** for granting access to the cores, providing me the financial support and permitting me to publish my work. I am also grateful to Gary Syowe and Bruce Spears at Integrated Core Characterization Center of the

University of Oklahoma for all help, support and ceaseless demands in setting up the equipment.

My special thanks to my dear friends: Akash, Anita, Atish, Nabanita, Supratik and Sumit who made my stay lovable, memorable and joyful experience.

Last but not least, I would like to thank my lovely parents for all the sacrifices they made for me. I can stride gracefully in this world due to their boundless love, inspiration and affection. I would like to thank my younger little brother Chiranjeevee Mohapatra for his constant support thought out my M.S study. Lastly, I am grateful to God without him nothing can be accomplished.

Table of Contents

Acknowledgements iv

Table of Contents vi

List of Tables ix

List of Figures x

Abstract xvii

1. Introduction 1

1.1 Need for Enhanced Oil and Gas Recovery 1

1.2 Carbon dioxide (CO_2) in enhanced oil recovery process 2

1.3 Seismic as mapping technique 5

1.4 Research objectives and scope of the study 5

1.5 Study area 6

1.6 Synopsis 9

2. Literature Review 10

2.1 Introduction 10

2.2 CO_2 as a complex gas 10

2.3 Seismic as a tool to detect CO_2 13

2.4 Velocity as a function of saturation 17

2.5 Laboratory based velocity as a function of stress and fluids (brine and oil) 18

2.6 Effective pressure law and Biot effective stress coefficient 20

2.7 Experiments on CO_2 23

2.8 Quantification of seismic parameters: Biot-Gassmann theory and Patchy saturation 25

2.9 Digenesis with CO_2 exposure 29

2.10 Study field 31

3. Experimental Procedure 34

3.1 Introduction 34

3.2 Sample preparation 34

3.3 Petrophysical properties 35

3.4 Experiemental set up 37

3.5 Experimental procedure 40

3.6 Sensitivity analysis 44

3.7 4D seismic feasibility study work flow 44

3.8 Precautions 45

4. Results and Observations 47

4.1 Sample and fluid description 47

4.2 Velocity Equilibration study 49

4.3 Velocity variation with effective pressure 52

4.4 Velocity measurements with various fluid fronts 58

4.5 Sensitivity Analysis to velocity estimated using Gassmann equation 75

4.6 Patchy saturation condition 81

4.7 Impedance behavior with various fluid fronts 83

4.8 Application to field data 87

5. Conclusion 92

References 93

Nomenclature 102

Appendix A 105

List of Tables

Table 2.1: n-values for Berea sandstone with water saturation (Christensen and Wang, 1985). 22

Table 2.2: n-value of Berea sandstone with water as pore fluid (Prasad and Manghnani, 1997). 22

Table 4.1: Petrophysical properties of samples chosen for velocity equilibration and effective pressure study. 47

Table 4.2: Geological characteristics of the arrived core interval (courtesy: Denbury Resources) 47

Table 4.3: Petrophysical properties of Tuscaloosa formation 48

Table 4.4: Density and bulk modulus of formation brine, formation oil and CO_2 used in our experiments 49

Table 4.5: Influence of differential pressure on n-values for gaseous and liquid CO_2 in Berea sandstone. 55

Table 4.6: n-values as function of differential pressure and CO_2 phase for Tuscaloosa sandstone. 55

Table 4.7: P- Impedance change with different flooding scenarios at effective pressure of 1500 psi. 85

Table 4.8: S- Impedance change with different flooding scenarios at effective pressure of 1500 psi. 86

List of Figures

Figure 1.1: Top 10 states in terms of number of stripper wells (DOE, 2011) 1

Figure 1.2: Histogram of EOR production using CO_2 from 1972 to 2008 shows increasing trend (NETL, 2010) 2

Figure 1.3: The potential area for EOR recovery in United States (Hovorka & Tinker, 2010) 3

Figure 1.4: The process of CO_2 flooding in the reservoir (NETL, 2010). 4

Figure 1.5: Geographic location of Delhi field 7

Figure 1.6: The 3D seismic area acquired over Delhi field in 2008 (in blue) and 2010 (in red). The overlapped area becomes the 4D seismic, the difference map between the two 3D seismic surveys. A mini 3D survey (shown in brown) was recorded in 2010 (Richards, 2011). 8

Figure 1.7: The Paluxy amplitude difference created between 2010 (post CO_2 flooded) and 2008 (pre CO_2 flooded) survey. The red triangles show the injector wells and the red circles shows producing wells. The map shows low impedance near the injector well shown in yellow and high impedance near producing wells in blue (Richards, 2011). ... 8

Figure 2.1: The carbon dioxide (CO2) phase diagram (Shakhashiri, 2008). 11

Figure 2.2: Influence of reservoir pressure and temperature on CO_2 displacement mechanism (Klims, 1953; Bui, 2010) 12

Figure 2.3: Schematic diagram of Seismic reflections (EPA, 2011) 14

Figure 2.4: The interface between formation of different density and velocity. 15

Figure 2.5 Time lapse 4D seismic map showing CO_2 signature at Midale-Weyburn field, Canada ongoing CO_2 EOR (White, 2009). 16

Figure 2.6: The 4D Time lapse showing change in CO_2 saturation (from 2001 to 2008) at Sleipner CO_2 storage operation (Chadwick et al., 2010). 17

Figure 2.7: The methodology to calculate numerator and denominator of second term of equation 2.3 (Hofmann et al., 2005). 21

Figure 2.8: Range of n-values for water saturated Berea sandstone (Hornby, 1996). 23

Figure 2.9: Decrease in n values with differential pressure in oil saturated sandstone (Siggins and Dewhurst, 2003). 23

Figure 2.10: (left) Sample and transducer set up for the experiment performed by Xue and Ohsumi, 2004. 24

Figure 2.11: Modeled P and S-wave velocities of water saturated rock with ongoing CO_2 flooding (Vanorio et al., 2010). 29

Figure 2.12: The SEM images of pre and post-flooded CO_2 to observe the geochemical effect in Fountainebleau sandstone (Vanorio et al., 2010) 31

Figure 2.13: The geographic location of Delhi field 32

Figure 2.14: 3D seismic surveys acquired over Delhi field at different times. The blue outlined is the region of Nov 2008 survey, red outline corresponds to Mar 2010 survey and pink color region shows Jan 2010 survey. Richards, 2011 used 2010 and 2008 survey to create amplitude difference map (refer Fig 2.15) 32

Figure 2.15: Amplitude difference in Paluxy horizon by subtracting June 2010 survey from 2008 survey. The red triangles correspond to CO_2 injector wells and red circles correspond to producing wells. The low to high amplitude difference region is colored as blue and red respectively (Richard, 2011). 33

Figure 3.1: AP608 (left) and HPP (right) equipments used to measure porosity. 35

Figure 3.2: Infrared spectra of the common minerals found in the sedimentary rocks (Sondergeld and Rai, 1993) 36

Figure 3.3: a) and b) showing the actual sample transducer assembly and its detailed inside picture respectively. 38

Figure 3.4: The compressional waveforms (a) and shear waveforms (b) showing poor quality signal with the Tuscaloosa sandstone using titanium endcaps. 38

Figure 3.5: Significant improvement in the signal quality with the use of peek endcaps mounted transducer. 39

Figure 3.6: Photograph of experimental set up used for velocity measurements. 39

Figure 3.7: Schematic diagram of the experimental set up. Both P and S-velocity can be measured with various pore and confining pressure using different saturants 40

Figure 3.8: The confining pressure (blue) and pore pressure (red) varying with time. Velocities were measured simultaneously along these pressures 41

Figure 3.9: The confining pressure and pore pressure points (black nodes) were chosen to maintain constant differential pressure intervals (written in colored) 42

Figure 3.10: The selected confining (blue), pore pressure (red) and saturation (brown) points at which seismic velocities are measured. The pore and confining pressure are chosen based on the insitu pressure conditions in Hot Bryant Basin and insitu fluids are used for saturation purposes 43

Figure 3.11: Blocked density, V_P and V_s logs as function of time (ms) and depth (ft).. 45

Figure 4.1: Porosity as function of pressure for plugs collected from various depths. .. 48

Figure 4.2: Compressional and Shear wave velocity in glass bead sample saturated with gaseous (blue square) and Liquid (red diamond) CO_2 50

Figure 4.3 Measured P (i) and S (ii) wave velocity equilibrating with gaseous CO_2 (blue) and liquid state CO_2 (red) in Berea sandstone. 51

Figure 4.4: Calculated bulk and shear moduli of Berea sandstone calculated from Biot-Gassmann theory 52

Figure 4.5: P (i) and S (ii) wave velocity measurements for varying confining and pore pressure for Berea sandstone. 53

Figure 4.6: P (top) and S wave velocity as function of effective pressure on Tuscaloosa sandstone 54

Figure 4.7: Measured Vp (i) and Vs (ii) values (shown in filled symbols) along with predicted Vp (i) and Vs (ii) values (shown in open symbols) as a function of confining and pore pressure in Berea sandstone. 57

Figure 4.8: Measured Vp (i) and Vs (ii) values (shown in filled symbols) along with predicted Vp (i) and Vs (ii) values (shown in open symbols) as a function of confining and pore pressure in Tuscaloosa sandstone. 58

Figure 4.9: Measured P and S velocity (blue) along with calculated bulk density (grey) as a function of brine saturation for sample XX26.6 ft 59

Figure 4.10 Measured P and S velocity (red) for sample XX26.6 ft along with calculated bulk density (grey) variation when formation oil replaces formation brine. 60

Figure 4.11 Measured P and S velocity (green) along with calculated bulk density (grey) variation when liquid CO_2 displaces oil for sample XX26.6 ft. 61

Figure 4.12: Experimental (filled) and theoretical (open) P and S wave velocity data as a function of brine saturation for sample XX26.6 ft 62

Figure 4.13 Experimental (filled) and theoretical (open) P and S wave velocity data as a function of brine saturation with oil displacing brine scenario for sample XX26.6 ft... 63

Figure 4.14: Experimental (filled) and theoretical (open) P and S wave velocity data as a function of liquid CO_2 saturation oil saturated for sample XX26.6 ft. 64

Figure 4.15: Experimental (filled) and theoretical (open) P and S wave velocity data as a function of brine saturation for sample XX58 ft. 66

Figure 4.16: Experimental (filled) and theoretical (open) P and S wave velocity data for sample XX58 ft as oil replaces water 67

Figure 4.17: Experimental (filled) and theoretical (open) P and S wave velocity data as a function of liq. CO_2 saturation oil saturated for sample XX58 ft. 68

Figure 4.18: Experimental (filled) and theoretical (open) P and S wave velocity data as a function of brine saturation for sample XX78 ft 69

Figure 4.19: Experimental (filled) and theoretical (open) P and S wave velocity data for sample XX78 ft as oil replaces brine 70

Figure 4.20: Experimental (filled) and theoretical (open) P and S wave velocity data as a function of liq. CO_2 saturation for oil saturated sample XX78 ft 71

Figure 4.21: Experimental (filled) and theoretical (open) P and S wave velocity data as a function of brine saturation for sample XX83.5 ft. 72

Figure 4.22: Experimental (filled) and theoretical (open) P and S wave velocity data for sample XX83.5 ft as oil replaces brine 73

Figure 4.23: Experimental (filled) and theoretical (open) P and S wave velocity data as a function of liq. CO_2 saturation for oil saturated sample XX83.5 ft. 74

Figure 4.24: Sensitivity analysis of predicted Vp to porosity with three flooding scenarios on sample XX78 ft..... 77

Figure 4.25: Sensitivity analysis of predicted Vp fluid bulk moduli with three flooding scenarios for sample XX78 ft..... 78

Figure 4.26: Sensitivity analysis of pred. Vp to fluid density with three flooding scenarios on sample XX78 ft..... 79

Figure 4.27: The patchy modeled P wave velocity (dotted) calculated using patchy model (Eq. 2.6) is better correlated to the experimental values in CO_2 flooding scenario. 81

Figure 4.28: The P and S impedance for all four samples calculated in Brine flooding scenario..... 84

Figure 4.29: The P and S impedance for all four samples calculated in oil flooding scenario..... 84

Figure 4.30: The P impedance for all four samples calculated in liquid CO_2 flooding scenario. Best fit line with R^2 of more than 0.9 is determined using linear regression analysis..... 85

Figure 4.31: Field pre-flooded and post-flooded Vp and Vs logs..... 87

Figure 4.32: Ricker wavelet of 60 Hz frequency and 120 ms length used to create Aki Richard synthetic seismogram..... 89

Figure 4.33: Seismic amplitude difference as function of offset and CO_2 saturation for reflection from Tuscaloosa and Paluxy interfaces. The base case is pre CO_2 flood condition when the formation is saturated with oil and water..... 89

Figure 4.34: Lab based AVO analysis created for different fluid and rock scenarios in Tuscaloosa (i) and Paluxy (ii) formation 91

Figure A.7.1 Measured V_p and V_s equilibrating with gaseous CO_2 (blue) and liquid state CO_2 (red) in coal. The V_p and V_s, shown with dotted line, are predicted from dry measurements. 105

Figure A.7.2: Measured P (i) and S (ii) wave velocity equilibrating with gaseous CO_2 (blue) and liquid state CO_2 (red) in Woodford shale 106

Abstract

Surface seismic offers a promising technique to monitor CO_2 flood fronts during enhanced oil recovery process. Changes in seismic signature have been observed with CO_2 flooding but quantification of the seismic signature with respect to subsurface saturation is still in its infancy. The model currently used in industries for fluid quantification are either non-linear or inappropriately describe the rock-fluid system undergoing CO_2 flooding. This study is focused on quantification of the variation in seismic parameters (velocity and impedance) with the change in subsurface fluid type and saturation.

In order to achieve this objective, velocity equilibration study is performed to understand the time required for liquid CO_2 to equilibrate in pores. This is followed by experiments to observe the influence of effective pressure on velocity. The outcomes of the above experiments determined some of the parameters for flooding experiments.

The results of the flooding experiments are presented where velocity and density were monitored as the pore fluids (formation brine and oil, and CO_2) are replaced sequentially. All the experiments were performed at *in-situ* pressure conditions on plugs (Tuscaloosa sandstones) recovered from a well in a field currently undergoing CO_2 flooding. The plugs used are characterized as fluvial (quartz~87%, clay~10%) and distributary channels (quartz~75%, clay~17%).

During brine flooding on dry samples, a decrease in P-wave velocity (~2%) was observed till 95% saturation and thereafter the velocity increases by 15% during the remaining 5% saturation. After attaining 100% brine saturation, oil was pumped to displace brine till irreducible water saturation was achieved. A linear drop of 4% in

velocity was observed during this step. Liquid CO_2 was injected to displace oil-brine system and a drop of 8% in P-velocity was observed. Associated changes in P-wave impedance due to change in pore fluid saturation were observed to be 25%, -5% and -8% respectively for the three flooding experiment. Biot-Gassmann modeling showed good agreement with experimental results for gas-brine and oil-brine system but not for liquid CO_2 flooding. However, the CO_2 flooding experimental data validated patchy model. Apart from patchy model, an empirical correlation is developed that can be used directly to convert seismically interpreted pre and post flooded impedance data to CO_2 saturation.

Using the patchy model and empirical correlation, the fluid substitution on field pre-flooded logs quantified the CO_2 saturation. Based on the pre flooded base and empirically CO_2 substituted logs, a synthetic seismic difference was generated as a function of CO_2 saturation to study the 4D seismic signature and AVO response to CO_2 saturation.

Chapter 1 Introduction

1.1 Need for Enhanced Oil and Gas Recovery

In 2011, U.S. Department of Energy published that 90% of the wells in oil producing states (filled with red in Fig. 1.1) are nearing their end of its economical useful. In such situation, enhanced oil recovery (EOR) techniques play critical role by extending the life of an existing field. Advanced Resources International in 2005 estimated that 400 billion barrels of oil in excess can be produced through EOR techniques out of 1124 billion barrels of undeveloped oil in place.

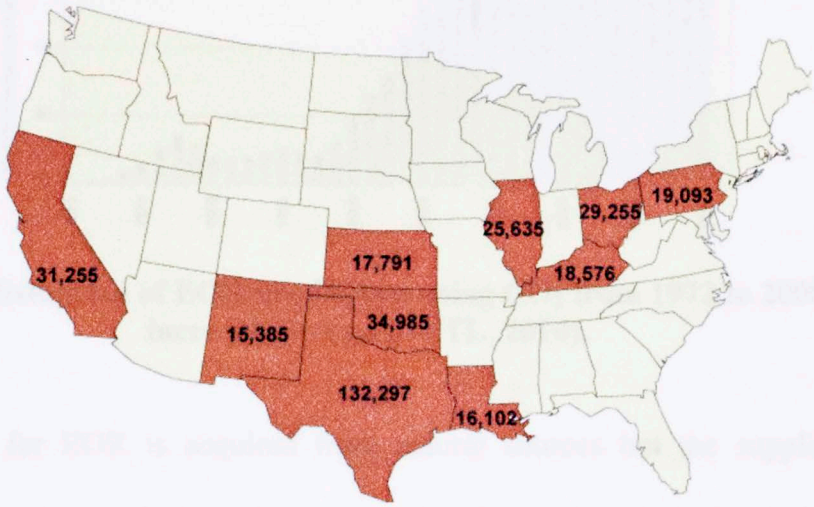

Figure 1.1: Top 10 states in terms of number of stripper wells (DOE, 2011)

There are many EOR techniques that are being adopted based on the reservoir characteristics, reservoir fluid properties, availability of the flooding fluid and economics. One of the forthcoming techniques is CO_2 –EOR technique. Apart from CO_2-EOR technique, other available techniques are water flooding, steam flooding, *in-situ* combustion etc. These techniques have their own merits and demerits; however,

because of the dual benefits from CO_2-EOR i.e. additional oil recovery and CO_2 sequestration, it is one of the most favored methods.

1.2 Carbon dioxide (CO_2) in enhanced oil recovery process

A histogram, shown in Fig. 1.2., depicts the increasing trend of oil production from 1972 till 2008 using CO_2 in EOR (NETL, 2010). A vast uninterrupted CO_2 source is required to meet such increasing demand.

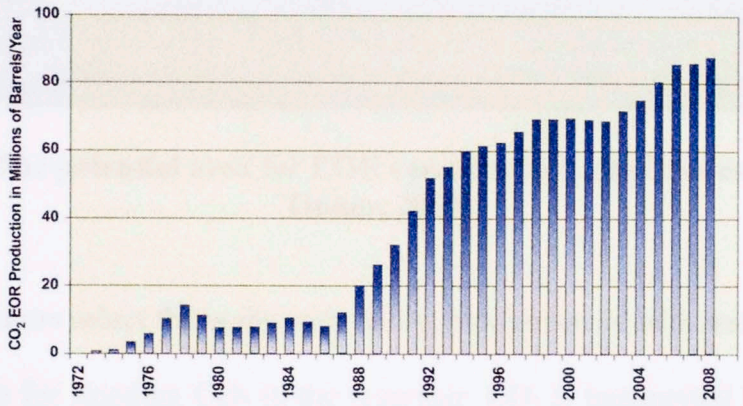

Figure 1.2: Histogram of EOR production using CO_2 from 1972 to 2008 shows increasing trend (NETL, 2010).

Currently, CO_2 for EOR is acquired from natural sources but the supplies can be increased by trapping emissions from the industries and power plants. In the US, approximately 70% of the electricity comes from power plants driven by fossil fuels (IEA, 2012) and they are responsible for emitting 2.3 billion tons of CO_2, in 2009 (EIP, 2011). This emitted greenhouse gas, with proper planning and technology, can be utilized for enhancing oil and gas production in the nearby stripper wells (Fig.1.3).

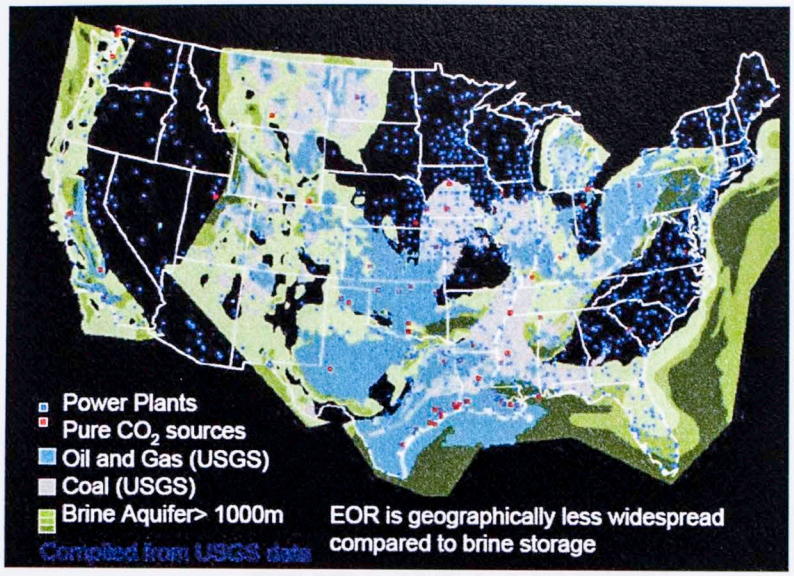

Figure 1.3: The potential area for EOR recovery in United States (Hovorka & Tinker, 2010)

Generally, operators select the wells with failing production or with water breakthrough as injector wells for flooding CO_2 in the reservoir. CO_2 is transported through pipeline to the injector wellhead installation from a CO_2 source. The CO_2 source is either a natural pool (more often) or industrial effluent (rarely used). Pressurizing units, such as compressors, compress the gaseous CO_2 and convert it into liquid state. This liquid CO_2 is injected in the subsurface reservoir which provides a pressure drive to liquid hydrocarbon to the surface through a production well (Fig 1.4).

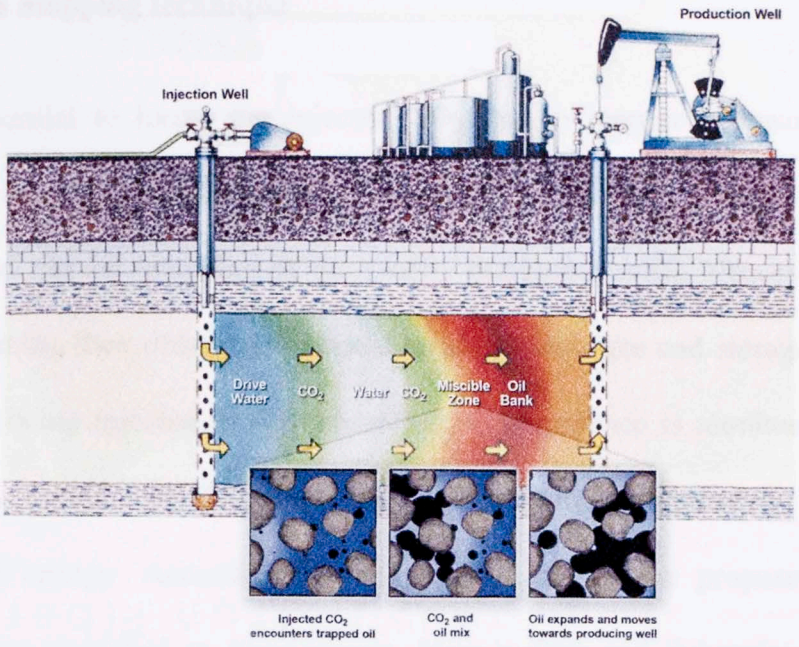

Figure 1.4: The process of CO_2 flooding in the reservoir (NETL, 2010).

Apart from exerting a pressure drive, the liquid CO_2 forms a miscible phase with the reservoir fluid present in the pores and thus decrease the density and viscosity of the fluid. Thus, increases the mobility of the fluid. It also results in decrease of surface tension between the fluid and grain surface which decreases the capillary pressure. Reservoir fluids thus seep out of the thin pores due to decrease in capillary pressure. It is also observed that some rock matrix (like coal, clays etc.) has higher affinity towards absorbing liquid CO_2. This shift in affinity from former existing reservoir fluid to liquid CO_2, discharge more reservoir fluids while trapping the liquid CO_2. This is also a factor which is responsible for existence of methane front before CO_2 flood front in the gas reservoir. The typical flood front pattern (as shown in Fig 1.4) consist of oil front, water front, miscible zone, methane front and liquid CO_2 in series.

1.3 Seismic as mapping technique

It is very essential to locate the injected CO_2 due to numerous reasons. For EOR purposes, locating CO_2 will assist in determining the area swept, oil recovery, production and history matching of the nearby producing wells. However, in case of CO_2 sequestration, then obtaining information about leakages and storage is the prime motive. After being injected in the subsurface, CO_2 presence is monitored by several techniques as defined by National Energy Technology Laboratory (NETL), US department of energy. According to NETL 2009 report, the proposed monitoring techniques were classified as Atmospheric, Near-surface and Subsurface Monitoring. Atmospheric monitoring technique detects the increased amount of CO_2 in the atmosphere column near the surface right above the CO_2 flooded reservoir. It is economical and effective to detect leakages, however, quite inefficient to map the CO_2 flood front in absence of leakages. Near surface monitoring techniques, on the other hand, locate the topographic, chemical and potential differences on the surface. Subsurface monitoring is the technique by which CO_2 can be detected deep in the reservoir using sensors sensitive to CO_2 presence. Among all the monitoring and mapping technologies, surface seismic offers a promising technique to monitor the CO_2 flood front remotely in the subsurface over a large area. Seismic data can provide high quality information on CO_2 distribution and migration in the subsurface.

1.4 Research objectives and scope of the study

A number of authors have reported seismic signature associated with CO_2 flooding but quantification of the seismic signature with respect to subsurface saturation is still in its

infancy. Also, they are unable to detect low CO_2 concentration, mineral trapped CO_2 and usually encounter low signal to noise ratio (NETL, 2009).

This study is primarily focused on quantification of variations in the seismic parameters (velocity and impedance) with the change in subsurface fluid type and saturation. This quantitative analysis based on laboratory measurements will be used to interpret and calibrate 4D seismic data set acquired over the region. Petrophysical measurements of the samples were performed before CO_2 flooding. Laboratory scale ultrasonic velocity was measured with three flooding scenarios in series. The different fluids used in experiments for flooding are formation brine, formation oil and research grade liquid CO_2. The experiment creates an understanding of velocity behavior with different fluids, their saturation and effective pressure. Later, these form a basis for analyzing well logs and 3D seismic survey acquired with the purpose of mapping CO_2 flood front. Post flooded synthetic sonic log of a CO_2 injector is generated from pre-flooded sonic logs using fluid substitution model and laboratory measurements. Empirical and theoretical correlations are evaluated using these measurements. The modeled sonic log, generated by substituting CO_2, is correlated and compared with the actual post flooded sonic log.

1.5 Study area

The study was performed on Tuscaloosa and Paluxy sandstones cored from a well placed in reservoir 'Holt-Bryant zone' at Delhi field, Louisiana State (Fig. 1.5). The core was taken from 3204 to 3285 ft of the Delhi field, located at the updip limit of the Tuscaloosa producing trend. This 84 ft core was divided into 6 units based on the

depositional environment i.e. fluvial channel, distributary mouth bar and estuary/distributary mouth channel.

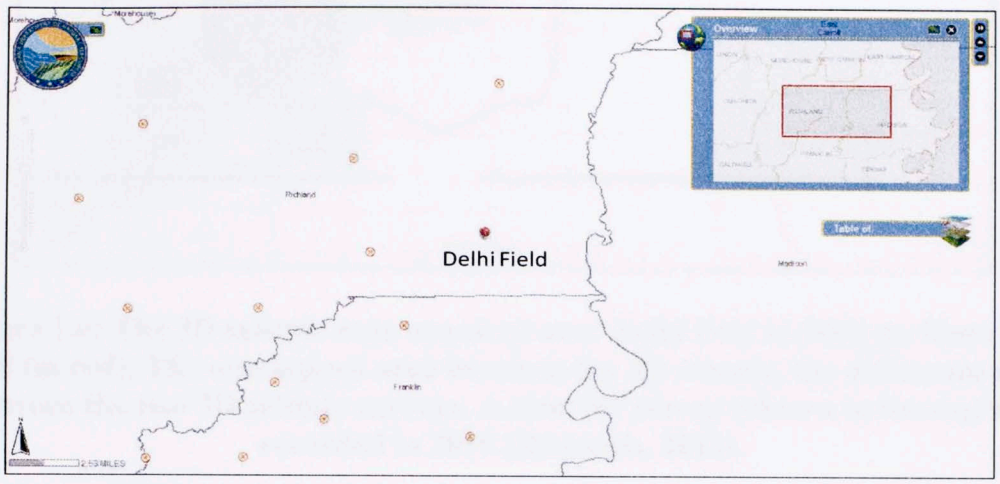

Figure 1.5: Geographic location of Delhi field

A detailed look of the Delhi field is shown in Fig. 1.6. The outlined area shows the regions where seismic data was acquired. Richards, 2011 described this field seismic survey in which he mentioned the manner in which 3D seismic survey and logs were taken in a sequence to map injected CO_2. In the Fig 1.6., Blue region shows the 2008 acquired 3D seismic survey area on the part of reservoir which was flooded with water in 1953. In 2010, 3D Seismic survey was acquired again over the other part of field outlined in red in Fig 1.6.

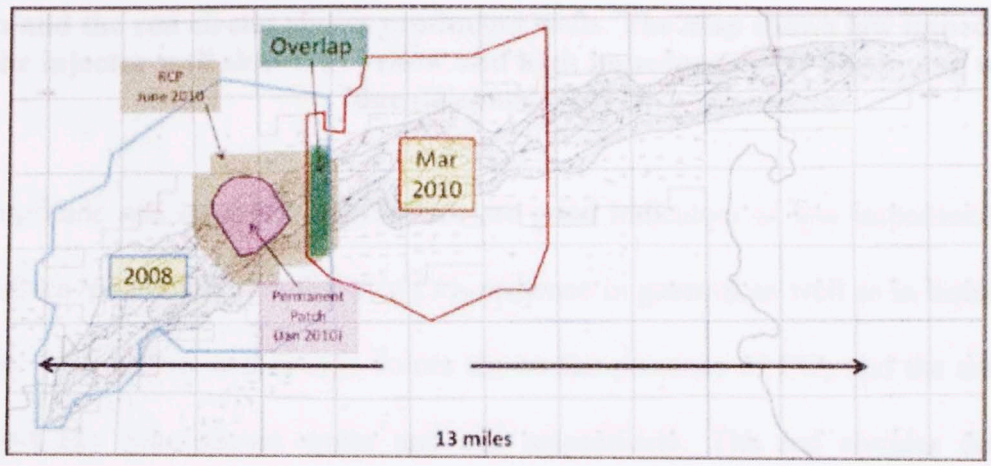

Figure 1.6: The 3D seismic area acquired over Delhi field in 2008 (in blue) and 2010 (in red). The overlapped area becomes the 4D seismic, the difference map between the two 3D seismic surveys. A mini 3D survey (shown in brown) was recorded in 2010 (Richards, 2011).

A small 3D seismic survey was acquired in Jan, 2010 and was compared with the 2008 3D seismic survey to observe the CO_2 flood front and its presence. An amplitude difference map as shown in Fig 1.7 was created by subtracting 2008 3D seismic amplitude from 2010 3D seismic amplitude, also known as Paluxy amplitude difference (Richards, 2011).

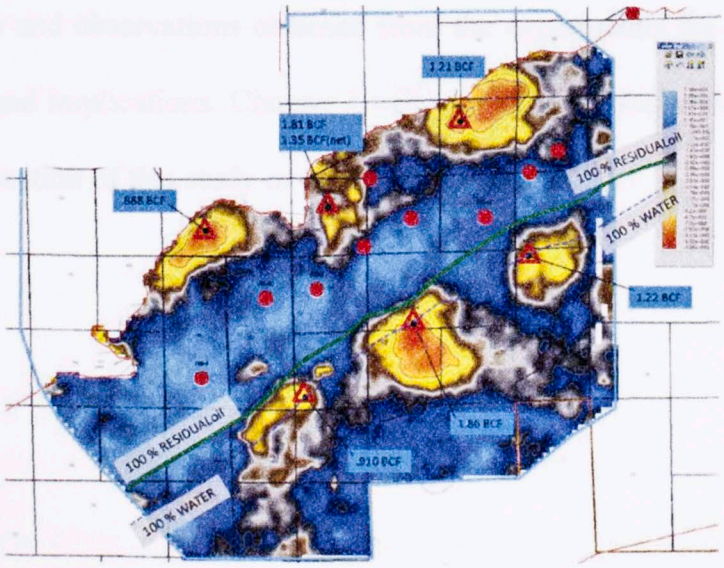

Figure 1.7: The Paluxy amplitude difference created between 2010 (post CO_2 flooded) and 2008 (pre CO_2 flooded) survey. The red triangles show the injector

wells and the red circles shows producing wells. The map shows low impedance near the injector well shown in yellow and high impedance near producing wells in blue (Richards, 2011).

The amplitude and impedance difference are good indicators of low impedance zones which gives qualitative possibility of CO_2 presence in gaseous as well as in liquid state. The area with yellow and orange colors shows the presence of CO_2 and the area with navy and sky blue shows water and oil, respectively. The red circular dots and triangular symbols are producers and CO_2 injector respectively. The grey colored region gives some indication of the direction of CO_2 flood front. A detailed description is provided in Chapter 2.

1.6 Synopsis

This study is divided in 6 chapters. Chapter 1 is about introducing CO_2 EOR, its significance and detection using seismic velocity. A review of relevant previous literature is mentioned in Chapter 2. Chapter 3 comprises a detailed description of experimental set up and procedure adopted to demonstrate the objective of this study. In Chapter 4, results and observations obtained from the experiments are discussed along with its features and implications. Chapter 5 will conclude this study with some critical remarks and application of this study in the 3D/4D seismic survey.

Chapter 2 Literature Review

2.1 Introduction

Carbon dioxide enhanced oil recovery (CO_2-EOR) is the tertiary oil recovery technique and was patented by Whorton et al in 1952. The first application of the CO_2-EOR technique was showcased on one of the largest U.S oil fields in Scurry County, Texas (DOE, 2011) in 1972. The merits of CO_2 as an EOR agent was well known back in 1970's as discussed by Holm and Josendal, 1972. When CO_2 is injected in to an oil reservoir, it is responsible for the swelling of oil, increase in oil density and decrease in oil viscosity. It is also corrosive to rock and is found to affect clay minerals (Barclay and Worden, 2000; Kharaka et al., 2006; Benson and Cole, 2008). In this Chapter, we will review the previous efforts of authors that helped us to understand the complex nature of CO_2, seismic mapping of fluid (water and liquid CO_2) flood, velocity effective pressure relationships, application of Biot-Gassmann theory and rock alterations to CO_2 exposure.

2.2 CO_2 as a complex gas

CO_2 is a gas of complex nature because of its properties and phases at which it exist. CO_2 phase behavior as a function of temperature and pressure is shown in Fig 2.1. CO_2 exist as gas at N.T.P. CO_2 as gas is slightly heavier and denser than air.

At temperature and pressure more than critical point (>31.1 ^{o}C and/or >1070 psi); CO_2 attains supercritical state. This state is somewhere in between gaseous and liquid state characterized by high density (like liquid) but low viscosity fluid of high volume (like gas). At lower temperature, CO_2 turns into liquid state above critical pressure, while at lower pressure it exists as gas.

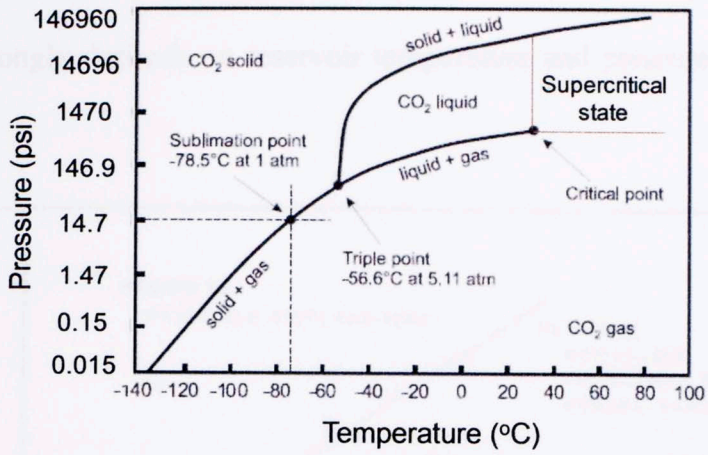

Figure 2.1: The carbon dioxide (CO2) phase diagram (Shakhashiri, 2008).

For the purpose of enhanced oil and gas recovery and CO_2 sequestration, CO_2 is pressurized and injected in its liquid state into the reservoir, usually below 800 m, via an injector well. Due to higher pressure and temperature in the reservoir, CO_2 converts into supercritical state.

In addition to mentioned physical complexity, CO_2 is a dispersive medium for ultrasonic velocities (Dean, 1979) in all its phases. At high frequencies, CO_2 presence may induce two frequency notes (high and low frequency notes) in the energy pulse. This early arrival of high frequency is responsible for the higher velocity of the pulse when a dispersive phase like CO_2 is encountered. In addition to dispersion, liquid CO_2 has high mobility as its viscosity is similar to that of gas. The high mobility characteristics may give rise to viscous fingering of liquid CO_2 in oil or brine saturated reservoir. Viscous fingering arises due to instability of the interface between the fluids of different viscosities and densities.

One of the driving mechanisms in CO_2 EOR is due to CO_2 miscibility with oil or brine. Its miscibility strongly depends on reservoir temperature and pressure as shown in Fig 2.2.

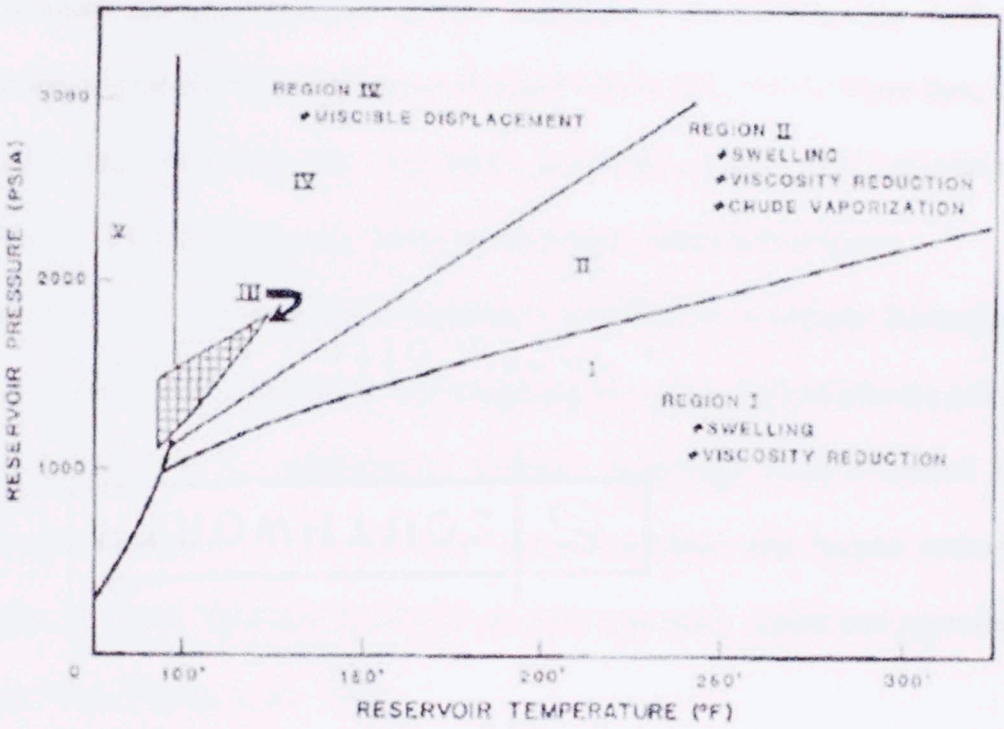

Figure 2.2: Influence of reservoir pressure and temperature on CO_2 displacement mechanism (Klims, 1953; Bui, 2010)

For a wide range of reservoir, region III and IV are more likely to prevail on the miscibility properties. The curves in Fig 2.2 may shift which depend on oil properties. In these regions, CO_2 entraps oil components via multiple contact miscibility, which requires rapid condensation and vaporization of oil in CO_2 phase and vice versa. Therefore, the interpreting seismic data poses a challenge which includes such complexity of CO_2 properties.

2.3 Seismic as a tool to detect CO_2

2D seismic survey was first used in search operations for sunken ships by Canadian inventor R. Fessenden and then later applied in tracing submarines in World War I. He later patented his invention for seismic exploration in 1917, giving birth to the application of seismic for oil and gas exploration (Fessenden, 1917). Since then, seismic technology has come a long way, developed, and improved even to 3D seismic and 4D seismic (repetition of 3D seismic survey in time lapse mode) technologies.

This technology is widely used as a qualitative indicator of oil and gas. Recently, it has found its application in monitoring and mapping CO_2, when injected into the subsurface either for CO_2 EOR or sequestration. Seismic technology plays a critical role in Reservoir management, which involves using technology and human resources to maximize economic recovery of oil and gas with minimum capital and operating cost (Thakur, 1996; Lumley et al., 2003).

In this technology, a seismic pulse is generated on the surface by near surface explosions, mechanical impact, or vibrations. It travels through the subsurface and is either reflected or refracted from interfaces between formations of different physical properties. The arrays of geophones on the surface (or hydrophones on the ocean surface) are placed nearer to the source than the depth of the reflecting layer (Fig. 2.3). They record the times the reflected waves take to reach the surface from the reflecting layers. The variations in the reflection time with the offset (distance of the geophones from the source) are analyzed to indicate the structural features in the subsurface strata (Dobrin and Savit, 1988).

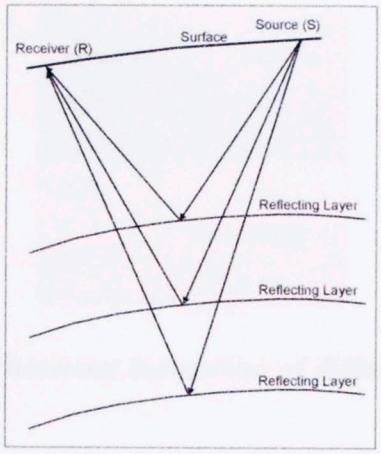

Figure 2.3: Schematic diagram of Seismic reflections (EPA, 2011)

The refracted data also provides the velocity of the refracting bed after it is separated from the reflected data during processing. Therefore, the reflected and transmitted seismic data is used not only to define the strata (includes geobody, reefs, salt domes, faults etc.) but also reflection coefficients and attenuation characteristics. Based on the velocity, the reflected and refracted data can indicate lithology, hydrocarbons, aquifer, reservoir characteristics etc.

Seismic reflection data is sensitive to fluid present in the subsurface. Various seismic attributes are used as an indicator and one of them is seismic reflection amplitude. Reflection coefficient is the magnitude of the seismic reflection amplitude between the layers, which is given by:

$$R = \frac{\rho_2 V_2 - \rho_1 V_1}{\rho_2 V_2 + \rho_1 V_1} \; or \; \frac{Z_2 - Z_1}{Z_2 + Z_1}$$

Where: $\rho_1$and ρ_2 are the densities of the top and bottom layer respectively and V represents velocity in the layer (Fig 2.4). Z represents the acoustic impedance (Dobrin and Sevit, 1988).

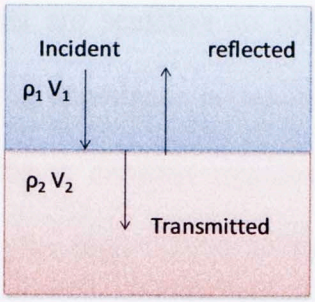

Figure 2.4: The interface between formation of different density and velocity.

It is clear that change in velocity and density will change the reflection coefficient indicating the dependence of seismic reflection amplitude on rock and fluid properties. Therefore, it is important to understand the seismic signature with fluid and its saturation in the pore spaces of rock using laboratory experiments and theory based models.

Several examples of field and theoretical generated seismic parameters have been published which are interpreted on reservoir rock saturated with fluids such as brine, oil or CO_2. Weyburn-Midale field is one of the sites where CO_2-EOR and CO_2 storage related research is in focus (Davis et al., 2003; Jinfeng and Morozov, 2010). The Fig 2.5 shows the amplitude difference of 3D seismic maps of the field ongoing CO_2 EOR (White, 2009). The green and black lines show injector and producer wells, respectively. The increasing trend of low impedance patches (yellow) indicates the location and flood front of CO_2.

A study, done on Sleipner field CO_2 storage operation by Arts et al. (2004), showed enhanced reflectivity in the amplitude map which is due to higher compressibility of the CO_2. Chadwick et al. (2010) published the time lapse seismic maps of this field showing the change in total reflection amplitude with CO_2 saturation in Fig 2.6.

3D or 4D seismic measurements are sensitive to rock matrix frame and pore fluid properties. Often a high contrast in impedance is required to favor the fluid detection in seismic survey. A good impedance contrast requires a high porosity and a weak modulus rock. High porosity implies high volume of fluid and low modulus frame will enhance the seismic capability to detect fluid type (Lumley, 2010). Based on such rock physics concepts, rock models are created and applied in seismic study for accurate fluid detection and saturation.

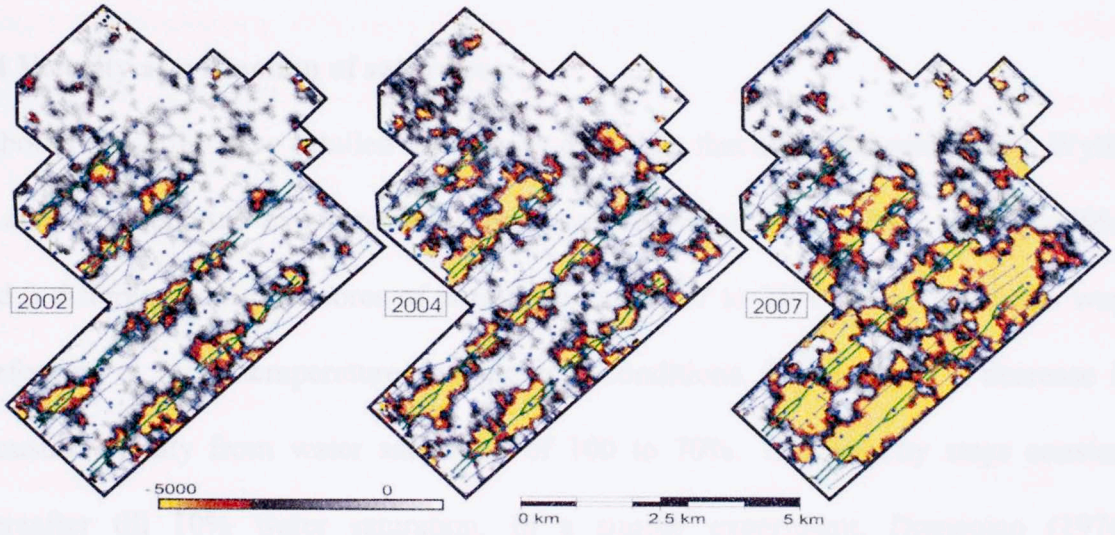

Figure 2.5 Time lapse 4D seismic map showing CO_2 signature at Midale-Weyburn field, Canada ongoing CO_2 EOR (White, 2009).

Urosevic et al. (2010) calculated significant change in acoustic impedance when fluid is replaced by CO_2. Numerical simulation using Biot-Gassmann equations shows change of 3-6% is observed due to intrusion of CO_2.

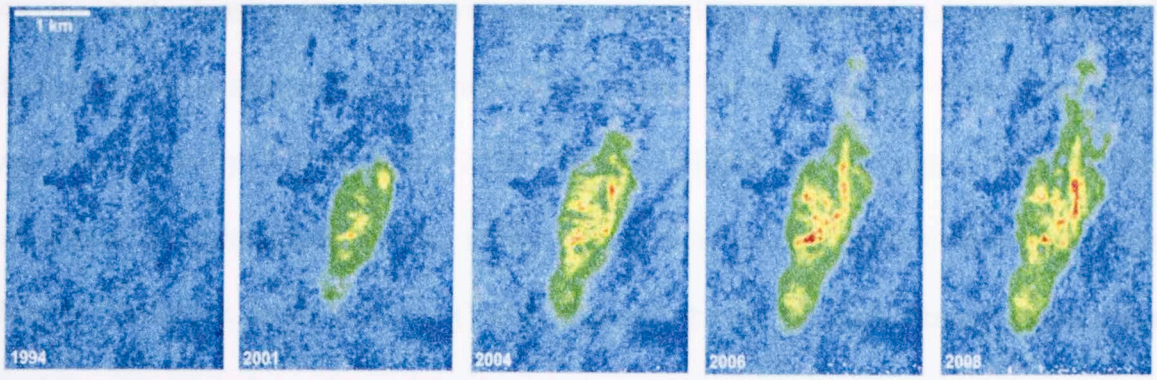

Figure 2.6: The 4D Time lapse showing change in CO_2 saturation (from 2001 to 2008) at Sleipner CO_2 storage operation (Chadwick et al., 2010).

2.4 Velocity as a function of saturation

Laboratory studies give detailed description of factors that affect seismic waves. Wyllie et al., 1956 reported experimentally measured velocities on alundum (porosity-40%) and 3 different sandstone cores of porosity between 17 to 25%. The experiments were performed at room temperature and pressure conditions. He observed a decrease in acoustic velocity from water saturation of 100 to 70%. The velocity stays constant thereafter till 10% water saturation. In a similar experiment, Domenico (1976) measured P and S wave velocity with brine saturation on an unconsolidated Ottawa sand (porosity of 38%). He observed a non linearity in the measured P wave velocities with saturation. Unlike Wyllie, he reported constant velocity till water saturation of 85%.

Domenico's results suggest that the velocities, besides saturation, also depend on the details of distribution and geometrics of pore fluid phases. In 1990, Knight and Hoeksema published their velocity (both Vp and Vs) measurements with water saturation based on imbibition/drainage experiments.

As the bulk density increases with brine saturation, compressional velocity (Vp) decreases until a saturation point near 100% where Vp rises steeply. This observation was also made by Wyllie et al. (1956), Murphy (1982) and Domenico (1976). This increase in compressional velocity is due to pore fluid compressibility dominance over density. However, shear velocity (Vs) is dependent only on bulk density since shear modulus remain independent of fluid saturation (Biot, 1956, Berryman, 1999). Increase in bulk density decreases the shear velocity.

Knight and Hoeksema, 1990 also observed sudden drop in V_p and V_s amplitude which suggests high attenuation between saturation of 0.73 and 0.81. They concluded that the difference in the velocity behavior in imbibition and drainage is because of changes in fluid phases (air & water) geometry in pore space of rock (also by Endres and Knight, 1989). Vp measured in case of drainage shows relatively smooth decrease throughout the decrease in brine saturation.

2.5 Laboratory based velocity as a function of stress and fluids (brine and oil)

Most of the laboratory based experiments have been performed as function of effective pressure and fluid type. Nur and Simmons, 1969 presented some experimental velocity (includes P and S wave) results on low porosity rocks like granite and Bedford limestone. They compared velocity values between water and dry saturated samples as a function confining pressure. Nur and Simmons (1969) justified the rapid increasing trend in P and S velocity with confining pressure, as closure of cracks present in the low porosity rocks. A rapid change in velocity trend as a function of pressure is followed by asymptotic curve velocity is measured as function of confining pressure and zero pore pressure.

King (1966) demonstrated the difference in dry velocity measurement parallel and perpendicular to the bedding in the Berea sandstone, former shows the higher. He, also, reported crossover of the velocity variation as a function of confining pressure between brine and kerosene saturated Berea sandstone. Ideally, the range of P velocity values for brine should be larger than corresponding values for oil and dry state and range of dry S-wave velocity values should be larger than corresponding oil and brine saturated measurements.

The crossover is an anomaly mentioned by King (1966), caused by 'relaxation behavior' of contained liquid in small cracks. Later in 1986, Winkler showed velocity dispersion (described in Chapter 4, sec 4.5) as a cause of such relaxation behavior. Apart from dry and saturated velocity measurements, the influence of pore pressure on velocity values of Berea sandstone indicates the role of fluid density. Nitrogen (N_2) and brine were used as a pore fluid.

Unlike this observation, Christensen (1984) reported strong influence (positive slope) of confining pressure on Vp, along constant differential pressure on water saturated marine basalt rock.

Ideally, the rock matrix should remain unaffected with constant differential pressure (effective pressure law). At constant differential, the increase in confining pressure should counteract the increase in pore pressure which maintains constancy in velocity values. The velocity values along the constant differential pressure are influenced by pore fluid and rock properties (King, 1966; Hofmann et al., 2005). The rock properties may include closure of micro-cracks, cementation and matrix density. Pore pressure affects the fluid properties like density and fluid modulus that in turn affect the velocity.

2.6 Effective pressure law and Biot effective stress coefficient

The effective pressure is defined as

$$P_e = P_c - nP_p \qquad \ldots (2.1)$$

Where, P_c and P_p are confining and pore pressure respectively. Effective pressure law is valid when a petrophysical property at particular confining and pore pressure is same when determined at confining pressure equal to effective pressure and zero pore pressure (Robin, 1973). 'n' is Biot effective stress coefficient which differentiates effective pressure from differential pressure ($P_e = P_d$ at n=1). The n values indicate the effect of pore pressure on petrophysical parameters. 'n' defined for static deformation is given (Biot, 1955) as

$$n = 1 - \frac{K_{dry}}{K_m} \qquad \ldots (2.2)$$

The 'n' values in static conditions depend only on rock properties. Dynamic mode of measurements required 'n' to be calculated (Todd and Simmons, 1972; Christensen, 1984) as

$$n = 1 - \frac{\left[\frac{\delta V}{\delta P_p}\right]_{P_d=const.}}{\left[\frac{\delta V}{\delta P_d}\right]_{P_p=const.}} \qquad \ldots (2.3)$$

$\left[\frac{\delta V}{\delta P_p}\right]_{P_d=const.}$ - is the change in velocity with pore pressure at constant differential pressure. In Fig. 2.7, $\left[\frac{\delta V}{\delta P_p}\right]_{P_d=const.}$ refer to the slope of 'P_d=const'.

$\left[\frac{\delta V}{\delta P_d}\right]_{P_p=const.}$ - is the change in velocity as a function of differential pressure at constant pore pressure. In Fig. 2.7, $\left[\frac{\delta V}{\delta P_d}\right]_{P_p=const.}$ refer to slope of 'P_p = const' at a particular pore pressure value.

If the slope of the velocity data, aligned in a constant differential trend line, is positive then n<1 and if negative, n>1. For perfect horizontal orientation, n=1. Dynamic n-values are published for different rocks and saturants. Many authors (Todd and Simmons, 1972; Christensen and Wang, 1985; Hornby, 1996; Prasad and Manghnani, 1997, Hoffman et al, 2005, Tinni et al. 2011) have reported the n values dependency on fluid properties (density and compressibility) and differential pressure.

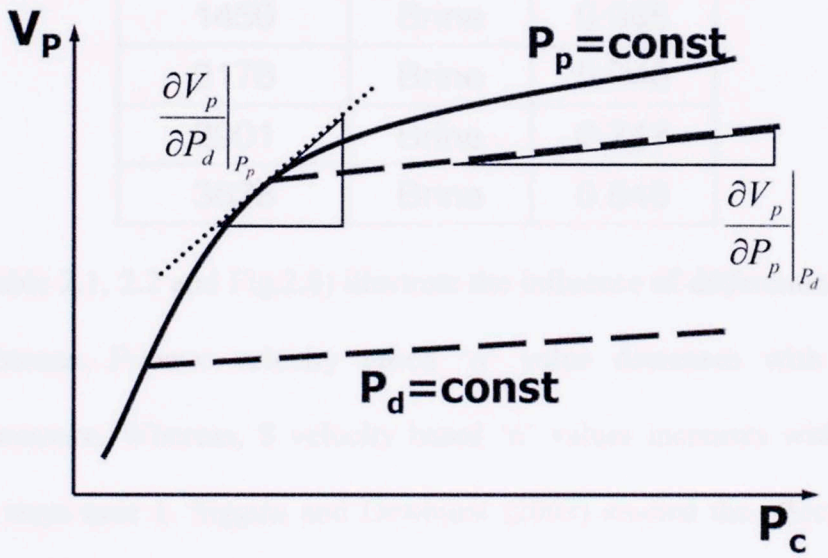

Figure 2.7: The methodology to calculate numerator and denominator of second term of equation 2.3 (Hofmann et al., 2005).

Table 2.1: n-values for Berea sandstone with water saturation (Christensen and Wang, 1985).

Diff. press (psi)	Fluid	n_p	n_s
73	Brine	0.99	
725	Brine	0.93	1.02
2901	Brine	0.89	1.06
8702	Brine	0.84	1.07

Table 2.2: n-value of Berea sandstone with water as pore fluid (Prasad and Manghnani, 1997).

Diff. press (psi)	fluid	n_p
725	Brine	0.936
1450	Brine	0.985
2176	Brine	0.940
2901	Brine	0.747
3626	Brine	0.648

The plots (Table 2.1, 2.2 and Fig.2.8) illustrate the influence of differential pressure on 'n' in sandstones. P-wave velocity based 'n' value decreases with increase in differential pressure. Whereas, S velocity based 'n' values increases with differential pressure but stays near 1. Siggins and Dewhurst (2003) studied the effective pressure dependency of velocity and 'n' on oil saturated sample. At lower differential pressure, n values are nearer to 1 for both water/brine and oil saturants (Fig 2.9).

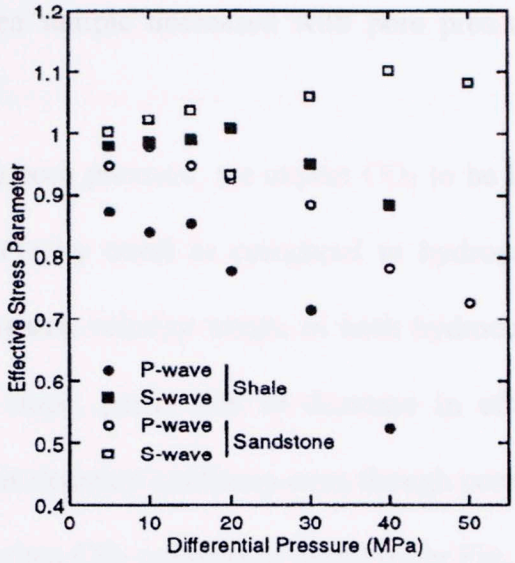

Figure 2.8: Range of n-values for water saturated Berea sandstone (Hornby, 1996)

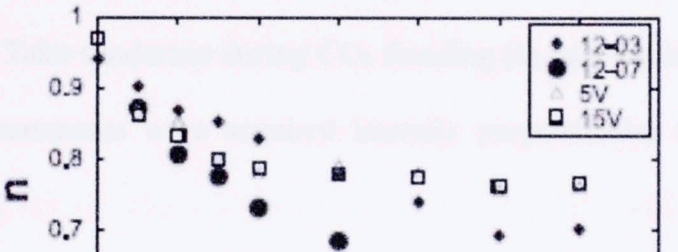

Figure 2.9: Decrease in n values with differential pressure in oil saturated sandstone (Siggins and Dewhurst, 2003).

2.7 Experiments on CO_2

Han et al. (2010) studied P-wave velocity of pure CO_2 at different pressure and temperature and obtained polynomial correlations that can be used to estimate CO_2 fluid modulus. Wang and Nur (1982) flooded hydrocarbon and CO_2 at different pore and confining pressure in Berea, Beaver, Boise, Conotton and Ottawa sandstones. Travel times were measured as a function of pore pressure. The CO_2 was injected at pressure of 1015 psi in the hydrocarbon saturated sample maintained at 580 psi pore pressure. The

velocity across the Berea sample decreased with pore pressure when saturated with hydrocarbon and CO_2.

Below 7 Mpa (1000 psi) pore pressure, we expect CO_2 to be in gaseous state which is responsible for lower velocity trend as compared to hydrocarbon saturated velocity measurements. The measured velocity trends in both hydrocarbon and CO_2 saturated samples have negative slope, partly due to decrease in effective pressure as pore pressure is increased. This decrease continues even though pore pressure is raised above 7 Mpa, critical pressure when CO_2 converts to liquid (refer Fig. 2.1).

In 2004, Xue and Ohsumi carried out laboratory based P-wave velocity measurements on water saturated Tako sandstone during CO_2 flooding (in gas, liquid and supercritical phases). The measurements were acquired laterally perpendicular to flood front (as shown in Fig 2.10).

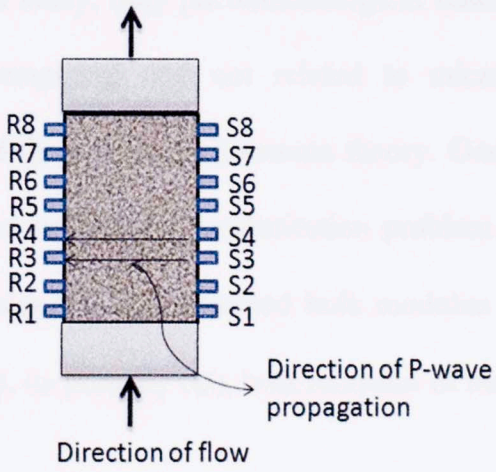

Figure 2.10: (left) Sample and transducer set up for the experiment performed by Xue and Ohsumi, 2004.

The P wave velocity decreases when liquid CO_2 is introduced (initially in position S1R1 and then to all positions). They also observed that this decrease is more as compared to

gaseous CO_2 replacing water from the pores. According to Xue and Ohsumi, the variation in velocity values after complete flooding suggests non homogeneous pore fluid distribution.

Kim et al. in 2011 attempted to create velocity profile experimentally against saturation. They measured P-wave velocity and resistivity simultaneously with CO_2 flooding in water saturated Berea sandstone. Using Archie's equation, CO_2 saturation was determined from the resistivity which was measured across sections of the sample.

P wave velocity measurement showed a non-linear overall drop of 9% at 50% CO_2 saturation.

2.8 Quantification of seismic parameters: Biot-Gassmann theory and Patchy saturation

The experimental data as discussed are used to generate or validate the theoretical models. As a part of this study, only phenomenological based models are discussed in which parameters are empirical and not related to microstructure (Jakobsen and Chapman, 2009). One of them is Biot Gassmann theory. Gassmann (1951) formulated theoretical correlations to employ fluid substitution problem. The equation, known as Gassmann's equation, calculates the saturated bulk modulus of the rock (K_e) from its dry bulk modulus (K_{dry}), its porosity (φ), bulk modulus of the matrix mineral (K_m) and fluids (K_f).

$$K_e = K_{dry} + \frac{n^2 K_f}{\varphi + \frac{K_f}{K_g}(n - \varphi)} \qquad \ldots (2.4)$$

Dry bulk modulus is determined experimentally from velocity measurements on dry or 'drained of pore fluid' sample. K_{dry} is calculated from the velocity measured on sample

drained of pore fluid if chemical interaction between pore surface and fluid exist. The Biot effective stress coefficient, 'n' is determined using Eq. 2.2 (static) or 2.3 (dynamic) depending on the type of loading or measurement acquired. Porosity is the total connected porosity of the sample. K_f is the overall modulus of fluid mixture which may comprise of one or more fluids (such as brine, oil, CO_2 etc) in pore space. It is calculated as Ruess average of the bulk modulus, K (which is also inverse of the compressibility) of each fluid.

$$\frac{1}{K_f} = \sum_{i=1}^{n} \left[\frac{S}{K}\right]_i \quad \ldots (2.5)$$

Where, S_i and K_i represent the saturation and bulk moduli of the ith fluid.

The mineral bulk modulus (K_g) is the Voigt-Ruess-Hill (VRH) average of moduli of each minerals. The VRH is calculated as:

$$K_{VRH} = \frac{1}{2}(K_{Ruess} + K_{Voigt})$$

$$\frac{1}{K_{Ruess}} = \sum_{i=1}^{n} \left[\frac{C}{K_m}\right]_i$$

$$K_{Voigt} = \sum_{i=1}^{n} C_i K_{mi}$$

C is the concentration and K_m is the modulus of the ith minerals.

Unlike saturated bulk modulus which is a dependent on pore fluid, shear modulus is independent of the fluid and its properties. This implies dry and saturated shear moduli are equal (Biot, 1956; Berryman, 1999).

There are some assumptions that should be considered before using the above correlation (Eq. 2.4), as mentioned below:

1) The rock is homogeneous and isotropic.
2) The pore spaces are all connected.
3) The frequency of the propagating wave is low enough such that the length required for pore pressure equilibration is in between the pore dimensions (restricting fluid movement) and seismic wavelength.
4) There is no chemical interaction between pore surface and pore fluid.

If any assumption is violated, Gassmann's equation cannot be applied for fluid substitution modeling. Our study deals with a complex gas CO_2 in the pore space of a high porosity rock such as Tuscaloosa and Paluxy sandstones. Such nature of the pore fluid and matrix properties can lead to violation of the 3rd assumption. The CO_2 distribution can be 'patchy', that implies that the distribution of fluid is in patches and does not equilibrate during the wave propagation (Smith et al., 2003; Mavko et al., 2003). The effective bulk modulus in patchy saturation conditions is formulated (Hill, 1963 and Berryman and Milton, 1991) as,

$$K_e = \left[\sum_i^n \frac{f_i}{\left(K_{isat} + \frac{4}{3}G\right)}\right]^{-1} - \frac{4}{3}G \quad \ldots (2.6)$$

Where, f_i - the volumetric fraction of patch i, n is the number of patches, G is the shear modulus and K_{isat} is the bulk modulus of the rock saturated with the ith fluid. A complete tutorial and procedure to apply this equation is given in a paper by Smith et al., 2003.

Many authors used the theoretical models (esp. Biot-Gassmann theory) to analyze the influence of fluids on logs, seismic attributes (especially elastic velocity or impedance) or lab based petrophysical velocity measurements. These correlations suit the behavior

of velocities when fluid and its properties changes. Based on these equations, Batzle et al., (1998) predicted a qualitative velocity profile in reservoir undergoing CO_2 EOR.

Biot-Gassmann theory is used extensively for locating hydrocarbon and water saturations and currently for CO_2 detection. However, no validation is ever reported that confirms its applicability in CO_2 flooding. For example, Lumley et al. (2008) used properties of Sliepner reservoir and Biot-Gassmann equation to forward model the velocities and density variation with CO_2 saturation.

Similar to Lumley et al., O'Brien (2004) used Biot Gassmann equations to detect CO_2 saturation but found inapplicable since he suspected uncertainties associated with pore fluid properties and presence of multiphase flow. Also, O'Brien et al. in 2010 mentioned the complications involved in inverting the seismic data to saturation values due to non-linearity associated with Biot-Gassmann equations.

Similar forward model based on Biot-Gassmann theory and patchy saturation was presented by Vanorio et al. in 2010 which postulates the velocity behavior when CO_2 flood the reservoir saturated with water. They came up with Fig.2.11 which shows the expected overall acoustic behavior of CO_2 saturation in all kinds of rocks. They also take mineralogy transformation (chemical interaction) into account that occurs when rock minerals are exposed to CO_2. The conditions applied are the possible transformations rock saturated with CO_2 may encounter. The blue curve shows velocity signature for patchy CO_2 saturation, red curve for uniform CO_2 saturation and green curve shows the decrease in velocity due to increase in porosity. Chemical interaction might give rise to porosity increase. Detailed discussion on chemical interaction is presented in next section.

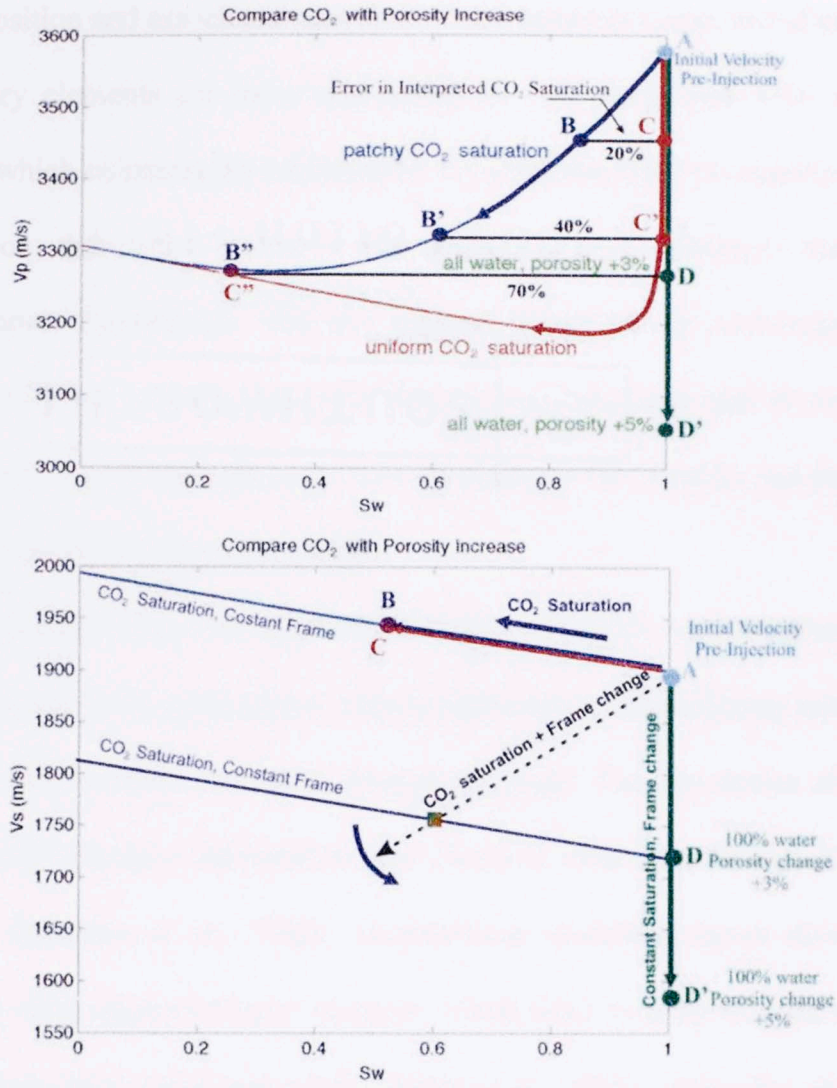

Figure 2.11: Modeled P and S-wave velocities of water saturated rock with ongoing CO_2 flooding (Vanorio et al., 2010).

Although Biot-Gassmann theory is widely employed for qualitative analysis, Vialle and Vanorio (2011), Ghosh and Sen (2012) found it inefficient to predict the elastic properties changes when carbonates are flooded with CO_2 saturated water.

2.9 Digenesis with CO_2 exposure

CO_2 interaction can initiate geochemical alteration in rocks which leads to digenesis. CO_2 is found to be corrosive to mineral matrix, clays and pore fluid (Kharaka et al., 2006; Benson and Cole, 2008). The severity of such reactions depends on host rock

mineral composition and associated pore fluid. Rock minerals composed of calcium and iron as primary elements are more susceptible to CO_2 alterations. CO_2 also forms carbonic acid which enhances the corrosion by lowering the pH. CO_2 exposure weakens the cementation that exists between the grains in rock skeleton. Geochemical simulations shows theoretically that the cements (made up of carbonate) dissolve initially increasing the porosity but later dissolution of feldspar and precipitation of reacted carbonate, quartz minerals and clays can decrease the porosity and permeability (Benson and Cole, 2008; Gaus et al., 2005).

Carbonic acid formed from the interaction between the CO_2 and brine/water reacts largely with Ca and Fe oxyhydroxides. This is important while analyzing mineralogical transformation in clays (also termed as mineral trapping). The dissolution of siderite is expected since no siderite concentration was observed from Frio formation core after CO_2 flooding (Kharaka et al., 2006). Geochemical modeling shows dissolution of oilgoclase and other aluminosilicate minerals which react to CO_2 to form dawsonite, gibbsite and amorphous silica precipitate (White et al., 2003). When the pH increases above threshold, carbonate and other minerals precipitate showing reverse trend.

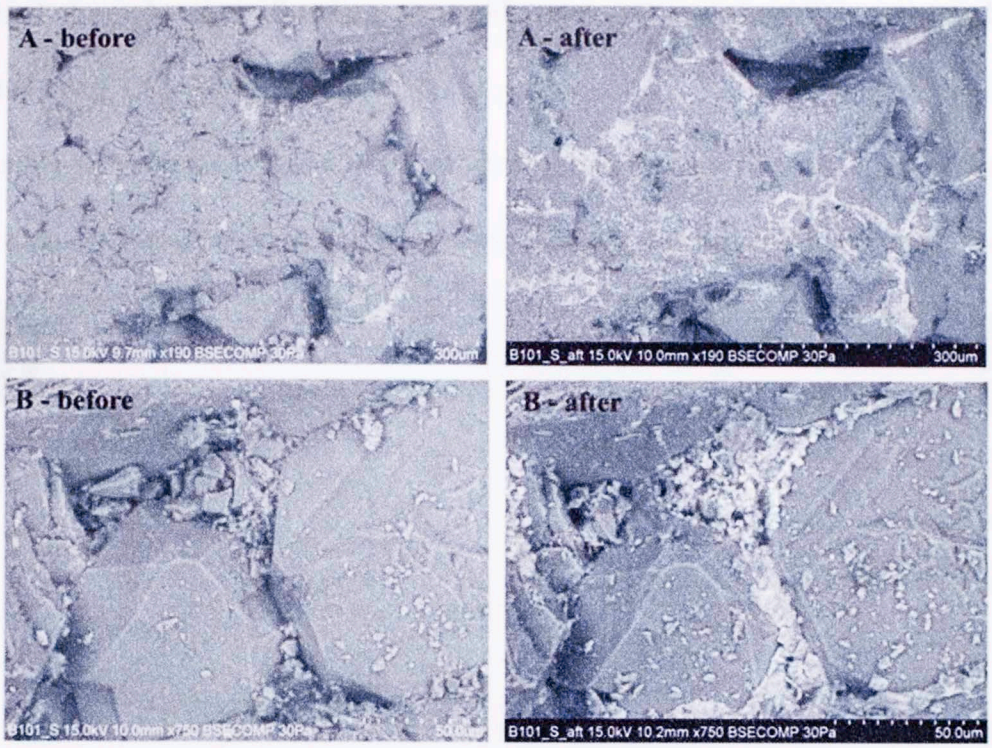

Figure 2.12: The SEM images of pre and post-flooded CO_2 to observe the geochemical effect in Fountainebleau sandstone (Vanorio et al., 2010)

SEM analysis (Fig 2.12) by Vanorio et al. in 2010 indicates visual differences before and after CO_2 flooding. Petrographic analysis performed by Barclay and Worden in 2000 shows the K-feldspar alteration due to CO_2 influx in arkosic sandstone to form quartz, kaolinite and ankerite. These studies implies that CO_2 can affect the elastic parameters to a great extent.

2.10 Study field

Hot Bryant basin of Delhi field, LA is currently under CO_2 flooding for EOR purpose (Fig. 2.13). Delhi field detailed structural geology and lithology is given in detail by Powell (1972). Intensive oil management started in 1953 with commissioning of water flooding in Delhi field. The original oil in place is 357 MMBO and 54% of it has been

recovered through water flooding. An additional 15% of the oil is expected to be extracted using CO_2 EOR (Richards, 2011).

3D seismic survey was acquired on a patch of Delhi field in Nov 2008, termed as base survey (blue outlined in Fig 2.14). Another monitoring 3D seismic survey was shot in

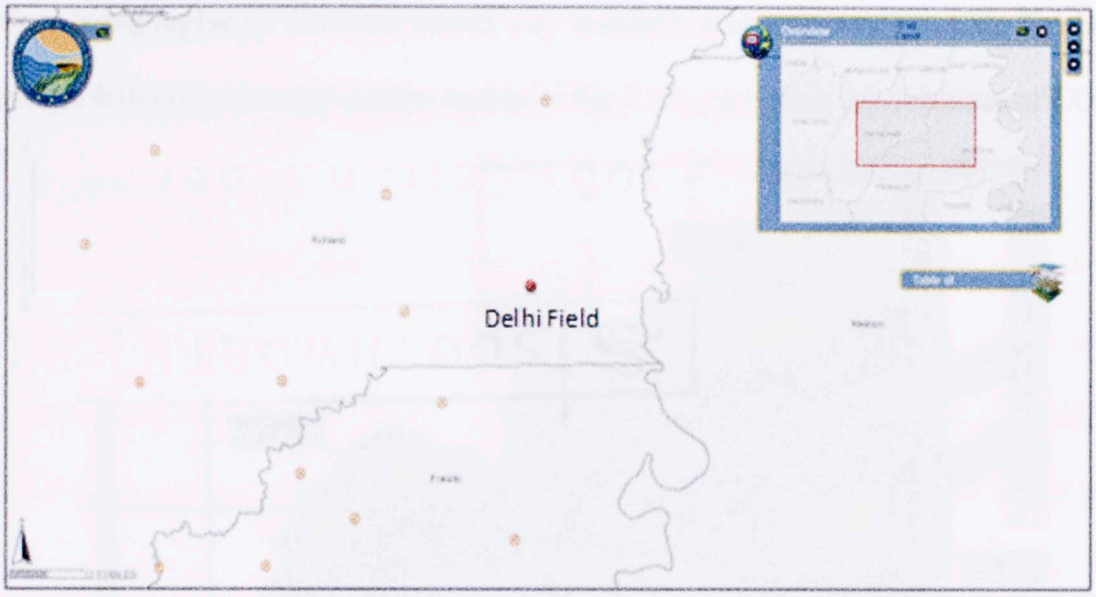

Figure 2.13: The geographic location of Delhi field

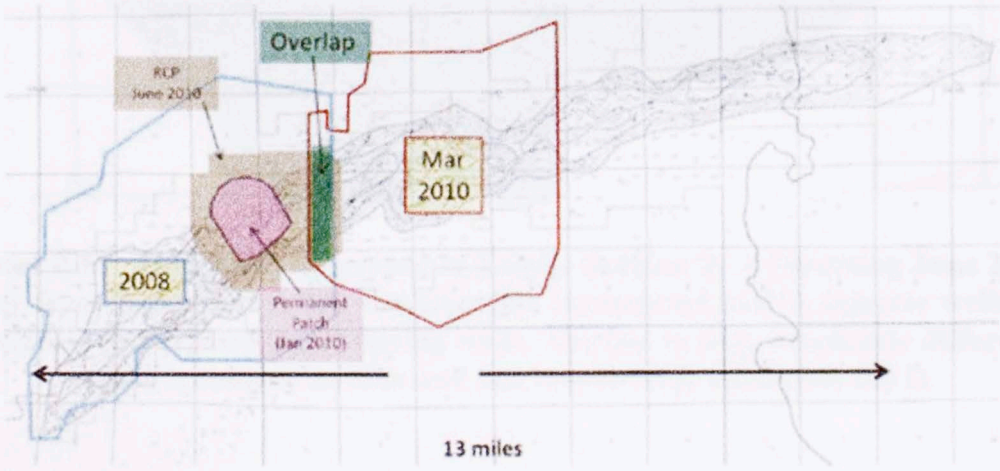

Figure 2.14: 3D seismic surveys acquired over Delhi field at different times. The blue outlined is the region of Nov 2008 survey, red outline corresponds to Mar 2010 survey and pink color region shows Jan 2010 survey. Richards, 2011 used 2010 and 2008 survey to create amplitude difference map (refer Fig 2.15)

Dec 2010 to create 4D time lapse survey (pink colored in Fig 2.14). The seismic amplitude difference map was created by subtracting the 2010 seismic from base survey. The regions, where fluid is substituted in these two years, are captured by the time lapse difference map (Fig 2.15). The lower the difference, lower is the probability of fluid being replaced. The base survey was acquired on reservoir before CO_2 flooding. The high difference (orange-yellow region in Fig 2.15) represents the presence of CO_2.

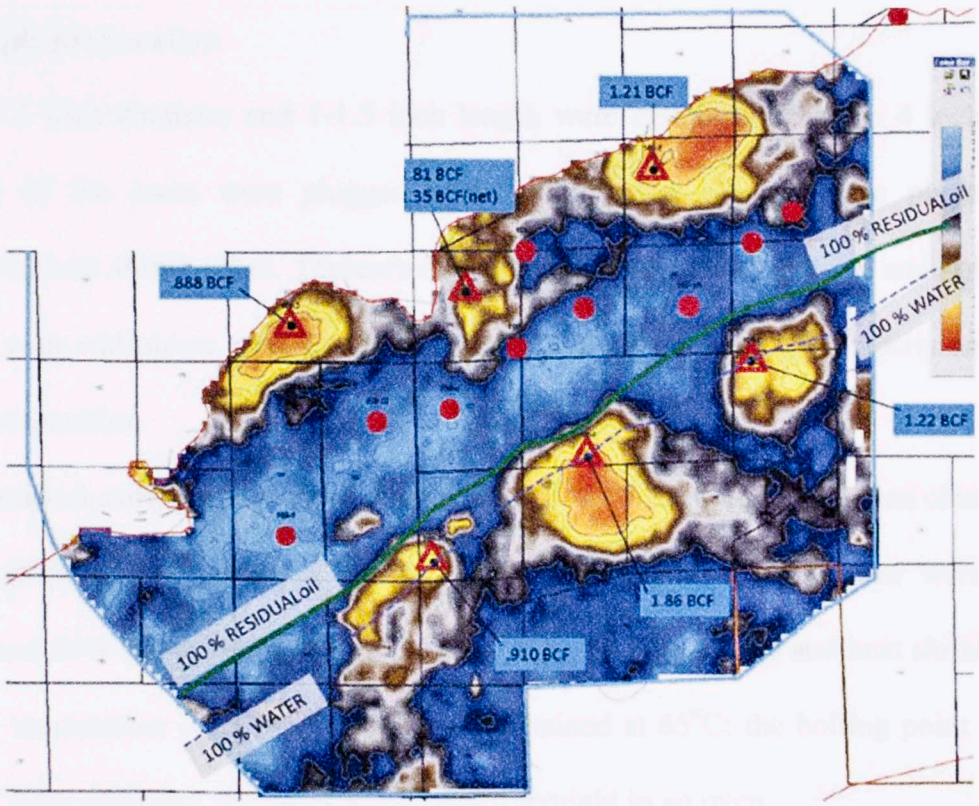

Figure 2.15: Amplitude difference in Paluxy horizon by subtracting June 2010 survey from 2008 survey. The red triangles correspond to CO_2 injector wells and red circles correspond to producing wells. The low to high amplitude difference region is colored as blue and red respectively (Richard, 2011).

The reservoir is Hot Bryant zone, mainly composed of Cretaceous sandstones (Powell, 1972; Richards, 2011). Our zone of interest lies in lower Cretaceous layer composed of Tuscaloosa and Paluxy sandstone at depth of 3200 to 3300 ft. Oil water contact is at 3286 ft.

Chapter 3 Experimental Procedure

3.1 Introduction

The core used in the study is from well 159-1 from Delhi field. This is an injector well. A series of experiments were performed on plugs to understand the seismic velocity in the reservoir rock with CO_2 flooding. This chapter includes the steps adopted for sample preparation, details of experimental set up and experimental procedure.

3.2 Sample preparation

Plugs of 1 inch diameter and 1-1.5 inch length were extracted from the 4 inch core. Majority of the cores were plugged horizontally. After plugging, the plugs were jacketed in heat shrink tubes. Thereafter, samples were trimmed, cleaned and polished. The left over end pieces were used for determination of mineralogy, porosity and thin section preparation.

The cylindrical samples were dried in an oven at 100 ^{o}C for 8 hours and then cleaned in Soxhlet extractor for another 8 hours. The solvent used in the extractor were 80% toluene and 20% methanol by volume. As the samples were friable and heat shrink tube covered, temperature of the extractor was maintained at 65°C; the boiling point of the mixture. After cleaning, the plugs were dried overnight in an oven.

Once dried, the ends of the cylindrical plugs were polished parallel to reduce standard deviation (upto $\pm$0.05 mm) in length measurements and for proper coupling of the samples with the transducer for velocity measurements. The length and diameter were measured at 6 different points and averaged. A balance with precision of 0.0001 gm was used to obtain plugs weight. Bulk volume was measured via mercury immersion

technique. Also, petrophysical properties were measured like mineralogy, porosity and permeability as discussed in the next section.

3.3 Petrophysical properties

3.3.1 Porosity measurement

Porosity is the ratio of the pore volume to the bulk volume of a material

$$\varphi = \frac{V_p}{V_b} = \frac{(V_b - V_g)}{V_b}$$

where V_p - pore volume (ml), V_b - bulk volume (ml) and V_g is the grain volume (ml) of the material.

Automated Porosimeter (AP608) and High Pressure Porosimeter (HPP) were used for the measurements (Fig 3.1). Both pieces of equipment work on the principle of Boyle's law which calculates grain density. The volume occupied by the grains (V_g) is calculated from the grain density and weight of the sample. Then, porosity is estimated using the above equation. To observe the porosity response with effective pressure; porosities at effective pressures of 100, 500, 1000 and 1500 psi were measured. Permeability was also measured using AP608 simultaneously with porosity.

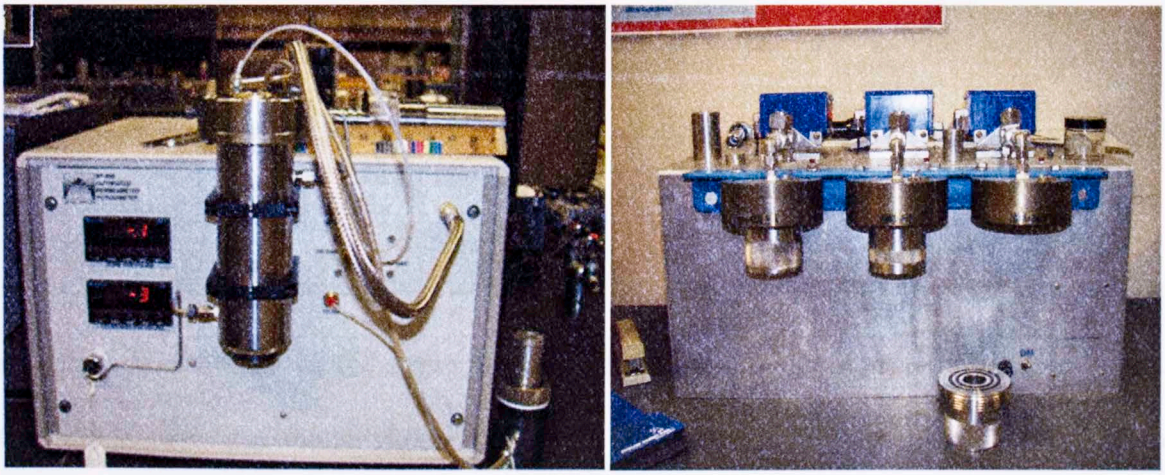

Figure 3.1: AP608 (left) and HPP (right) equipments used to measure porosity.

3.3.2 Mineralogy

Fourier Transform Infrared Spectroscopy (FTIR) was used to determine the quantitative mineralogy of the samples. Inversion of spectra generated from the current FTIR set up can be quantified in 16 commonly found minerals: quartz, calcite, dolomite, siderite, aragonite, illite, smectite, kaolinite, chlorite, oligoclase feldspar, orthoclase feldspar, mixed clays, albite, apatite, pyrite and anhydrite. Advantages associated with FTIR are: the error is usually below 1.2 by wt% (Sondergeld and Rai, 1993; Ballard, 2007), portable and gives the result faster compared to other techniques.

FTIR technique generates spectra based on the absorption of mid-infrared energy by different minerals. Fig 3.2 shows some of the infrared spectra of few minerals.

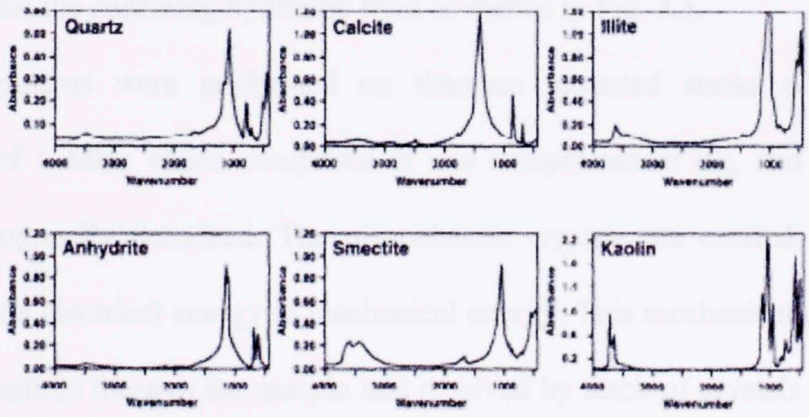

Figure 3.2: Infrared spectra of the common minerals found in the sedimentary rocks (Sondergeld and Rai, 1993)

A part of the sample was crushed to fines and dried for 8 hours to remove moisture. The samples were placed in the asher to remove the organic content, if there were any. Organic matter and water vapor can affect the spectra; therefore it is important to remove them before placing in the spectrometer. 0.0005 gm of ashed sample was mixed

with 0.3 gm of dried KBr powder and pressurized to transform it into clear disc. The disc was placed in the spectrometer chamber filled with dry nitrogen and exposed to mid-infrared radiation. The generated spectra was acquired and inverted for minerals composition (wt. percent).

3.4 Experiemental set up

3.4.1 Sample-transducer assembly set up

The assembly of sample and transducer was prepared for the velocity measurement. The heat shrink covered samples were enveloped with the vinyl tube jacket of 1 inch inner diameter. The length of vinyl tube jacket was slightly longer than the samples allowing end caps to fit with the sample. The vinyl tubes are non reactive to CO_2. Hose clamps were used on both ends of the assembled sample and transducer to tighten them together and also to seal the confining hydraulic fluid as shown in Fig. 3.3.

Initial experiments were performed on titanium mounted stacks of piezoelectric transducers of 1 MHz which comprises of one compressional (P), and two shear (S) crystals orthogonally polarized. The piezoelectric crystals are excited by ~ 12 volts which converts electrical energy to mechanical energy. This mechanical energy in form of waves transmits through the sample and received by stack of crystals at the receiver end. The receiver end stacks convert mechanical energy back to electrical energy which gets recoded and displayed in form of waves.

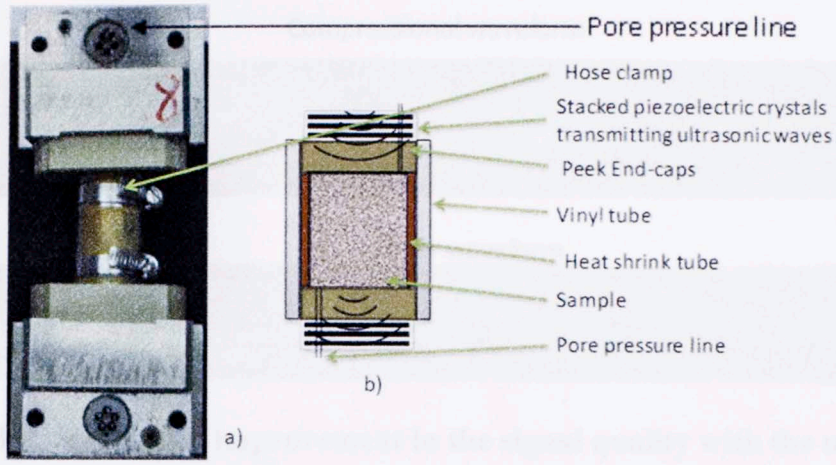

Figure 3.3: a) and b) showing the actual sample transducer assembly and its detailed inside picture respectively.

3.4.2 Transducers and their signal quality

The signal quality was found to be poor with titanium end caps as shown in Fig. 3.4. The reason of such poor quality is high impedance contrast between rock and titanium which is responsible for high reflection rather than transmittance through the sample. An improved version of transducer pair was introduced with end-caps made of Peek. The signal quality significantly improved (refer Fig 3.5).

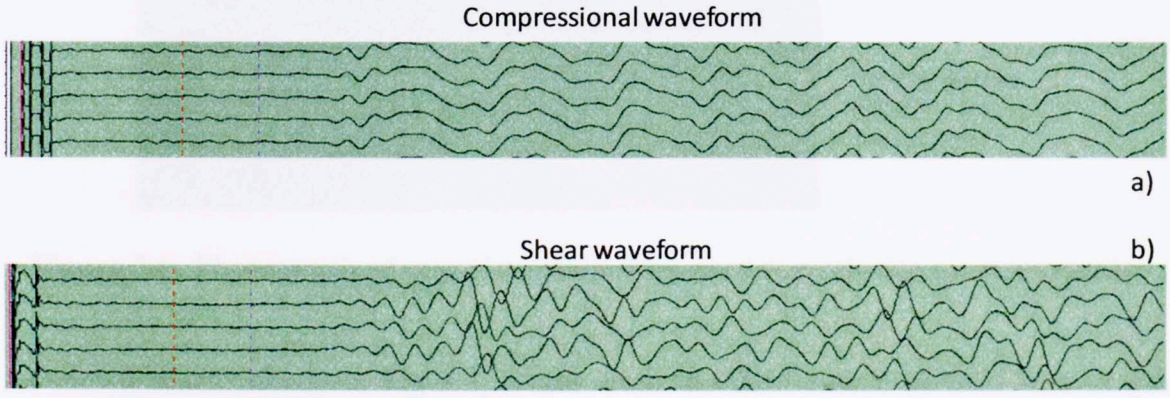

Figure 3.4: The compressional waveforms (a) and shear waveforms (b) showing poor quality signal with the Tuscaloosa sandstone using titanium endcaps.

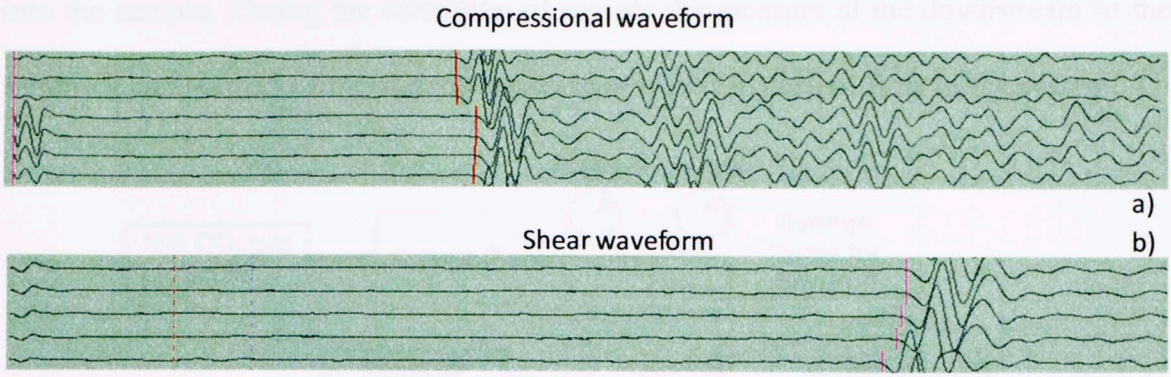

Figure 3.5: Significant improvement in the signal quality with the use of peek endcaps mounted transducer.

3.4.3 Equipment set up

The sample transducer assembly was placed in pressure chamber of the velocity station (Fig 3.7). The pressure chamber is hydraulically pressurized using precise syringe pumps filled with mineral oil. Seismic velocities are measured at various confining and pore pressures (pressure points) applied to the samples.

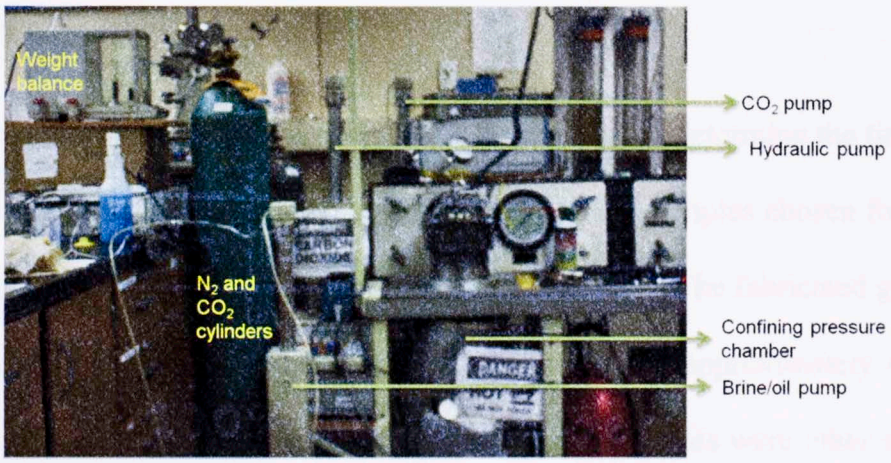

Figure 3.6: Photograph of experimental set up used for velocity measurements.

As shown schematically in Fig 3.7, a tube from the fluid source (a fluid tank or gas cylinder) connected to the syringe pumps which mounted with controller and pressure transducer. These pumps were controlled either manually or remotely to infuse the fluid

into the sample. During the saturation of sample the pressure at the downstream of the sample is maintained using back pressure valve to obtain desired flow in the system.

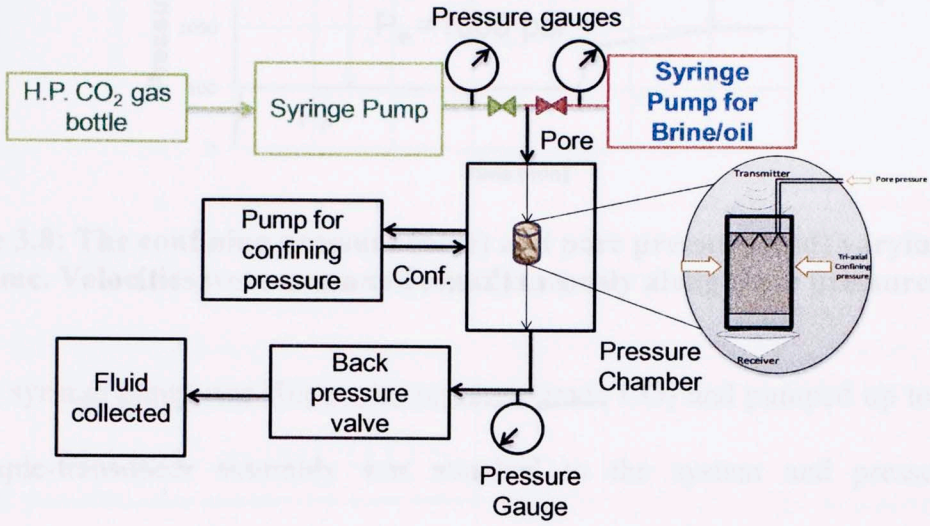

Figure 3.7: Schematic diagram of the experimental set up. Both P and S-velocity can be measured with various pore and confining pressure using different saturants

3.5 Experimental procedure

3.5.1 Velocity equilibration study

Velocity equilibration study is done as a base experiment to determine the time required for CO_2 to equilibrate with the pore pressure change. The samples chosen for this study were fabricated glass bead, Berea sandstone, coal and shale. The fabricated glass bead is made up of micro glass beads fused together with porosity approximately 40%. Berea sandstone was used as a standard rock sample. Coal and shales were other sedimentary rocks studied for curiosity (reported in Appendix A). The pressure points, combination of confining and pore pressure (shown in Fig.3.8), were selected to observe the time required for CO_2 to equilibrate in the pores of the rock at constant effective pressure.

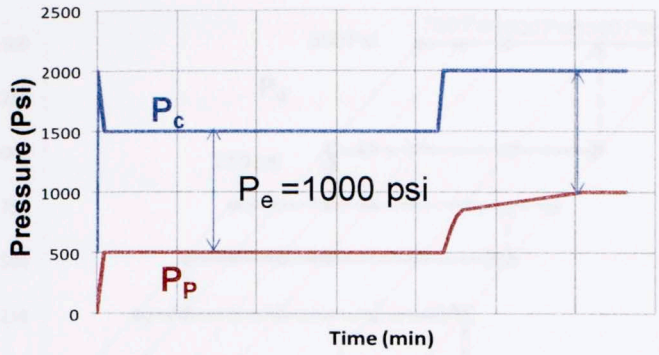

Figure 3.8: The confining pressure (blue) and pore pressure (red) varying with time. Velocities were measured simultaneously along these pressures.

The CO_2 syringe pump was filled with research grade CO_2 and pumped up to 500 psi. The sample-transducer assembly was attached to the system and pressurized to confining pressure of 2000 psi (with step increments of 250 psi). P and S velocities were measured simultaneously at every pressure point. The confining and pore pressure was set at 1500 psi and 500 psi and maintained for 3 to 4 hours measuring velocity at an interval of 10 to 15 mins (Fig 3.8). Confining was later raised to 2000 psi. We recorded the velocities at constant confining pressure of 2000 psi while increasing the pore pressure to 500, 700, 800, 900 psi and lastly to 1000 psi. The confining and pore pressure of 2000 psi and 1000 psi is maintained for next 2 hours.

3.5.2 Velocity versus effective pressure

Effective pressure is one of the factors that affect seismic velocities; therefore it was important to measure velocity with change in effective pressure. Also, the fluid and rock properties primarily depend on effective pressure as discussed in chapter 2. The study of velocity response with liquid CO_2 saturation was performed on fabricated glass bead, Berea, Tuscaloosa and Paluxy sandstones by varying the effective and pore pressure.

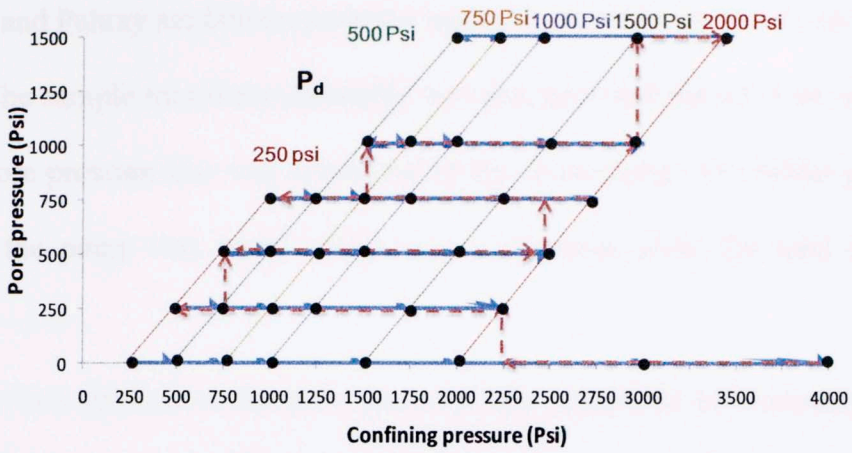

Figure 3.9: The confining pressure and pore pressure points (black nodes) were chosen to maintain constant differential pressure intervals (written in colored)

Confining pressure was applied on the sample with zero pore pressure as shown in array of black dots at the bottom of the plot in Fig 3.9. P and S wave velocity measured at these nodes are the dry velocity measurements. The pore pressure was gradually raised to 250 psi and new set of velocity measurements were acquired. And so on, pore pressure was increased till 1500 psi in order to acquire sufficient measurements to observe the behavior of velocity with wide range of effective pressures i.e. 250, 500, 750, 1000, 1500 and 2000 psi.

3.5.3 Influence of fluid saturation on velocity

Based on the information of velocity equilibration time and its dependency on effective pressure, P and S wave velocity were measured with various saturating fluids. The first step was to determine the dead volume, which includes the total pore pressure tube volume excluding the sample. The fluid saturation is determined while injecting fluid in the pore pressure tube based on the determined dead volume and change in pump volume.

The Tuscaloosa and Paluxy sandstones undergo sample preparation as mentioned earlier in the chapter. The sample transducer assembly was prepared and placed in the pressure chamber. The pore pressure line was connected to the brine pump. The initial pressure and volume of the pump was noted which was a reference point for total injected volume.

Formation brine was injected in the pore pressure tube controlled by injection pump. The saturation in sample was raised progressively as shown in Fig 3.10. Six saturation points of 30%, 60%, 90%, 95%, 97% and 100% were chosen and both P and S waves were measured at each point. Once 100% saturation was achieved, oil was pumped in to the system which displaced brine from the sample. The upstream injector pump was then switched to liquid CO_2 (with pore pressure above 1000 psi). The concise description is plotted in Fig 3.10.

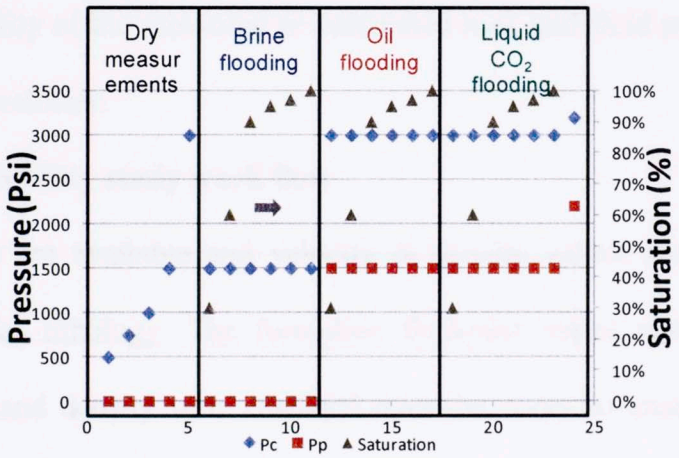

Figure 3.10: The selected confining (blue), pore pressure (red) and saturation (brown) points at which seismic velocities are measured. The pore and confining pressure are chosen based on the insitu pressure conditions in Hot Bryant Basin and insitu fluids are used for saturation purposes

The pressurized CO_2 was pushed into the upstream tube filled with oil water system and velocities were measured at the desired saturation intervals. The weighing balance was

kept at the downstream of the system and based on the mass balance, amount of oil displaced by liquid CO_2 was determined. This also overcomes the uncertainty associated with the quantity of absorbed CO_2 in oil water system. The observations are plotted and shown in Chapter 5.

3.6 Sensitivity analysis

In order to perform sensitivity analysis of P wave velocity to parameters such as porosity, fluid density and moduli, one parameter is altered keeping other same in the Gassmann's equation for each flooding scenario. The three different porosity values are 21%, 23% and 25% while rests of the parameters are same as actual. To determine the fluid moduli sensitivity, the fluid moduli of brine and oil was increase by 0.2, 0.1 and decreased by 0.1. The density was raised by 0.2, 0.3 and dropped by 0.02 to estimate the sensitivity of P wave velocity to fluid density. The sensitivity analysis is performed to account the reliability of the measured or calculated rock and fluid properties affecting the Biot predicted velocity.

3.7 4D seismic feasibility study work flow

Pre flooded zones are available and velocity & density values are averaged over a thickness of similar lithology. The formation thickness varies with depth. Average values of Vp, Vs and density were obtained over the zones to create logs that looks blocky in nature (Fig 3.11).

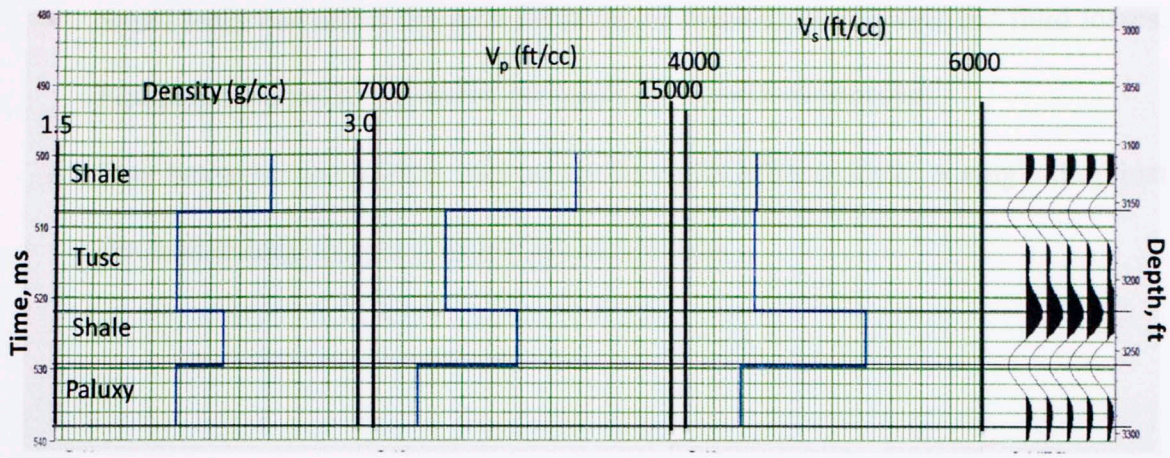

Figure 3.11: Blocked density, V_P and V_s logs as function of time (ms) and depth (ft)

Those average values of Vp, Vs and density logs are used to calculate reflection coefficient series, which is then convolved with a 60 Hz Ricker wavelet in order to obtain synthetic seismic (Aki and Richards, 1980). This model is also considered as a base model. CO_2 fluid substitution of 10%, 50% and 90% are performed on these logs using the empirical correlation discussed in Chapter 4. The post flood 2D synthetic seismic as a function of offset is generated from CO_2 substituted logs.

The pre flooded synthetic seismic model is subtracted from the base case. And then AVO response and difference map at the zones of expected CO_2 intrusion are investigated.

3.8 Precautions

Some precautionary measures should be taken for successful completions of the experiments:

- The equipments such as tubes, valves, seals, covers, back pressure valve, pumps and all other equipments exposed to CO_2 must be non corrosive to CO_2.
- All equipments must be cleaned with hot water, toluene and air after each experiment. Cleaning is also followed by drying the equipments with vacuum.

- Small leaks can affect the pore pressure, saturation calculations and fluid losses. Equipments must be examined for leaks after every experiment.
- Care has to be taken while measuring the outlet effluent fluid. A single drop lost can lead to large errors in saturation calculation.

Chapter 4 Results and Observations

4.1 Sample and fluid description

Fused glass bead and Berea sandstone were used to perform the velocity equilibrium and effective pressure study experiments whereas; Tuscaloosa and Paluxy sandstones were used in fluid flooding experiments. Research grade CO_2 and fluid recovered from the field were used for flooding. A set of rock properties are measured prior to velocity experiments.

Table 4.1: Petrophysical properties of samples chosen for velocity equilibration and effective pressure study.

Sample	Porosity (%)	Permeability (md)	Primary composition (%)
Fused glass beads	32	1000	Glass beads
Berea sandstone	18	76	84% quartz, 10% clays

80 ft core was received with its Geological characteristics shown in Table 4.2.

Table 4.2: Geological characteristics of the arrived core interval (courtesy: Denbury Resources)

Core interval (ft)	**Unit**	**Characteristics**	**Environment**
XX04-XX07	Tusc 9	Lower fine grain sand, quartz rich	Lower fluvial channel
XX25-XX28	Tusc 5	Middle fine grain sand, solely quartz	Middle fluvial channel
XX58-XX61	Tusc 3	Lower very fine grain, quartz rich	Fluvial channel
XX76-XX79	Paluxy	Lower very fine grain, quartz rich	Distributary mouth bar
XX82-XX85	Paluxy	Middle very fine grain sand, quartz rich	Estuary / Distributary channel

Four plugs from XX26.6, XX58, XX79 and XX83.5 ft were selected for flooding experiments. Petrophysical properties of these plugs are listed in Table 4.3 which were determined at native state prior to velocity measurements.

Table 4.3: Petrophysical properties of Tuscaloosa formation

Core interval (ft)	Porosity	Mineralogy represented by top 4 minerals (wt %)
XX26.6	23%	Quartz: 84%, clay: 6%, siderite: 2%
XX58	25%	Quartz: 87%, clay: 9%, siderite: 2%, albite: 1%
XX79	24%	Quartz: 81%, clay: 12%, albite: 2%
XX83.5	26%	Quartz: 86%, clay: 7%, siderite: 2%, albite: 5%

In Fig 4.1, measured porosity values are plotted as a function of effective pressure. Substantial change of 18% in porosity is observed when measured at higher effective pressure on different samples.

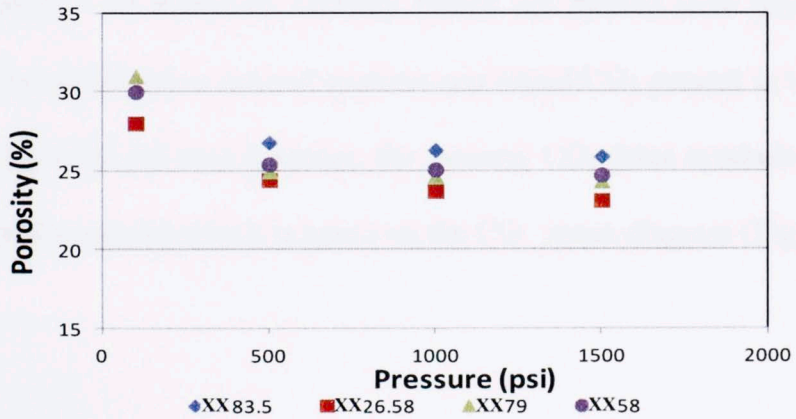

Figure 4.1: Porosity as function of pressure for plugs collected from various depths.

Table 4.4 lists all the fluids with their properties that are used in the experiments.

Table 4.4: Density and bulk modulus of formation brine, formation oil and CO_2 used in our experiments

Fluid	Phase	Density (g/cc)	Bulk modulus (Gpa)
CO2	Gas	0.002	1.3×10^{-4}
	Liquid (1500 psi)	0.733	0.01
Brine	Liquid	1.05	2.583
Oil	Liquid	0.81	1.375

4.2 Velocity Equilibration study

Compressional (V_p) and shear (V_s) wave velocities were measured as a function of time at pore pressures of 500 psi, 700 psi, 800 psi, 900 psi and 1000 psi with CO_2 as saturating fluid. Firstly, a standard sample i.e fused glass bead is used to study the velocity equilibration as it is unaffected when exposed to any fluid. Then, the Berea sandstone was used as it is a well studied sample whose mineral properties are common to other sandstones.

In Fig 4.2, variation of measured velocity values are plotted with time. The figure indicates that the equilibration time of gaseous and liquid CO_2 present in the pore space is 15 minutes. At 1000 psi pore pressure, the gaseous CO_2 (blue symbols) is converted to liquid CO_2 (red symbols) which is based on the CO_2 phase diagram (Fig 2.1).

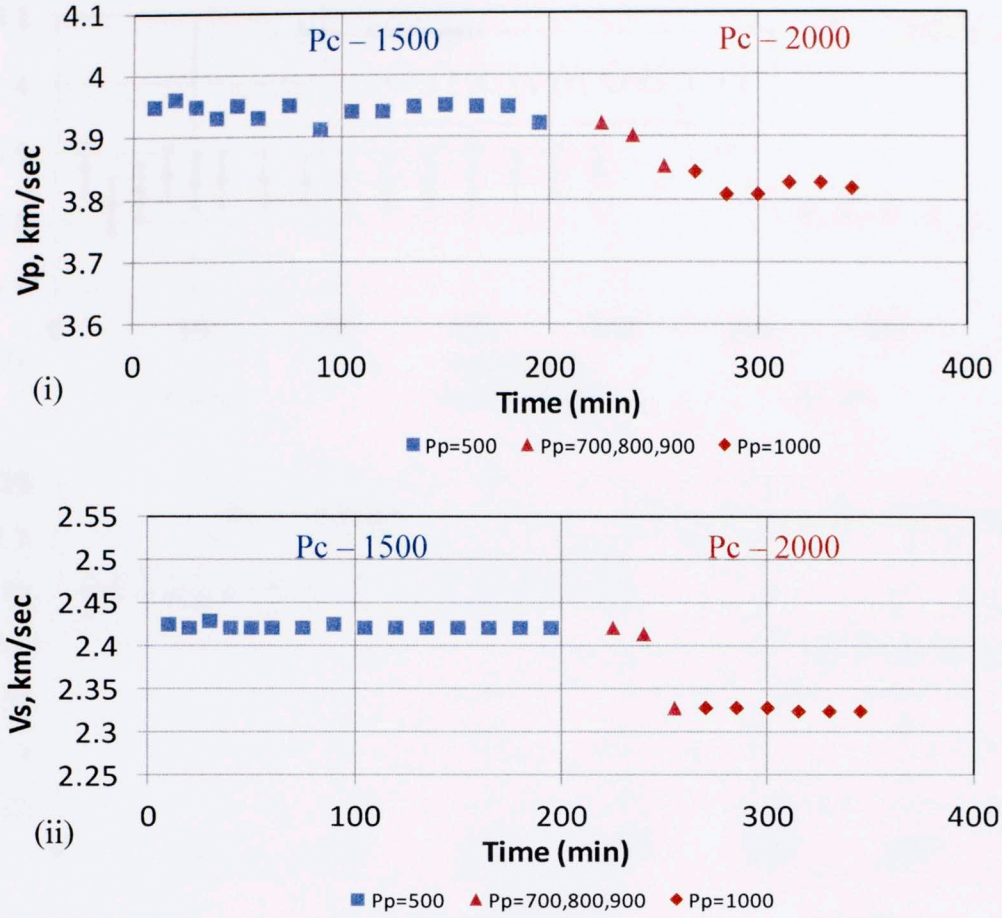

Figure 4.2: Compressional and Shear wave velocity in glass bead sample saturated with gaseous (blue square) and Liquid (red diamond) CO_2

As observed in Fig 4.2, V_p and V_s decrease by 3% and 4% respectively in fused glass bead with the change in pore pressure from 500 psi to 1000 psi at constant differential pressure of 1000 psi. The total percentage in error is less than 1%. This velocity equilibration experiment was also performed on the Berea sandstone. And the velocity equilibration time for Berea sandstone is found to be similar to that of fused glass bead sample.

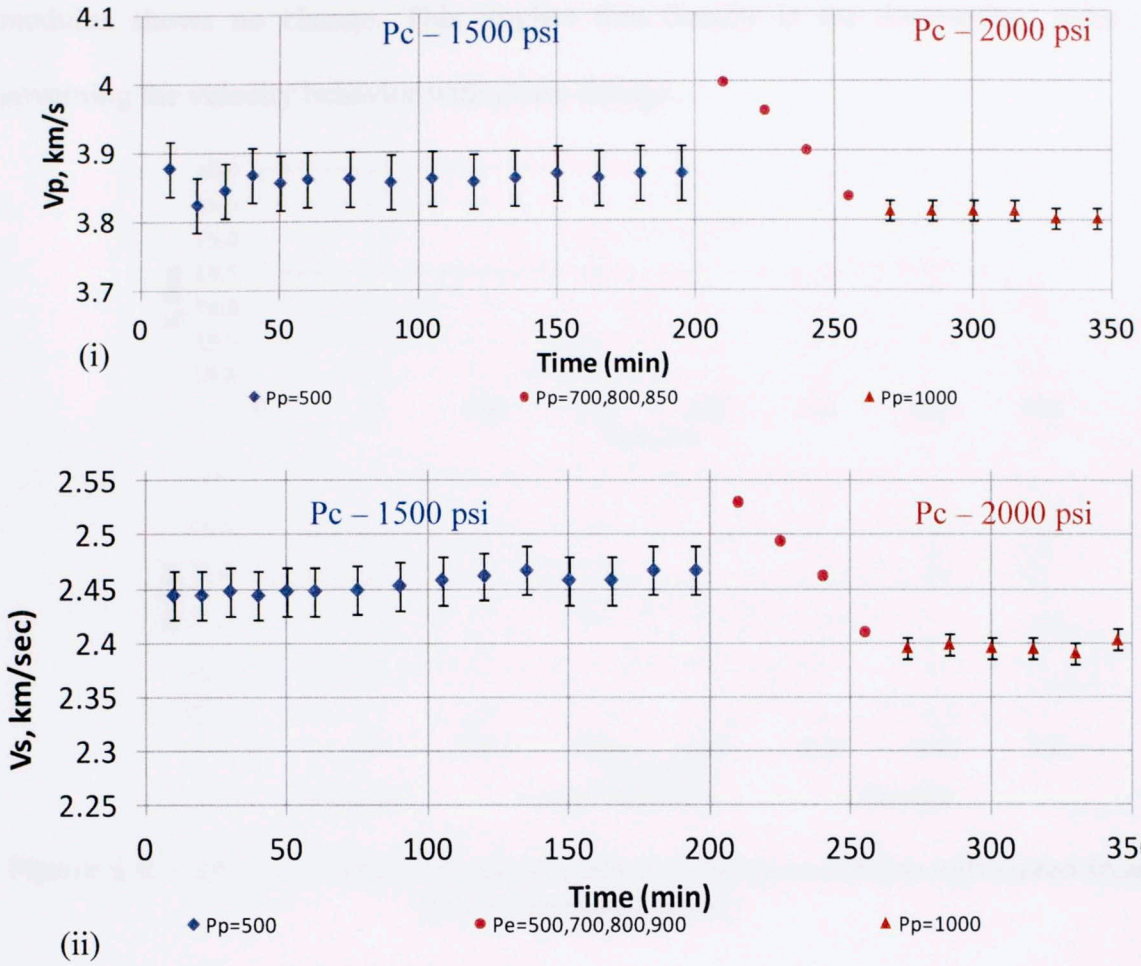

Figure 4.3 Measured P (i) and S (ii) wave velocity equilibrating with gaseous CO_2 (blue) and liquid state CO_2 (red) in Berea sandstone.

As referred to Fig 4.3, the measured V_p and V_s wave velocities decrease by 1.5% and 2.5% respectively from the transition of CO_2 from gas to liquid even at constant differential pressure.

From Peng-Robinson equation of state and CO_2 Phase diagram (Shakhashiri, 2008), we estimate 80% decrease in compressibility and 800% increase in fluid density with CO_2 phase change from gas to liquid. These changes in fluid properties affect the velocities in the rock saturated with CO_2. The bulk modulus calculated using Gassmann's equation shows slight increase with phase change as shown in Fig 4.4 whereas, shear

modulus shows no change. This implies that density is the dominating factor in governing the velocity behavior with phase change.

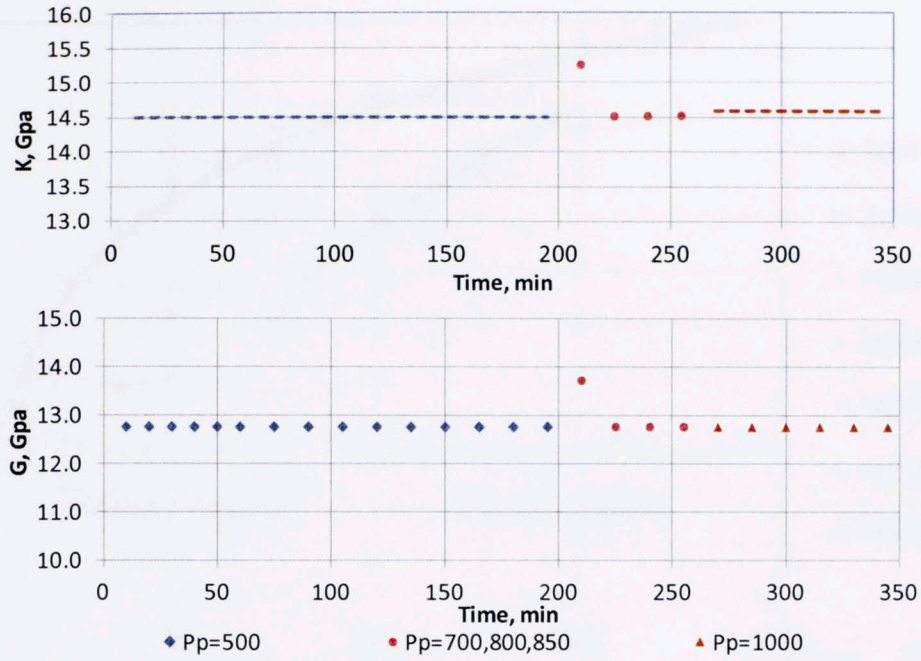

Figure 4.4: Calculated bulk and shear moduli of Berea sandstone calculated from Biot-Gassmann theory

4.3 Velocity variation with effective pressure

Berea and Tuscaloosa sandstones are subjected to next set of experiments to determine the influence of effective pressure.

4.3.1 Berea sandstone:

The first set of measurements was dry velocities i.e at zero pore pressure. The variation in V_p and V_s with confining pressure (250 to 4000 psi) in Berea sandstone are 46% and 42% respectively at zero pore pressure (Fig 4.5). The P and S velocity values at constant differential pressure are joined by linear regression analysis. The slopes of these linear lines in gas region are close to zero (except few exceptions of P velocity which shows slight dip) and are observed to be independent of the differential pressure.

Whereas the slopes of best fit lines representing P velocity in liquid region are positive and that of S velocity are close to zero except slopes at low differential pressures.

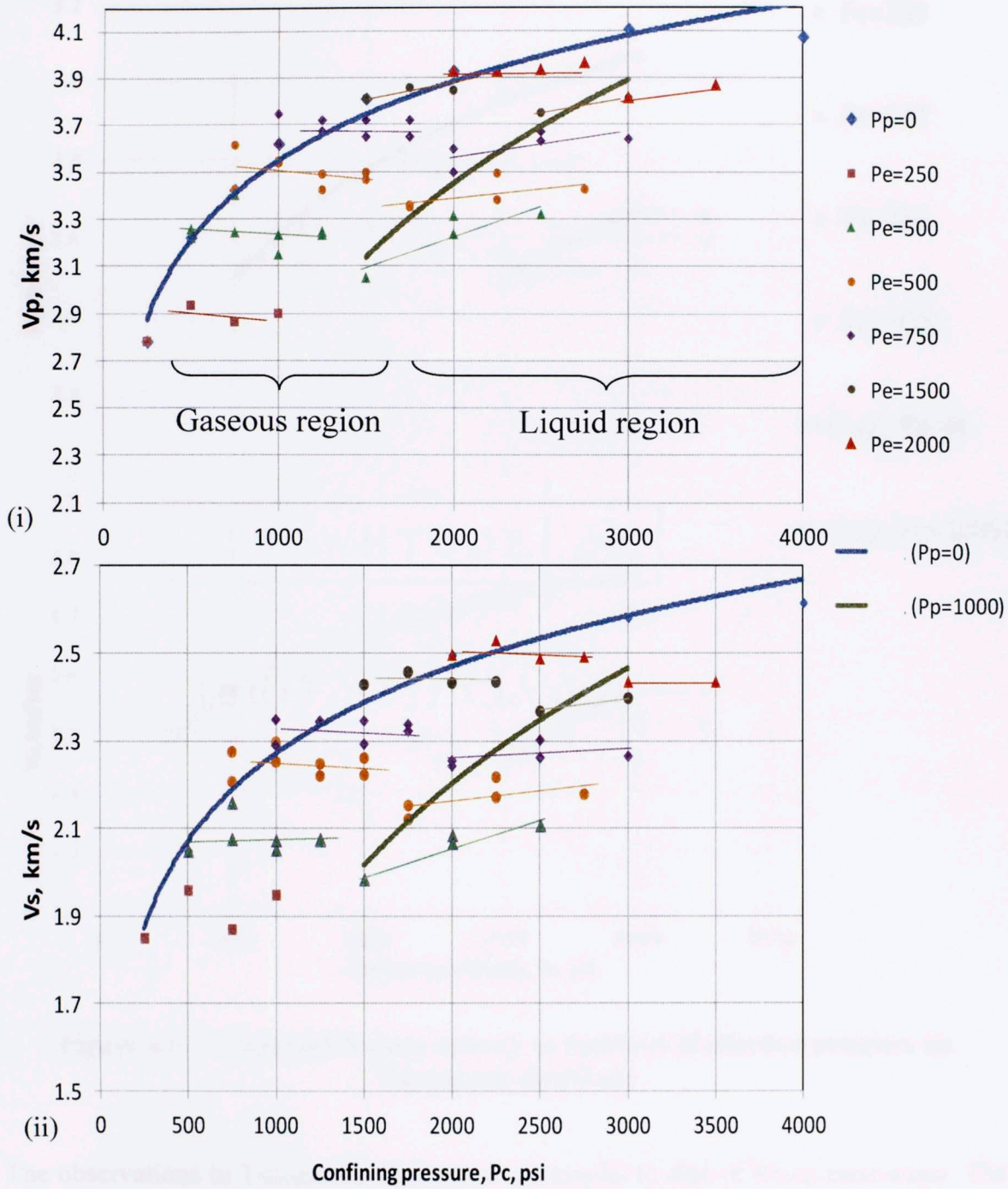

Figure 4.5: P (i) and S (ii) wave velocity measurements for varying confining and pore pressure for Berea sandstone.

The measured P and S velocity data are plotted in Fig 4.6 for Tuscaloosa sandstone samples. The experiments are restricted to 2000 psi effective pressure.

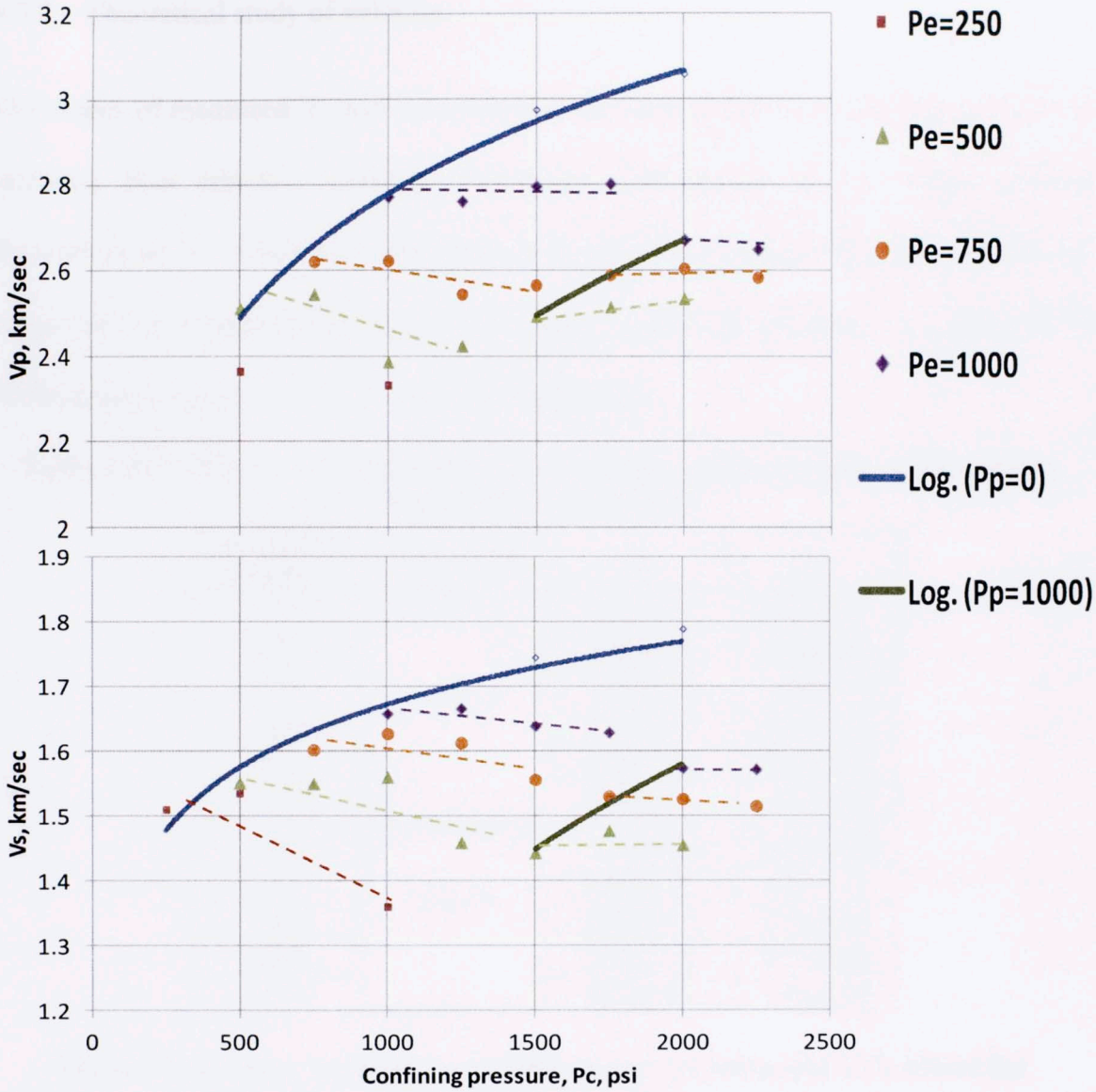

Figure 4.6: P (top) and S wave velocity as function of effective pressure on Tuscaloosa sandstone

The observations in Tuscaloosa sandstones are similar to that of Berea sandstones. The slopes of the best fit lines tend towards zero with increase in differential pressure. At

lower differential pressure, the slopes in gaseous region are negative whereas in liquid region of Fig 4.6, n values are positive for both P and S velocity.

4.3.2 Theoretical study of velocity:

The slopes of measured V_p and V_s trends with constant differential pressure are used to calculate Biot effective pressure coefficient also known as 'n'. More detailed description on 'n' values and calculation is provided in Chapter 2 Section 2.6. The 'n' values of CO_2 saturated Berea and Tuscaloosa sandstones are listed as a function of differential pressure in Table 4.5 and 4.6 respectively.

Table 4.5: Influence of differential pressure on n-values for gaseous and liquid CO_2 in Berea sandstone.

Diff. pressure (psi)	Fluid phase	n_p	n_s
250	Gas	**1.04**±0.07	**0.93**±0.09
500		**1.05**±0.10	**0.99**±0.09
750		**1.12**±0.13	**1.05**±0.11
1000		**1.01**±0.13	**0.99**±0.12
1500		**0.97**±0.15	**1.02**±0.15
2000		**0.95**±0.09	**1.14**±0.27
500	Liquid	**0.59**±0.15	**0.77**±0.08
750		**0.86**±0.11	**0.87**±0.11
1000		**0.82**±0.13	**0.94**±0.09
1500		**0.72**±0.00	**0.77**±0.00
2000		**0.72**±0.00	**1.00**±0.00

Table 4.6: n-values as function of differential pressure and CO_2 phase for Tuscaloosa sandstone.

Diff. pressure (psi)	Fluid	n_p	n_s
500	Gas	1.20±0.13	1.38±0.26
750		1.18±0.09	1.33±0.28
1000		0.90±0.06	1.33±0.13
500	Liquid	0.80±0.01	0.92±0.21
750		1.03±0.12	1.12±0.03
1000		1.27±0.00	1.04±0.00

This study shows that n values depend on both rock and fluid properties. For example, the 'n' values (for P and S velocity) in gas saturated Berea sandstone stays near 1. However, in liquid CO_2 saturated Berea sandstone, compressional n values are less than 1. As reported earlier by many authors (chapter 2), n values in brine saturated Berea sandstone were near 1 and decreases with increasing differential pressure.

In Tuscaloosa sandstones, compressional 'n' values variations are much larger with differential pressure as compared to Berea sandstones. Shear velocity is dominated by density and thus the difference in its 'n' values between gaseous CO_2 saturated and liquid CO_2 saturated is higher. On the other hand, compressional 'n' values tend to 1.0 at higher differential pressure.

A more recent study on tight sand samples, Tinni et al. in 2011 reported compressional and shear velocity based n values as a function of differential pressure which is found similar to this study. Apart from correct estimation of pore pressure from seismic data, n values also indicate the influence of microstructure on petrophysical properties.

Using above n-values, the experimentally measured V_p and V_s can be estimated using Biot-Gassmann theory (Gassmann, 1951). The theoretical P and S velocities are plotted on the same plot populated with experimental data (Fig 4.7) on Berea sandstone. The predicted velocities closely follow the experimental data. The dynamic 'n' values not only depend on rock properties but also on its saturant type and physical properties. This study shows the importance of dynamic n values that can be used in Biot-Gassmann theory instead of static n values.

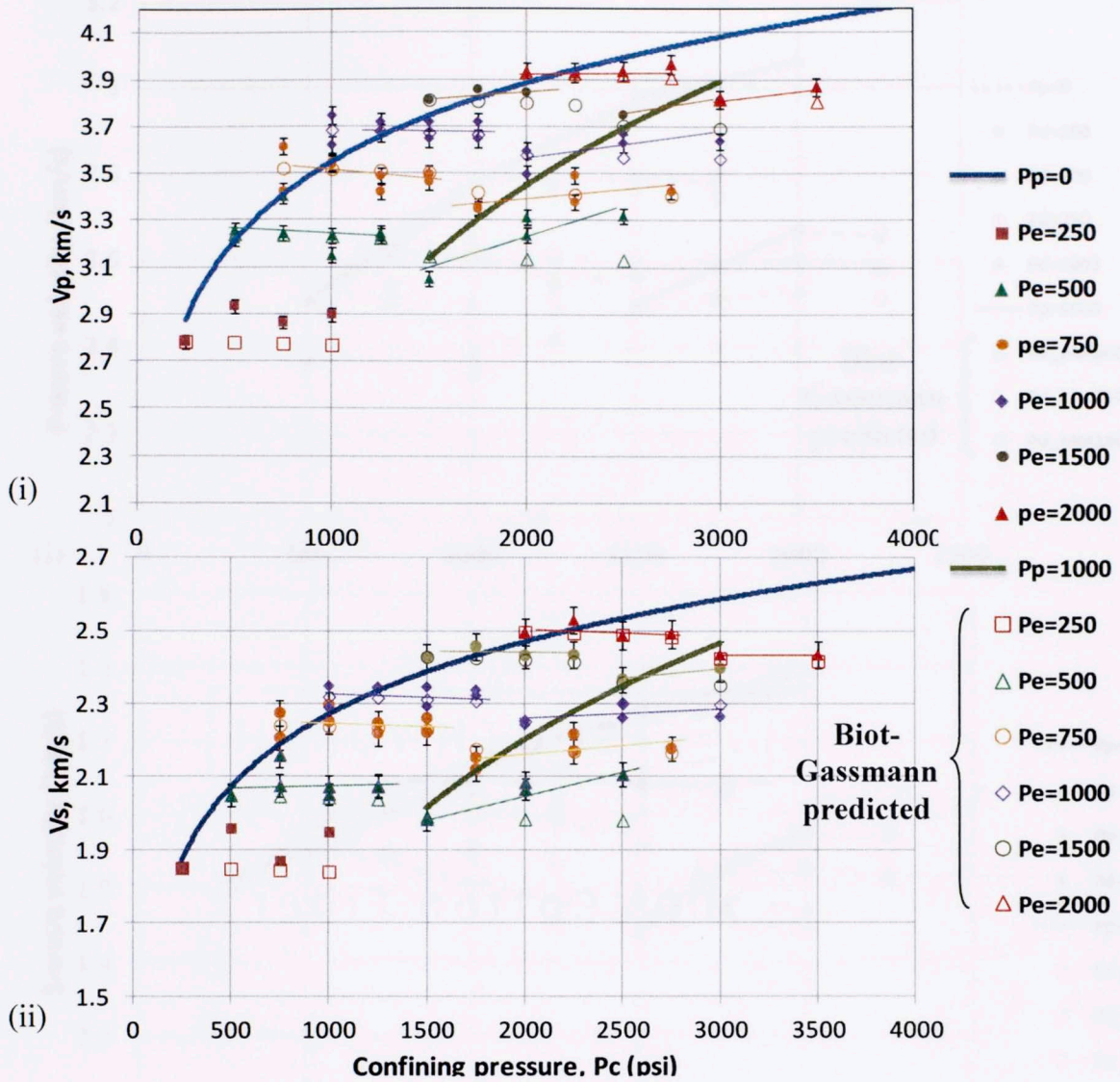

Figure 4.7: Measured Vp (i) and Vs (ii) values (shown in filled symbols) along with predicted Vp (i) and Vs (ii) values (shown in open symbols) as a function of confining and pore pressure in Berea sandstone.

Similar study is performed on Tuscaloosa sandstone where experimental and Biot Gassmann theory based compressional and shear velocities are plotted on the same Fig 4.8. It is observed that at differential pressure of 1500 psi, theoretical velocities fairly match the experimental velocity data.

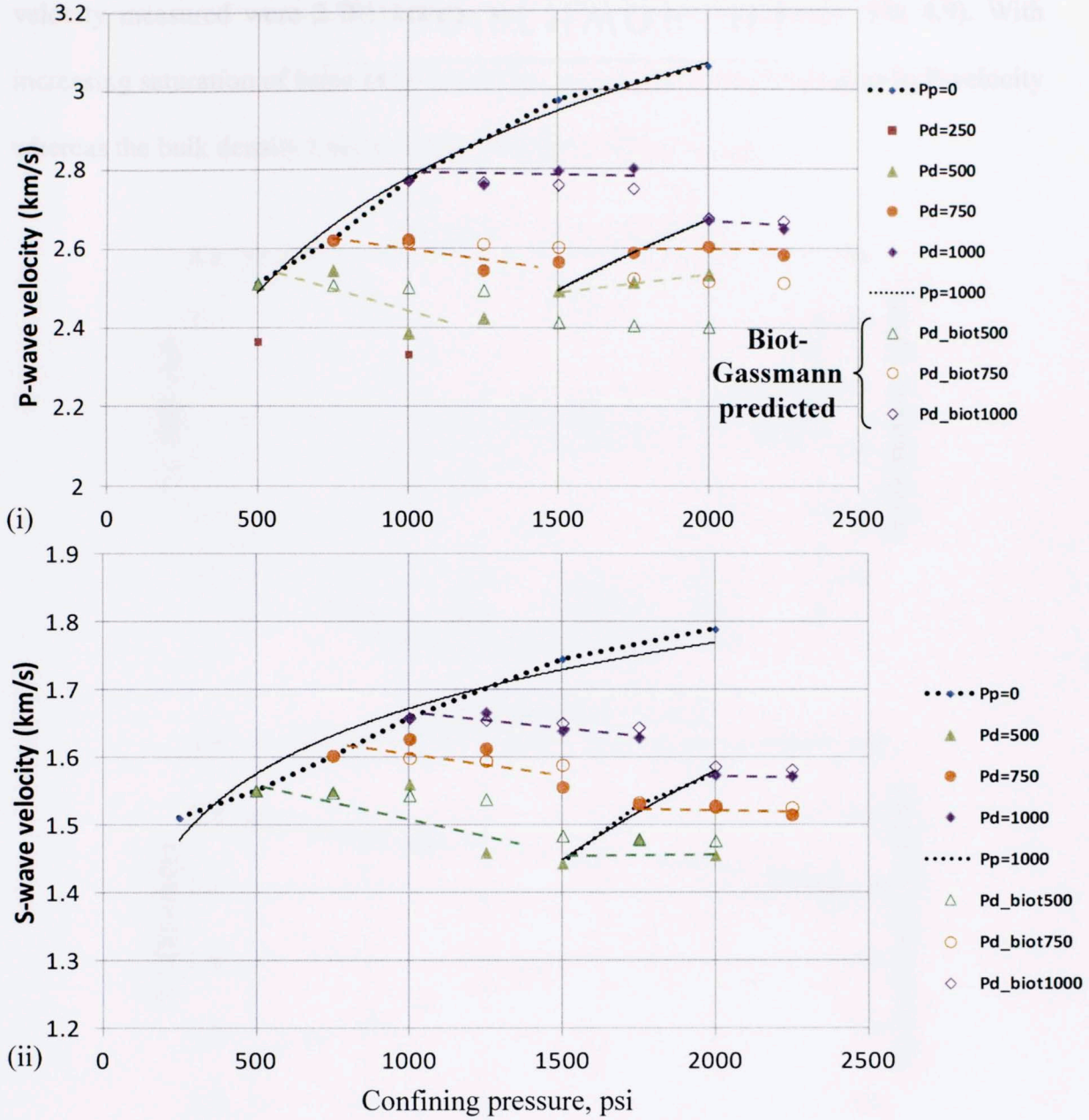

Figure 4.8: Measured Vp (i) and Vs (ii) values (shown in filled symbols) along with predicted Vp (i) and Vs (ii) values (shown in open symbols) as a function of confining and pore pressure in Tuscaloosa sandstone.

4.4 Velocity measurements with various fluid fronts

Velocity measurements in Tuscaloosa sandstone plugs saturated with brine, oil and CO_2 are shown in Fig 4.9 to 4.23. The sample XX26.6 ft is horizontal and has the lowest porosity. The plug was subjected to confining pressure of 1500 psi and the dry P and S

velocity measured were 2.791 km/sec and 1.787 km/cc respectively (Fig 4.9). With increasing saturation of brine from 0 to 95%, we observe 1.6% linear drop in P-velocity whereas the bulk density linearly rises throughout the saturation.

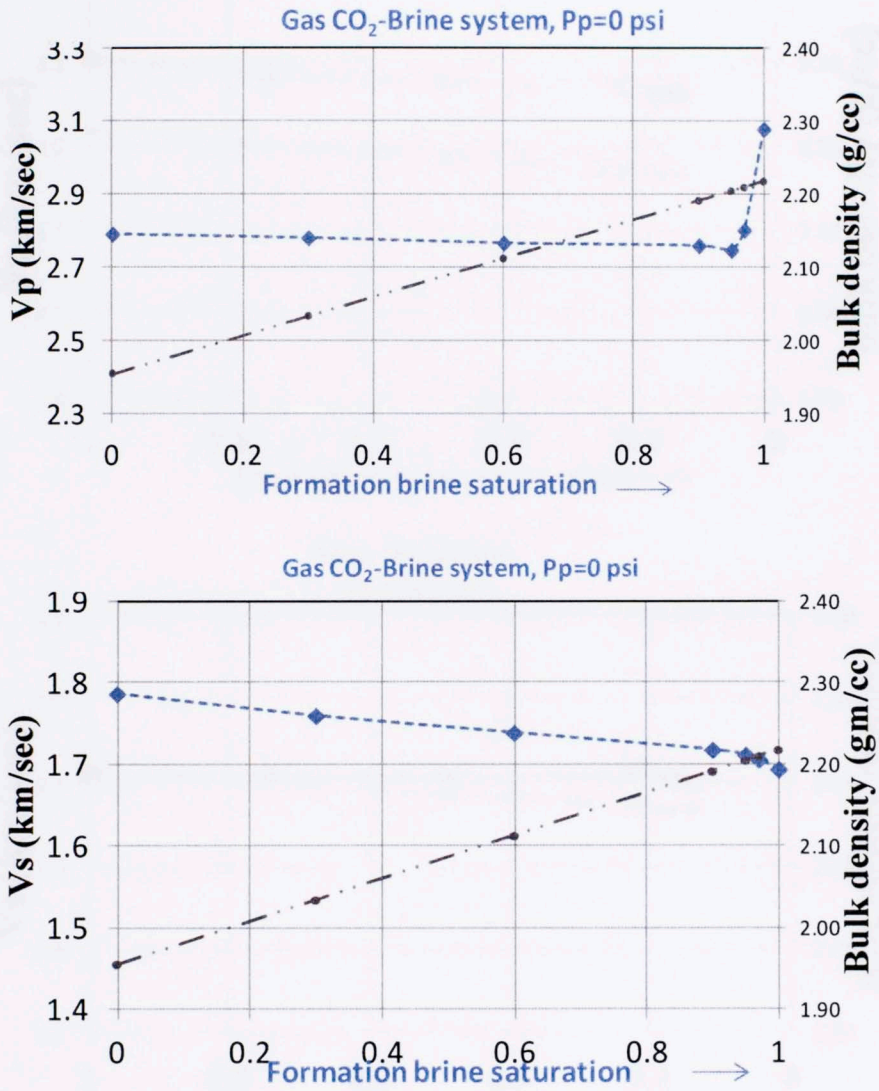

Figure 4.9: Measured P and S velocity (blue) along with calculated bulk density (grey) as a function of brine saturation for sample XX26.6 ft

At saturation beyond 95%, P-velocity increases steeply by 12.5% however S-velocity continued to decrease throughout the saturation. The overall decrease in S-velocity is

5.2%. At 100% brine saturation, oil is introduced and we observe decrease in the P-velocity (Fig. 4.10). It continues to decrease till irreducible water saturation is attained.

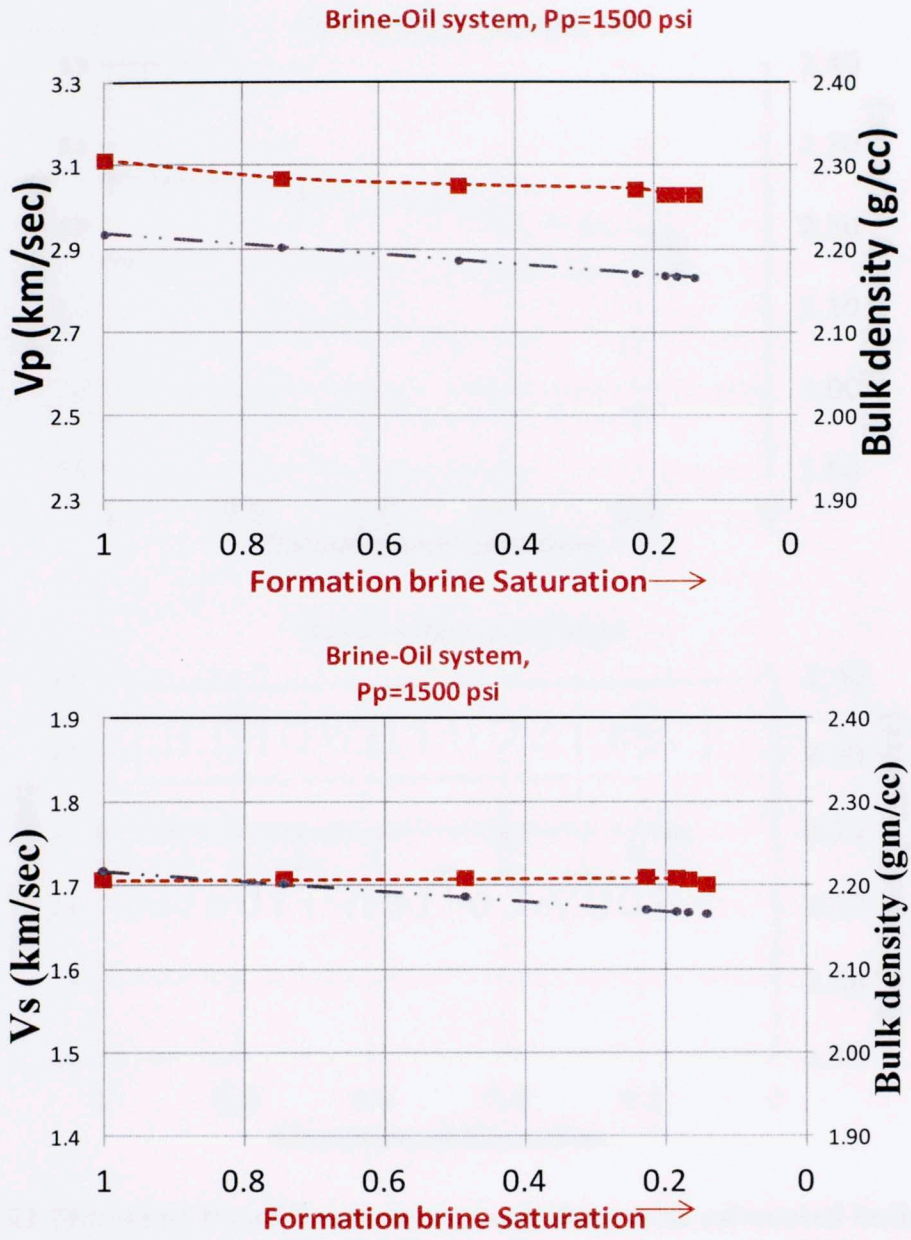

Figure 4.10 Measured P and S velocity (red) for sample XX26.6 ft along with calculated bulk density (grey) variation when formation oil replaces formation brine.

From Fig 4.11, the change in P wave velocity is 2.6% and in S wave velocity is negligible. The expected saturation condition simulates the reservoir condition. Liquid

CO_2 is introduced into the system at confining pressure of 3000 psi and pore pressure of 1500 psi.

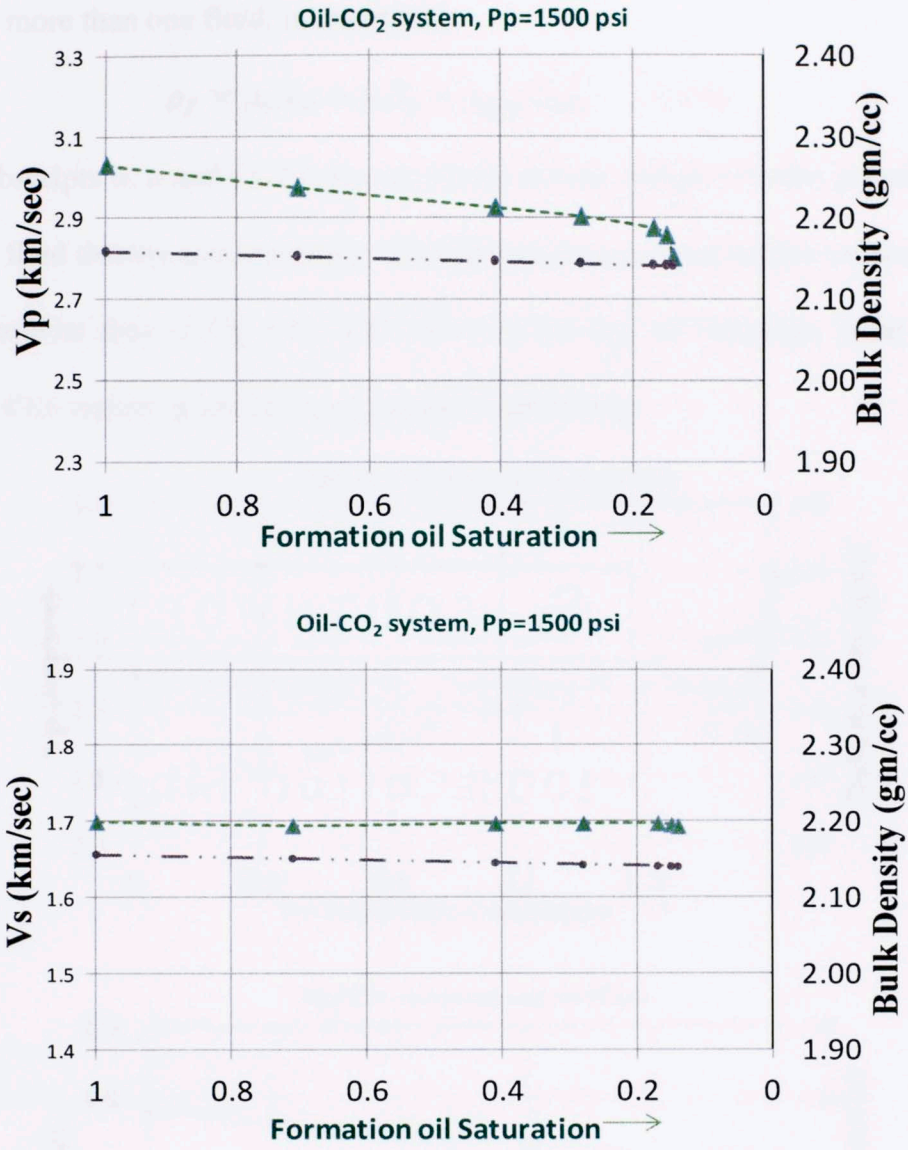

Figure 4.11 Measured P and S velocity (green) along with calculated bulk density (grey) variation when liquid CO_2 displaces oil for sample XX26.6 ft.

The P-velocity shows a linear decrease in Fig 4.11. The change in P-velocity is 5.1 % till the sample is saturated with 80% of the CO_2. For the remaining 5% saturation, the drop in P-velocity is 2.5%; overall change was 7.5%. S-wave velocity remains independent of saturation.

Biot-Gassmann theoretical velocities were estimated using Eqs 2.4 and 2.7. The required input parameters are either measured or estimated. The fluid density, which comprises more than one fluid, is calculated:

$$\rho_f = \rho_w S_w + \rho_o S_o + \rho_{CO2} S_{CO2} \quad \ldots (4.1)$$

Where, subscripts *w*, *o* and *CO2* represent water, oil and carbon dioxide. ρ and S denote individual fluid density and saturation. The theoretical estimated values are compared to the experimental data in Fig 4.12, 4.13 and 4.14 for dry, oil saturated, brine saturated and liquid CO_2 replacing oil saturated sample respectively.

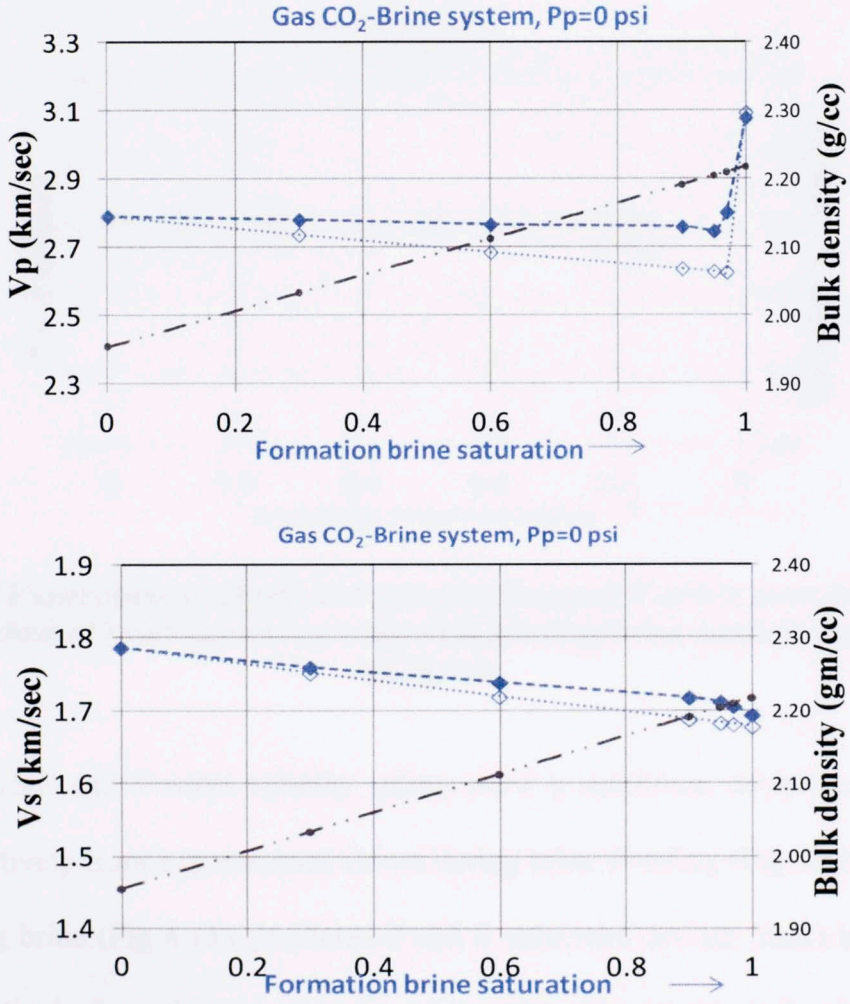

Figure 4.12: Experimental (filled) and theoretical (open) P and S wave velocity data as a function of brine saturation for sample XX26.6 ft

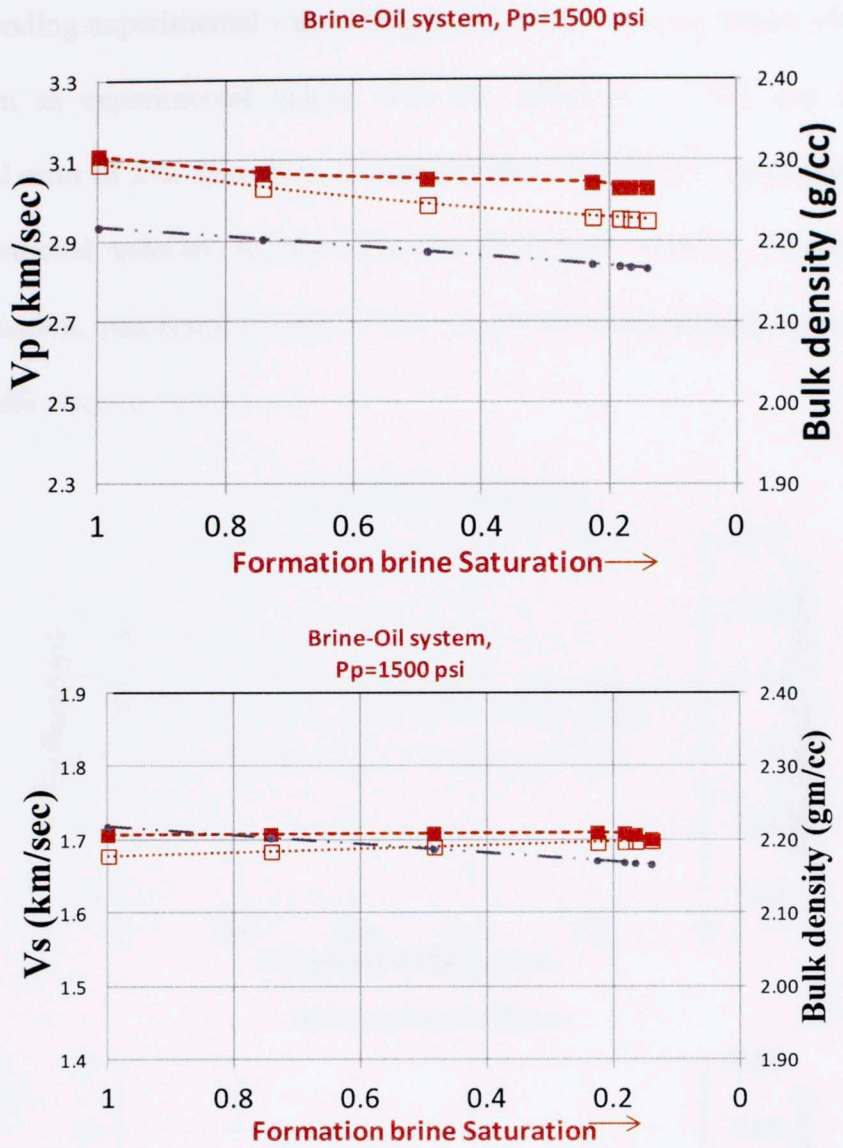

Figure 4.13 Experimental (filled) and theoretical (open) P and S wave velocity data as a function of brine saturation with oil displacing brine scenario for sample XX26.6 ft

The predicted P and S wave velocity values show a maximum deviation of 4% and 1.6% respectively from experimental values during brine flooding (Fig 4.12). In case of oil replacing brine (Fig 4.13), predicted P and S velocities deviate (max) by 2.6% and 0.8% respectively from the experimental values. When the sample is flooded by liquid CO_2 the theoretical P and S velocity deviate (max) by 10% and 0.1% respectively from

the corresponding experimental values (Fig 4.14). The P velocity values still follow the same pattern as experimental values with the difference of 4% and 2.6% within experimental error of 2%. Therefore, experimental P velocity is in good agreement with the Biot predicted velocity for the first two flooding scenarios. However, in CO_2 flooding situation, predicted P-velocity does not follow the experimental values and shows the difference of 10%.

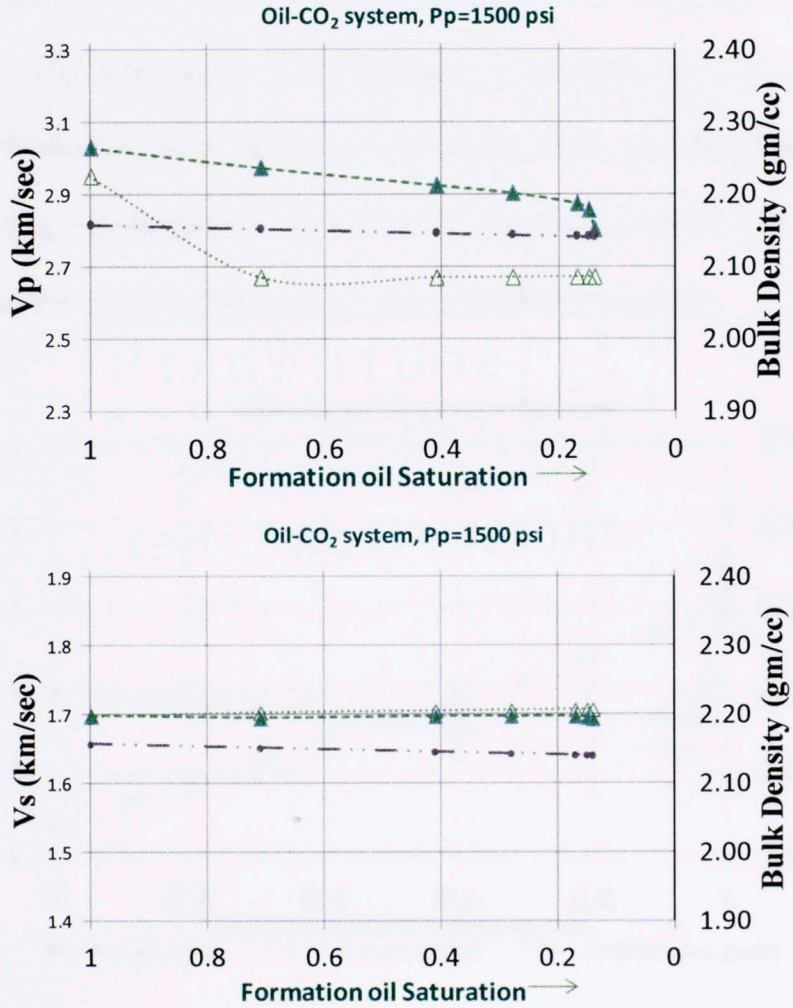

Figure 4.14: Experimental (filled) and theoretical (open) P and S wave velocity data as a function of liquid CO_2 saturation oil saturated for sample XX26.6 ft.

The plug from depth XX58 ft is selected for the next flooding experiment. The measured and theoretical P wave velocity is plotted in Fig 4.15. The velocity pattern of sample XX58 is observed to be similar to the previous sample XX26.6 ft. However, the values are found to be lower than the corresponding measured values of sample XX26.6 ft. The change in P velocity when the dry sample is saturated with brine is 2.3% till it reaches 95% of saturation. And then a steep rise of 14% was observed for the remaining 5% of saturation. S-wave velocity shows change of 8% from dry to 100% brine saturated state. Fig 4.16 shows 3.7% decrease in P-wave velocity as oil flooding proceeds till irreducible water saturation is reached. Later on, the change in P wave velocity from fully oil saturated to the end of CO_2 flooding is 6.83%. The shear velocity remains independent of the saturation for second and third scenarios.

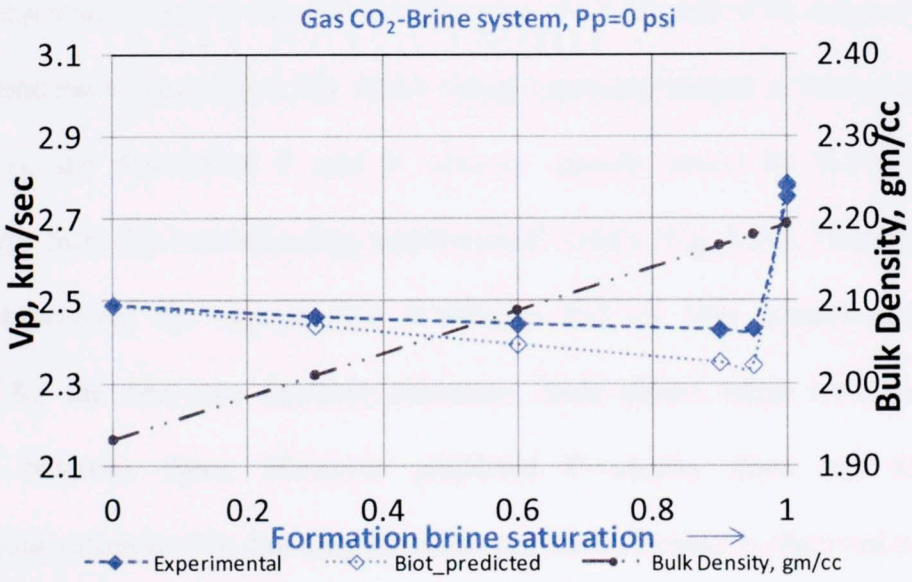

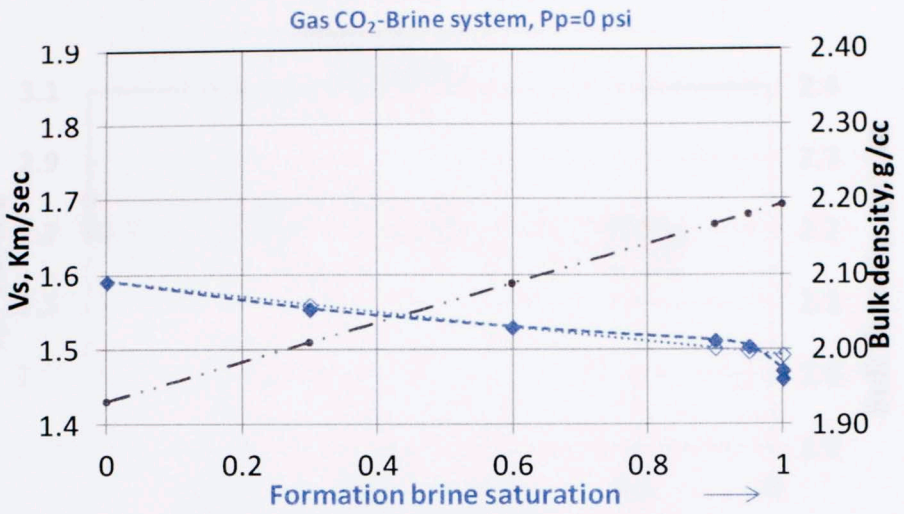

Figure 4.15: Experimental (filled) and theoretical (open) P and S wave velocity data as a function of brine saturation for sample XX58 ft.

The maximum difference in percentage between predicted and experimental P and S wave velocity is 3.7% and 1% respectively from dry to brine saturating state. In case of oil replacing brine, P and S velocity deviate (max) by 2.4% and 0.7% respectively from the experimental values (Fig 4.16). When the oil saturated sample is further flooded by liquid CO_2, the theoretical P and S velocity deviate (max) by 8.2% and 1.5% respectively from the corresponding experimental values (Fig 4.17). Therefore a good agreement between the experimental P velocity and the Biot predicted velocity is observed for the first two flooding scenarios. Both shows same trend with lower deviation between them. However predicted P-velocity does not follow the experimental values in CO_2 flooding situation and the difference is observed to be 8.2%.

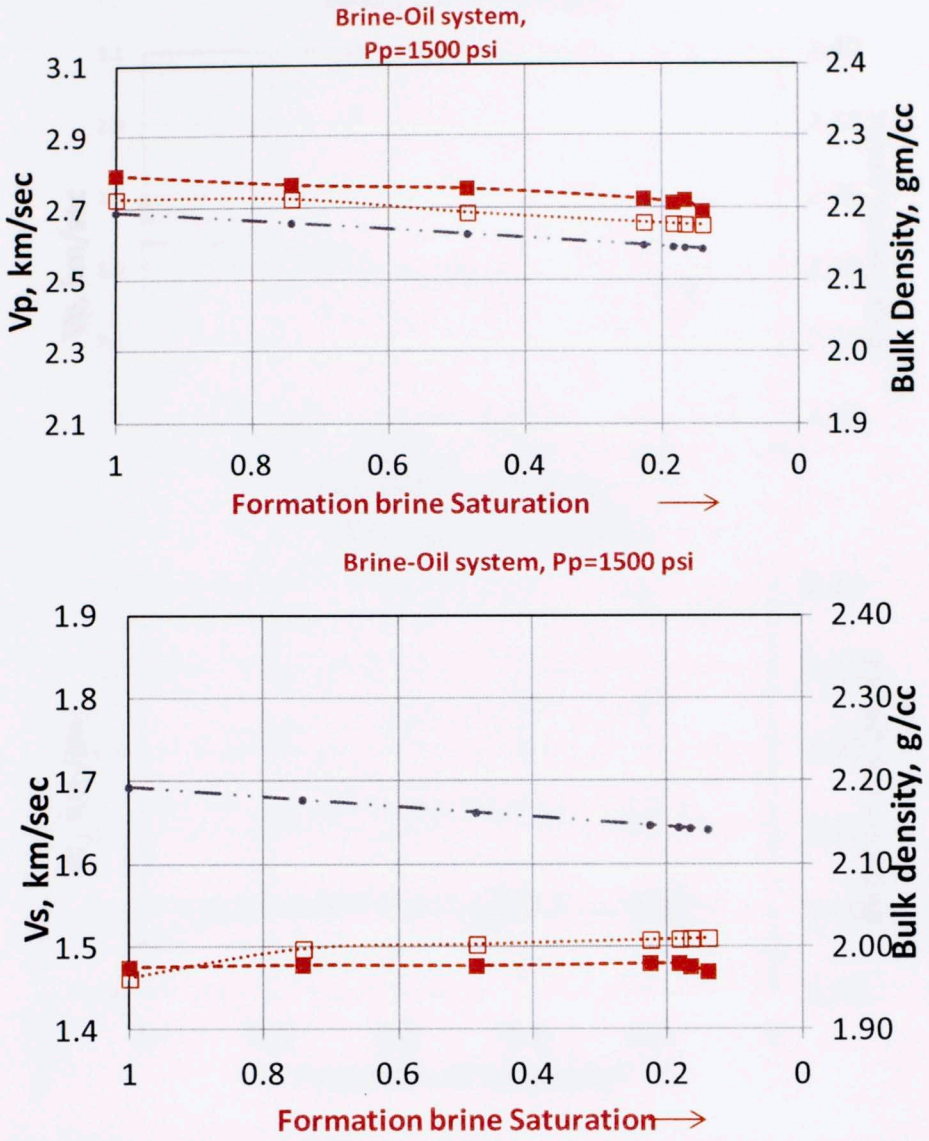

Figure 4.16: Experimental (filled) and theoretical (open) P and S wave velocity data for sample XX58 ft as oil replaces water

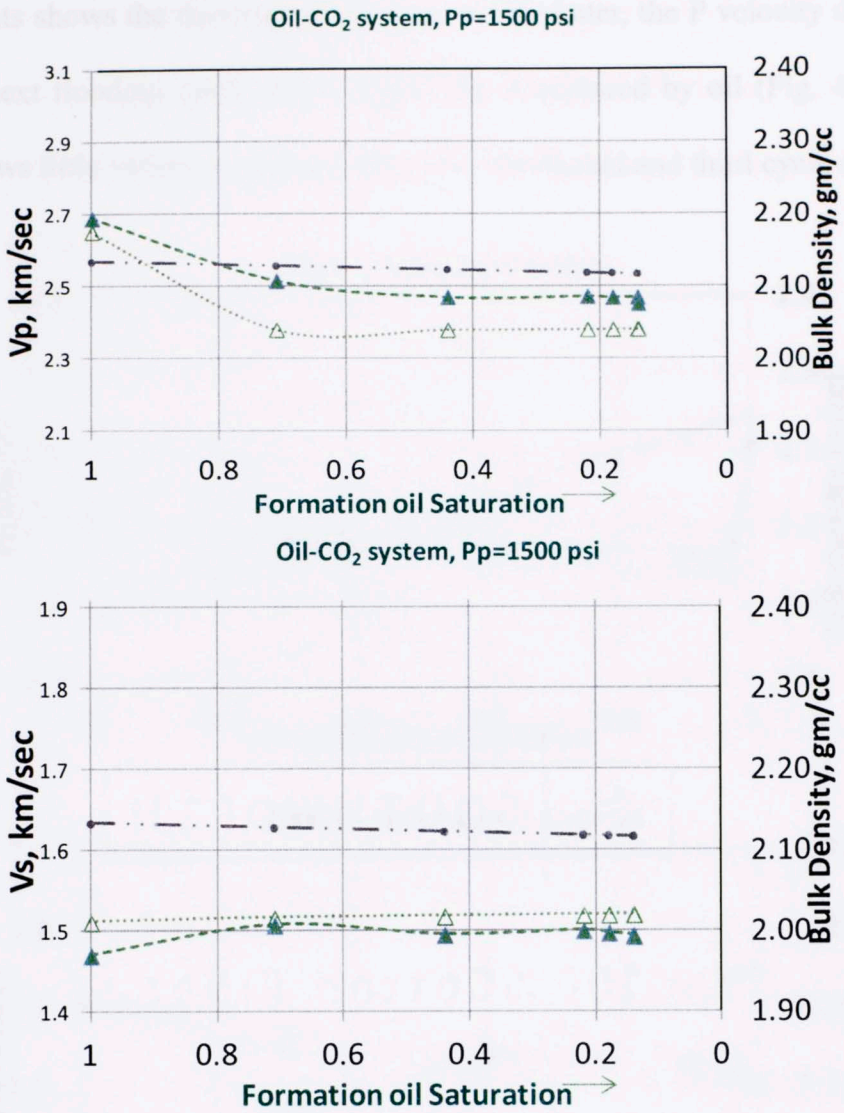

Figure 4.17: Experimental (filled) and theoretical (open) P and S wave velocity data as a function of liq. CO_2 saturation oil saturated for sample XX58 ft.

All the above flooding experiments were performed on Tuscaloosa sandstones. Two Paluxy sandstones between XX78 ft and XX83.5 ft were selected for next two experiments. For the sample from XX78 ft, P wave velocity decreases by 3.7% at 95% brine saturation and increases by 11% at the end of first cycle (Fig 4.18). On the other hand, S-wave velocity decreases by 6% till the end of the first cycle. In the next flooding cycle where oil is introduced to the brine saturated sample, the P velocity

measurements shows the decrease of 3% (Fig. 4.19). Later, the P velocity decreases by 4% in the next flooding cycle when liquid CO_2 is replaced by oil (Fig. 4.20). The S velocity shows little variation with saturation for the second and third cycle of flooding.

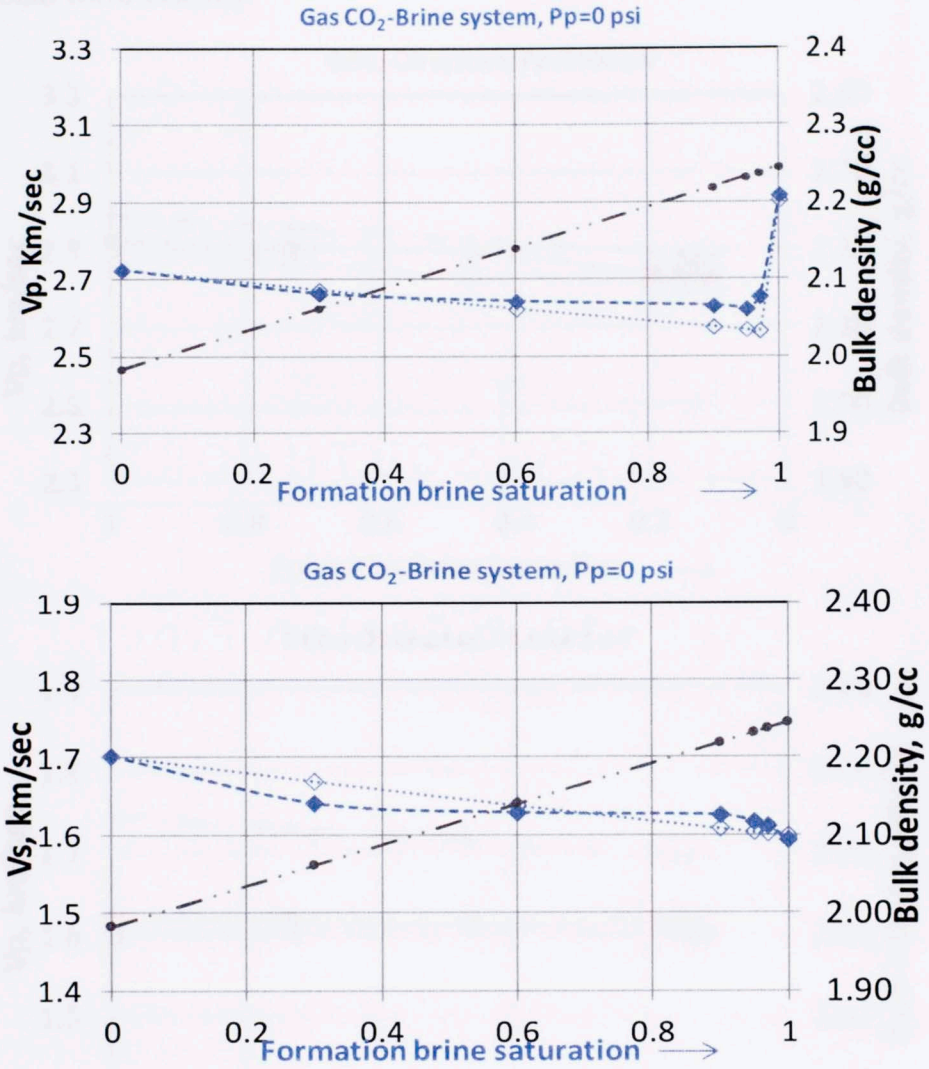

Figure 4.18: Experimental (filled) and theoretical (open) P and S wave velocity data as a function of brine saturation for sample XX78 ft

The predicted and experimental P and S velocity differ (max.) by 2% and 1.8%, respectively (Fig.4.18) for the brine saturation scenario. In oil flooding scenario, the difference in P and S-wave velocity is 2% and 1.4% respectively. Therefore, Biot-Gassmann theory is successful in predicting the experimental values for both the brine

and oil flooding scenarios. The predicted P and S wave velocity deviate from the corresponding experimental values by 7.4% and 4%, respectively in the third flooding scenario. And once again, the Biot-Gassmann theory fails in CO_2 flooding scenario for compressional wave velocity.

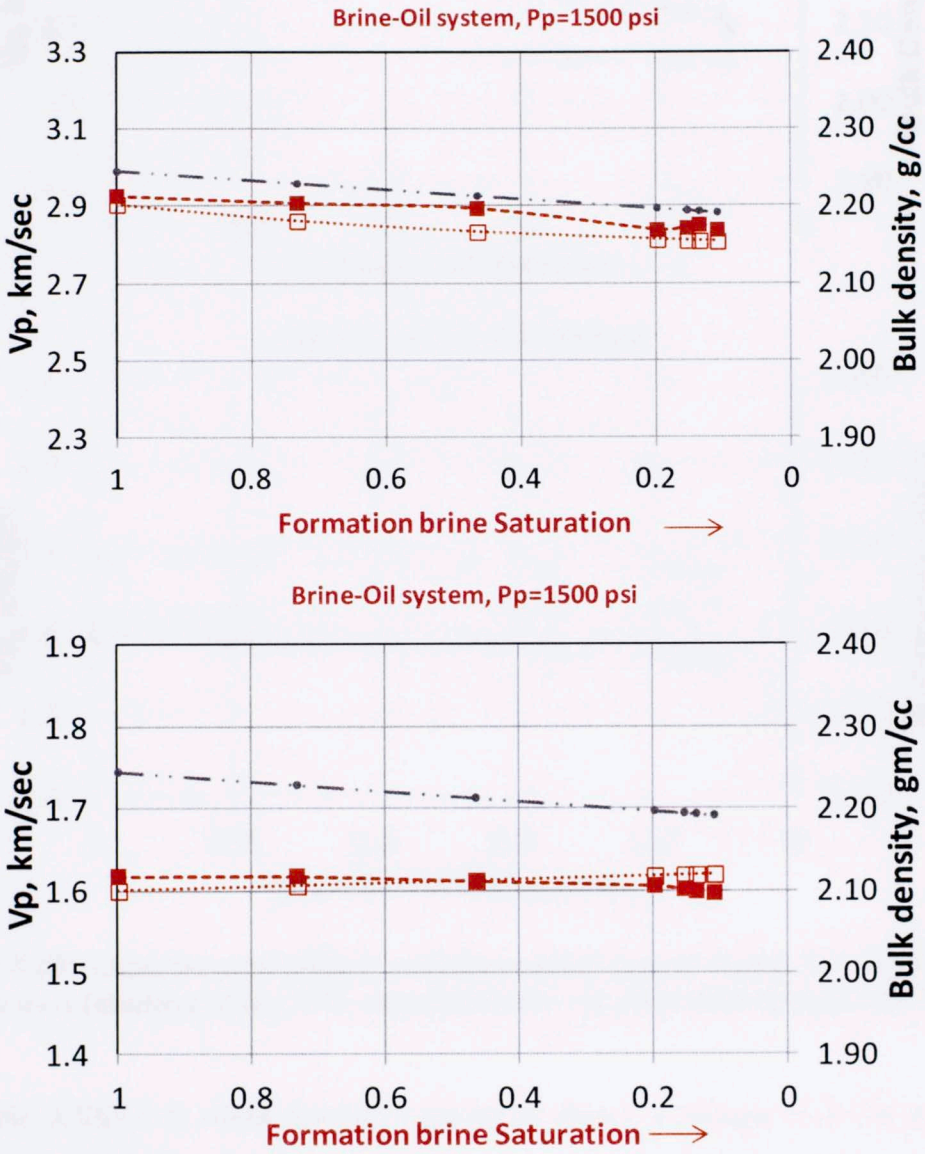

Figure 4.19: Experimental (filled) and theoretical (open) P and S wave velocity data for sample XX78 ft as oil replaces brine

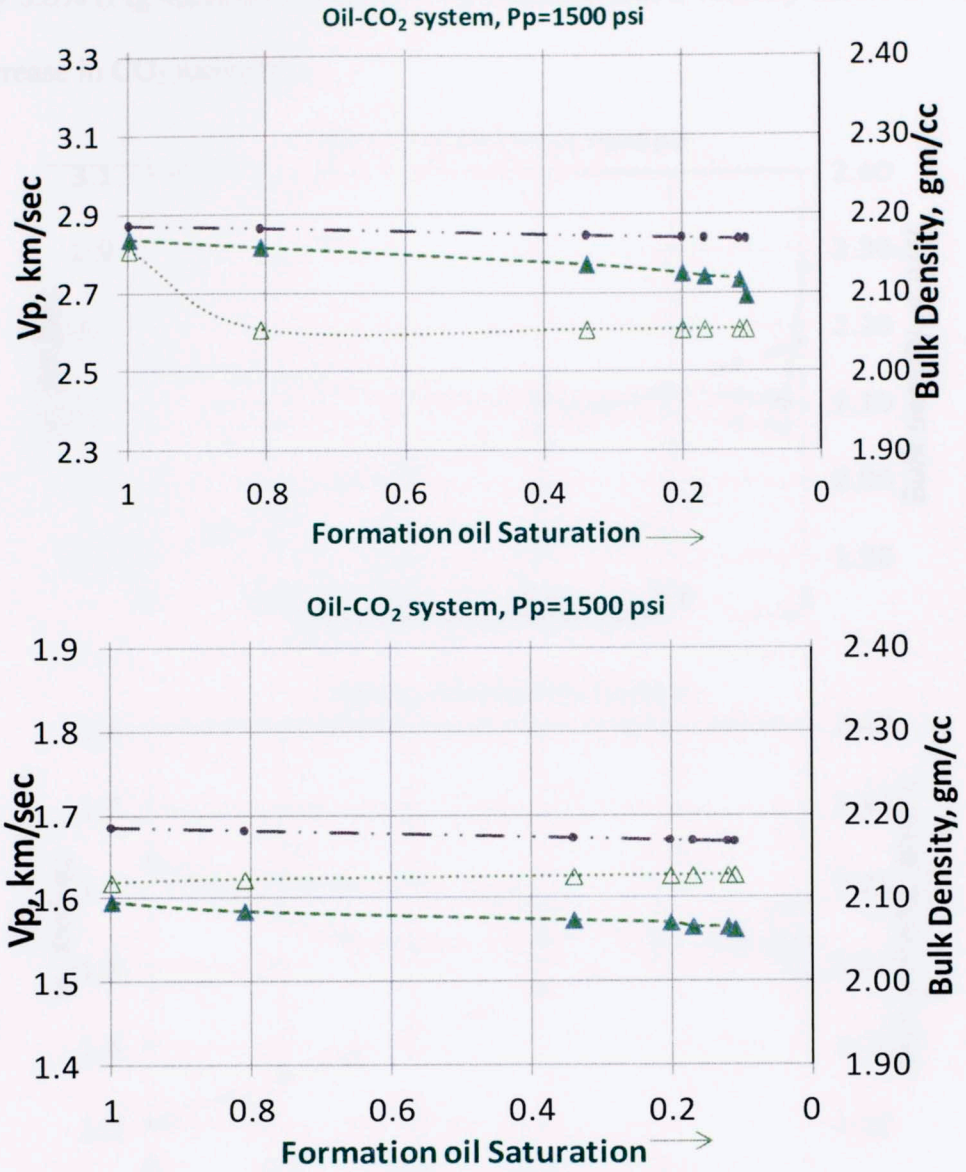

Figure 4.20: Experimental (filled) and theoretical (open) P and S wave velocity data as a function of liq. CO_2 saturation for oil saturated sample XX78 ft

The sample XX83.5 ft when flooded with brine shows a change of 6.7% in P wave velocity (Fig 4.21) until 95% of saturation is reached. 17% increase in P wave velocity is observed for the remaining 5% of saturation. The overall decrease in S velocity for the first flooding scenario is 9%. Later on, flooding oil decreases the P velocity by 3% while showing the negligible effect on S velocity (Fig 4.22). Thereafter, P velocity

drops by 8.6% (Fig 4.23) for the liquid CO_2 flooding. But S velocity shows no variation with increase in CO_2 saturation.

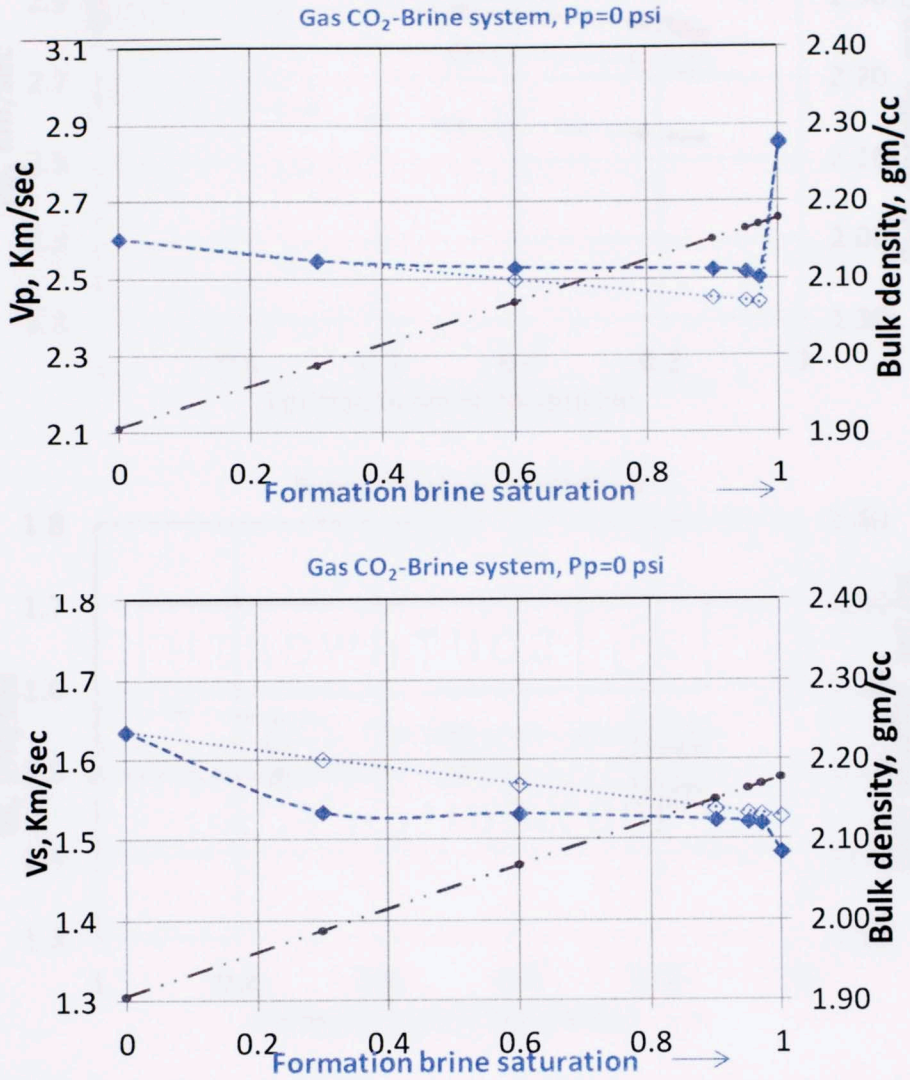

Figure 4.21: Experimental (filled) and theoretical (open) P and S wave velocity data as a function of brine saturation for sample XX83.5 ft.

For the brine flooding scenario, the predicted P and S velocity differ by 3% and 4% (max), respectively from the experimental values. Whereas for oil flooding scenario, the difference (in %) is 3.6% and 4.8% (max) respectively. In CO_2 flooding scenario, they differ by 8.8% and 5.7% respectively. The difference is larger in third case with a different trend of variation with saturation.

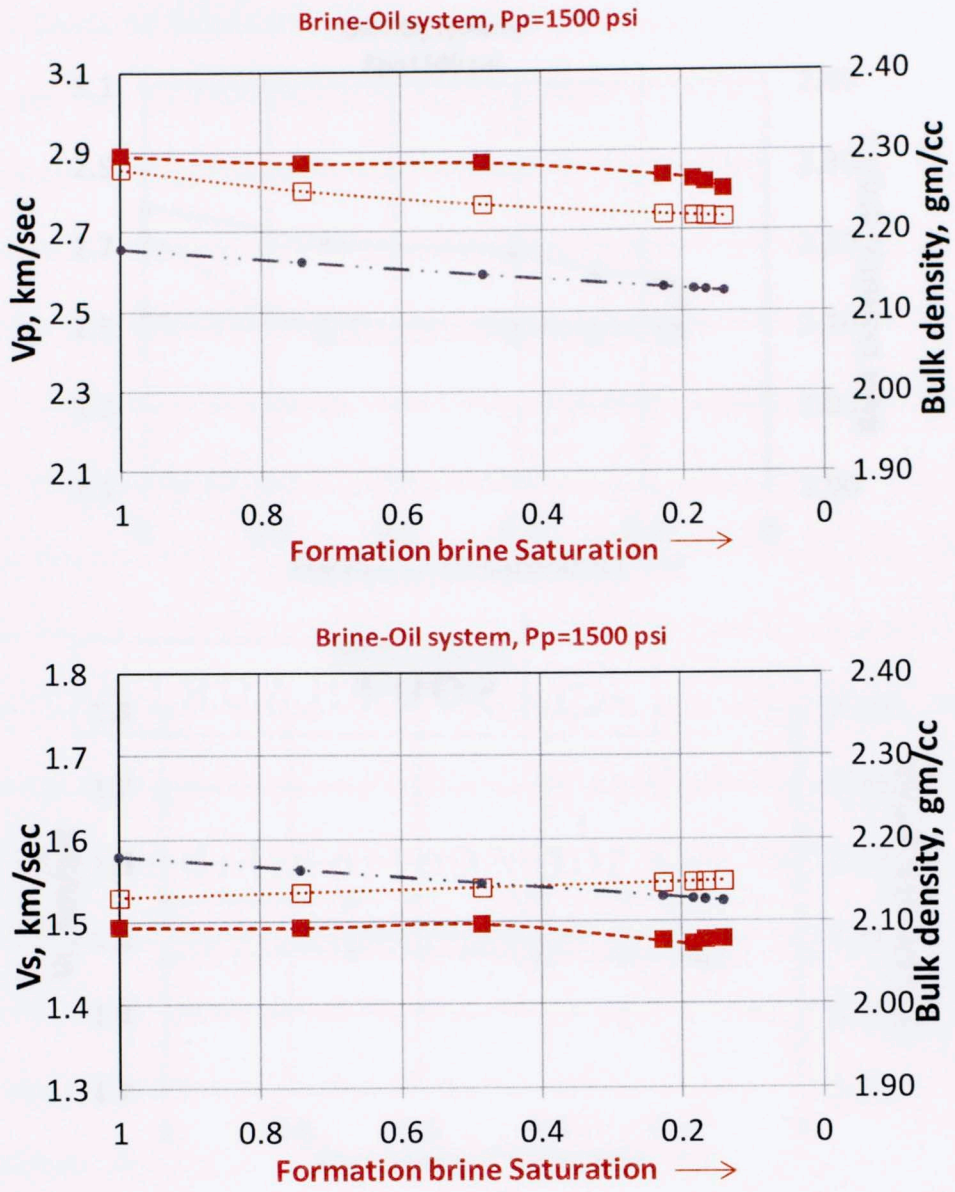

Figure 4.22: Experimental (filled) and theoretical (open) P and S wave velocity data for sample XX83.5 ft as oil replaces brine

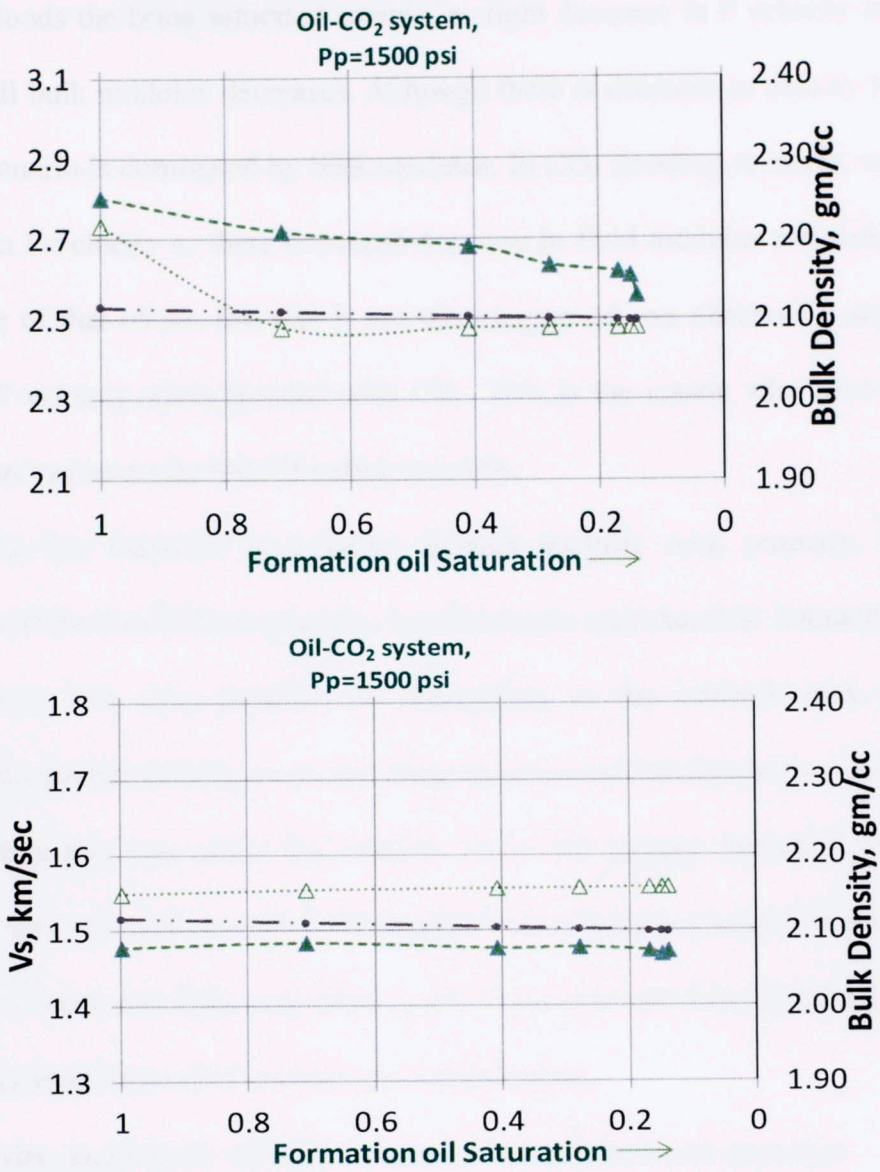

Figure 4.23: Experimental (filled) and theoretical (open) P and S wave velocity data as a function of liq. CO_2 saturation for oil saturated sample XX83.5 ft.

In all the samples, we see a systematic decrease in P and S velocity when saturated with brine. This is because density increases with flooding whereas bulk fluid modulus remains same in the order of that of gas. After saturation crosses 95%, bulk fluid modulus rises steeply to the order of brine. Therefore, we observe a high increase in P velocity whereas S velocity continues to decrease due to increasing density of the fluid.

When oil floods the brine saturated sample, a slight decrease in P velocity is observed since overall bulk modulus decreases. Although there is decrease in density too but the flooding scenario is dominated by bulk modulus. In CO_2 flooding scenario, we expect a high drop in P-velocity as there is overall decrease in fluid modulus and density is still in the order of that of oil. But this is not what happened; we observed a steady linear change in P velocity when flooded with CO_2. This is the reason why Biot-Gassmann theory doesn't agree to the third flooding scenario.

I investigate this behavior of velocity through intrinsic rock property, pore fluid properties and its distribution. Porosity measurements and chemical interaction in rock saturated with CO_2 may produce the uncertainty in the intrinsic rock properties. Combined properties of CO_2 in oil and brine mixture and its distribution in pore space are the factors that may affect the velocity across the sample. Sensitivity analysis of fluid properties and rock porosity to theoretical velocity values helped to determine the uncertainty in rock and fluid properties. Later, I speculate the fluid distribution must be 'patchy saturation' instead of uniform fluid distribution.

4.5 Sensitivity Analysis to velocity estimated using Gassmann equation

Sample chosen for sensitivity analysis is from depth XX79 ft. The predicted velocities are estimated for porosity values of 21%, 23% and 25%. The estimated fluid modulus is (K_f) decreased by 0.1, increased by 0.1 and 0.2 and estimated fluid density is decreased by 0.02, increased by 0.02 and 0.03. The estimated fluid properties used are shown below:

Fluid	K_f (GPa)	Density (gm/cc)
Brine	2.583	1.05
Oil	1.375	0.81

4.5.1 Case 1: Porosity : 21%, 23% and 25%

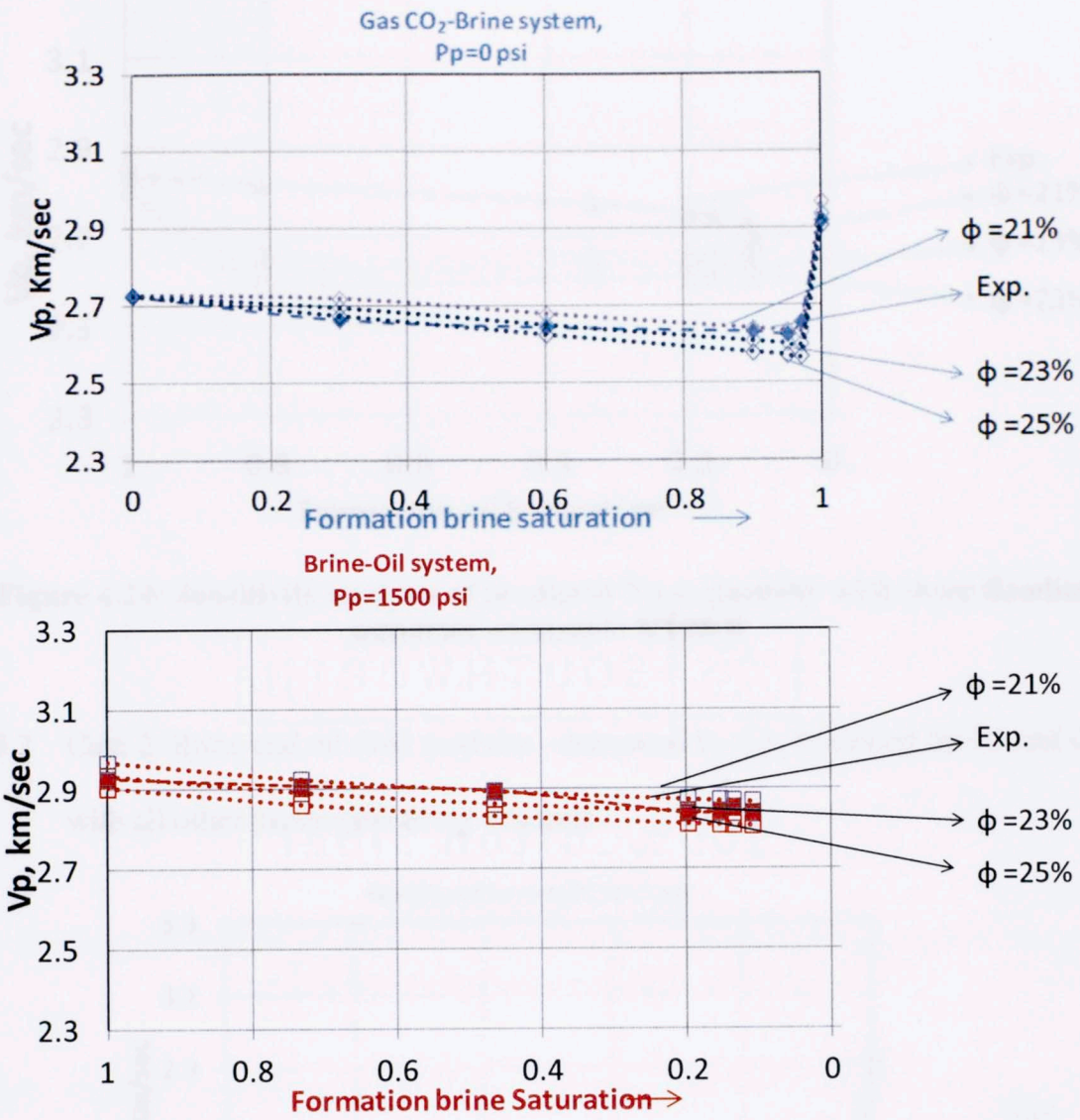

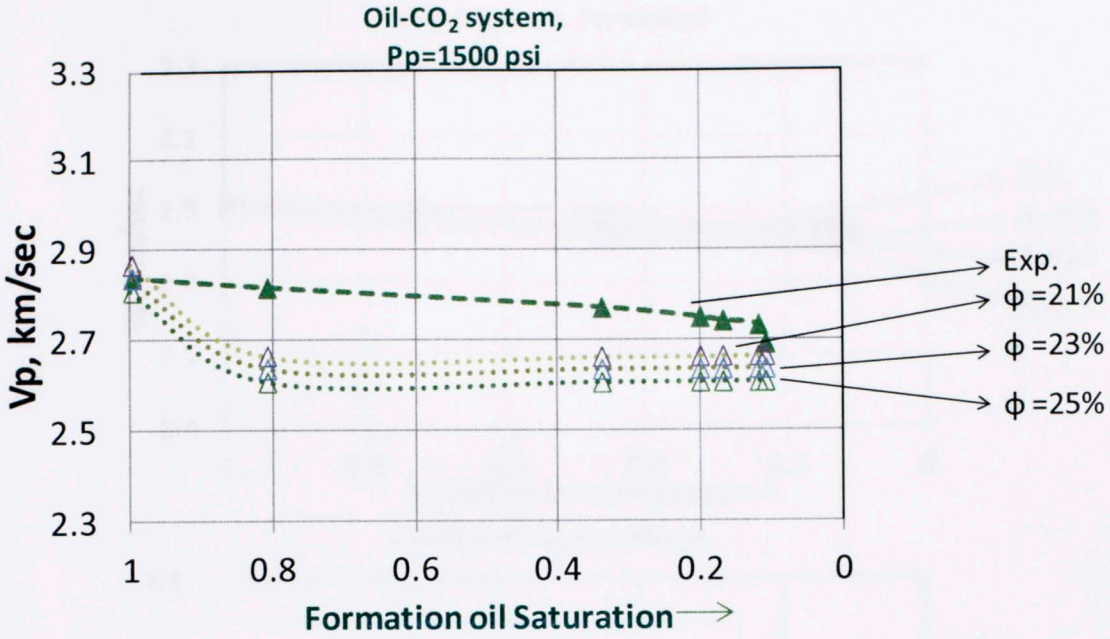

Figure 4.24: Sensitivity analysis of predicted Vp to porosity with three flooding scenarios on sample XX78 ft

4.5.2 Case 2: Brine and oil fluid modulus –decreased by 0.1, increased by 0.1 and 0.2 with all other parameters being constant

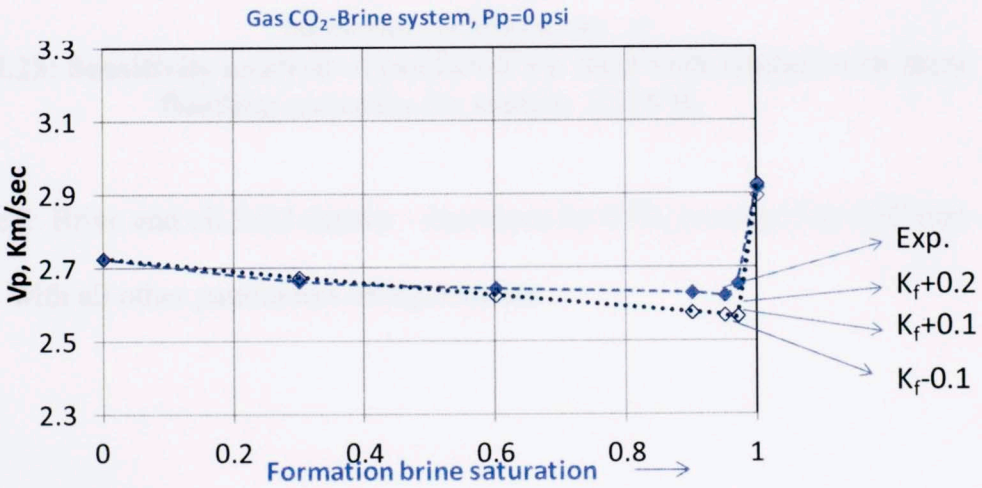

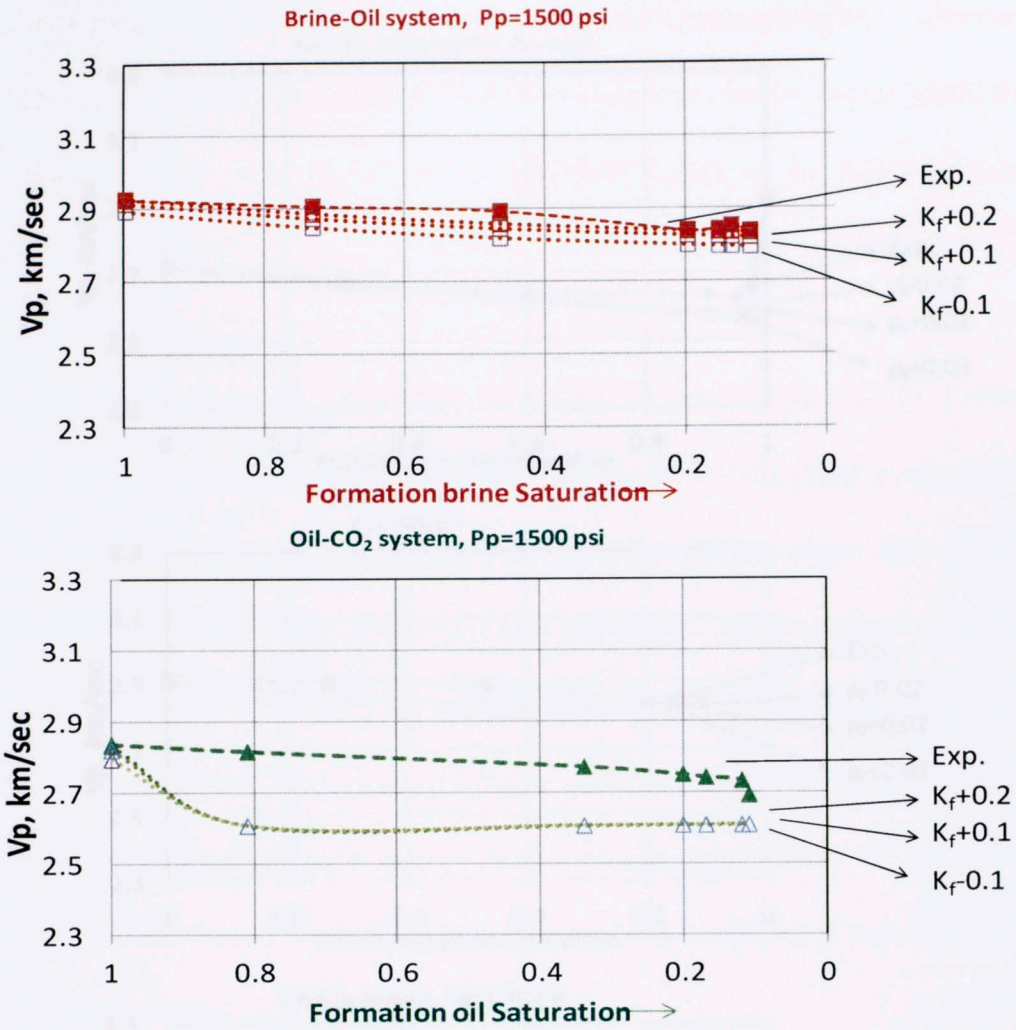

Figure 4.25: Sensitivity analysis of predicted Vp fluid bulk moduli with three flooding scenarios for sample XX78 ft.

4.5.3 Case 2: Brine and oil fluid density –decreased by 0.02, increased by 0.02 and 0.03 with all other parameters being constant

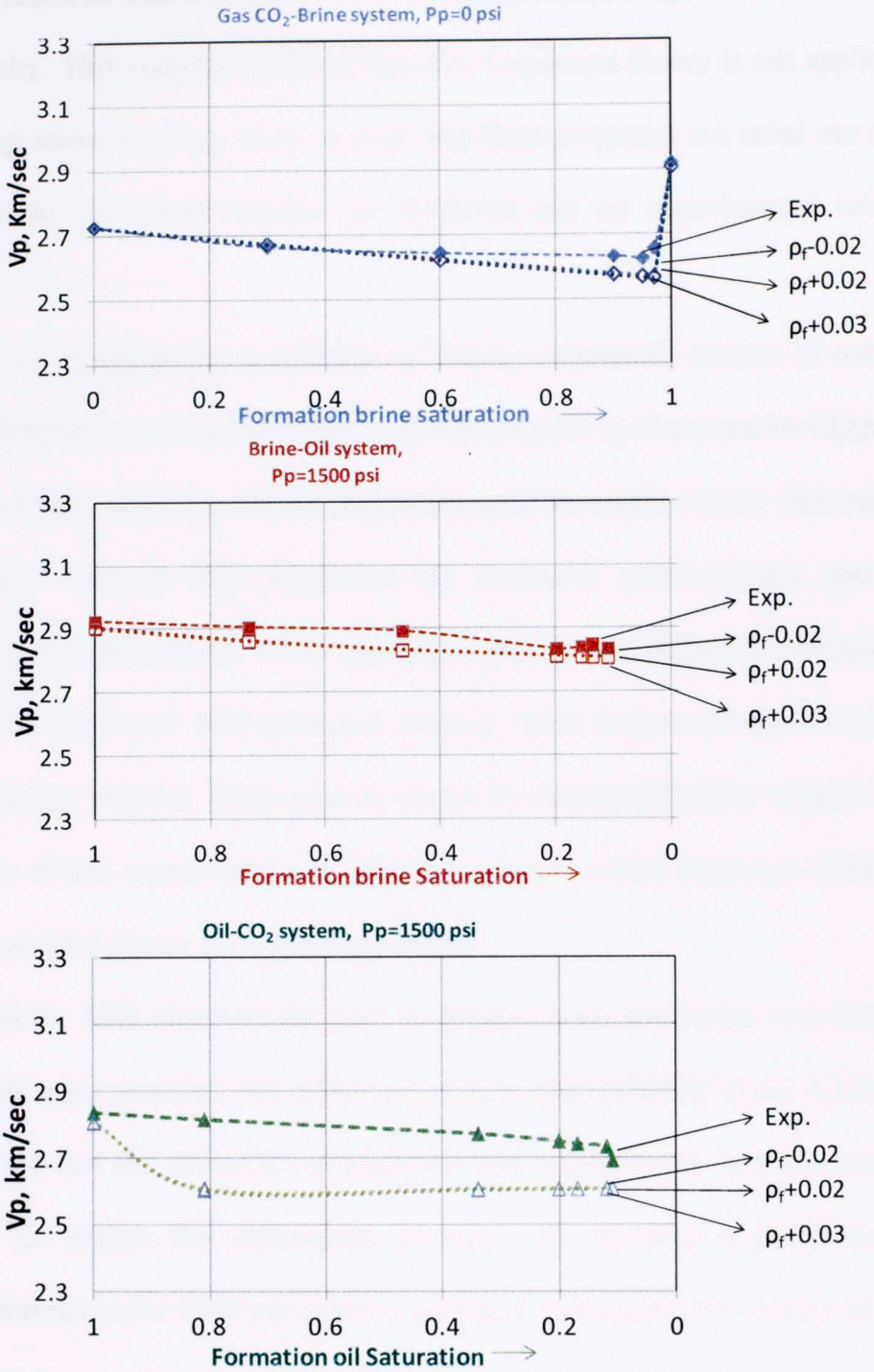

Figure 4.26: Sensitivity analysis of pred. Vp to fluid density with three flooding scenarios on sample XX78 ft

Sensitivity analysis shows that porosity is the major factor that affects the predicted P-velocity for all the three flooding scenarios whereas fluid modulus affects only the oil

flooding brine scenario. Density doesn't show any significant change in Biot-Gassmann predicted velocity. This analysis confirms that Biot-Gassmann theory is not applicable in CO_2 flooding scenario. Also, errors in rock and fluid properties are ruled out to be responsible for the mismatch between the predicted and the experimental velocity values.

The next step is to analyze the possibility of 'patchy saturation' instead of uniform saturation. A detailed overview on patchy saturation model is discussed in Chapter 2 sec. 2.8. Apart from patchy conditions, dispersion may be another factor that may be creating disparity between high frequency lab ultrasonic measurements and low frequency Biot-Gassmann model. Total velocity dispersion, as defined by Winkler, is the difference in calculated Biot predicted velocity (zero frequency) and frequency dependent measured velocity. Dispersion is caused by non-equilibration of pore fluid due to presence of low aspect cracks in saturated reservoir rocks. However, effects of dispersion are minimal due to the following reasons:

a. Winkler, 1986 observed decrease in dispersion on sandstones as a function of effective pressure. The effective pressure study (Chapter 4, sec 4.3.2) also proved that the difference in predicted and experimental data decreases as we go higher the differential pressure. As flooding experiments are performed under 1500 psi effective pressure (responsible for closure of most of the low aspect ratio cracks), dispersion is expected to be negligible.

b. The dispersion in shear velocity represents more reliable and is the true velocity dispersion (King, 1966; Winkler, 1986). As observed in all the shear

velocity measurements data, the predicted velocity values are equal or slightly greater than experimental data.

Since dispersion is out of question, patchy saturation is speculated as a primary reason of P velocity behavior as a function of saturation.

4.6 Patchy saturation condition

Theoretical P velocity is estimated under patchy saturation condition using Eq. 2.6 and plotted with experimental values in Fig 4.27. The input parameters for the patchy model such as bulk moduli and saturation values were determined experimentally.

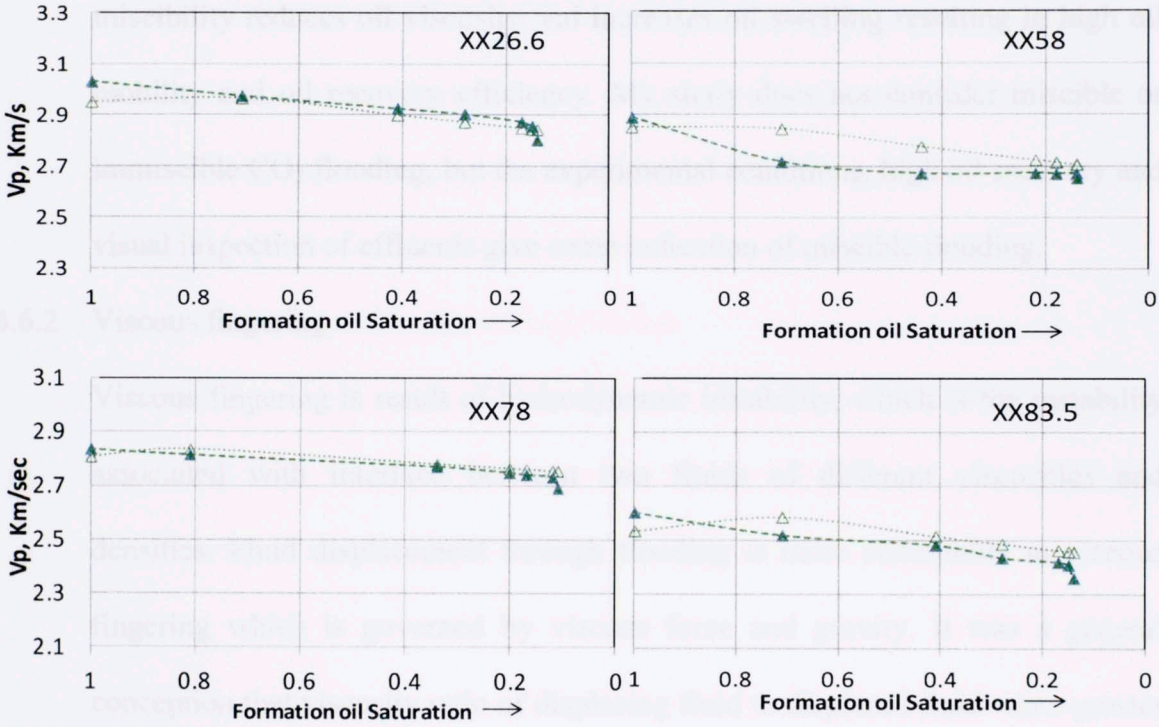

Figure 4.27: The patchy modeled P wave velocity (dotted) calculated using patchy model (Eq. 2.6) is better correlated to the experimental values in CO_2 flooding scenario.

On the contrary to the Biot-Gassmann theory, theoretical P-wave velocity estimated from effective bulk modulus of patchy saturation shows good agreement with the experimental data (Fig 4.27). Therefore, it is inferred that CO_2 distribution may be more

like "patchy" than uniform in oil saturated samples. Such linear velocity behavior can be easily inverted to saturation parameters. As discussed in Chapter 2 sec 2.2, there are two physical phenomenons which may favor patchy saturation:

4.6.1 Miscibility

Miscibility is the mixing of CO_2 and oil without any interface. The miscibility occurs when CO_2 flooding pressure is above minimum miscible pressure i.e 1500 psi (communicated through Richard, 2012). Miscibility enhances the oil recovery. The oil recovery in these experiments is 84% (average). The CO_2 miscibility reduces oil viscosity and increases oil swelling resulting in high oil mobility and oil recovery efficiency. My study does not consider miscible or immiscible CO_2 flooding, but the experimental conditions, high oil recovery and visual inspection of effluents give some indication of miscible flooding.

4.6.2 Viscous fingering

Viscous fingering is result of hydrodynamic instability, which is the instability associated with interface between two fluids of different viscosities and densities. Fluid displacement through flooding is more susceptible to viscous fingering which is governed by viscous force and gravity. It was a general conception that viscosity ratio of displacing fluid to displaced fluid when greater than 1 induces hydrodynamic instability (Dana and Skoczylas, 1999). But later mobility ratio was found to be more controlling factor (Cosentino, 2001). Maes et al. in 2010 used logarithm of mobility ratio (>1) to define the boundary of hydrodynamic instability. Since there is no data available on relative permeability of CO_2 in reservoir oil, casual calculations shows that log of

mobility ratio is greater than 1. However, CO_2 is a miscible fluid which reduces the effect of viscous fingering. The high mobility of CO_2 enhances fingering but is limited by the gravity (high density), capillary and miscibility effects (Garcia and Pruess, 2003). Since the previous studies were based on gas and water flooding; many other factors have to be considered for CO_2 flooding to confirm its behavior related to viscous fingering.

Patchy saturation may be outcome of any of the above phenomenon individually or together. However, miscibility effects seem more likely to cause patchy saturation that directly impacts P-velocity and impedance. The experiments in this study are limited to analysis of fluid saturation and velocity behavior and therefore, more rigorous experiments are required to characterize the fluid flow phenomenon that leads to patchy saturation.

4.7 Impedance behavior with various fluid fronts

The product of measured velocity with density yield impedance. The P and S impedances are plotted for all samples in Fig 4.28, 4.29 and 4.30 for brine, oil and liquid CO_2 flooding scenarios respectively.

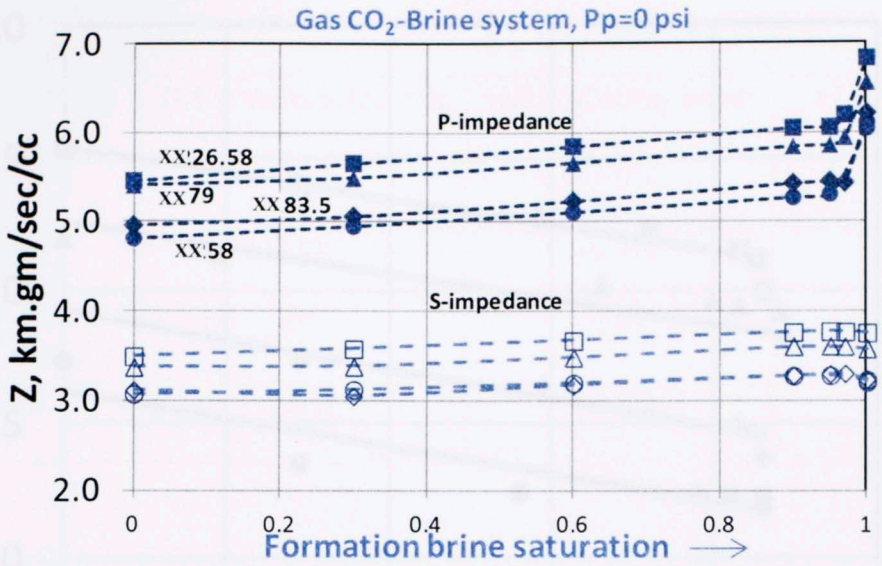

Figure 4.28: The P and S impedance for all four samples calculated in Brine flooding scenario.

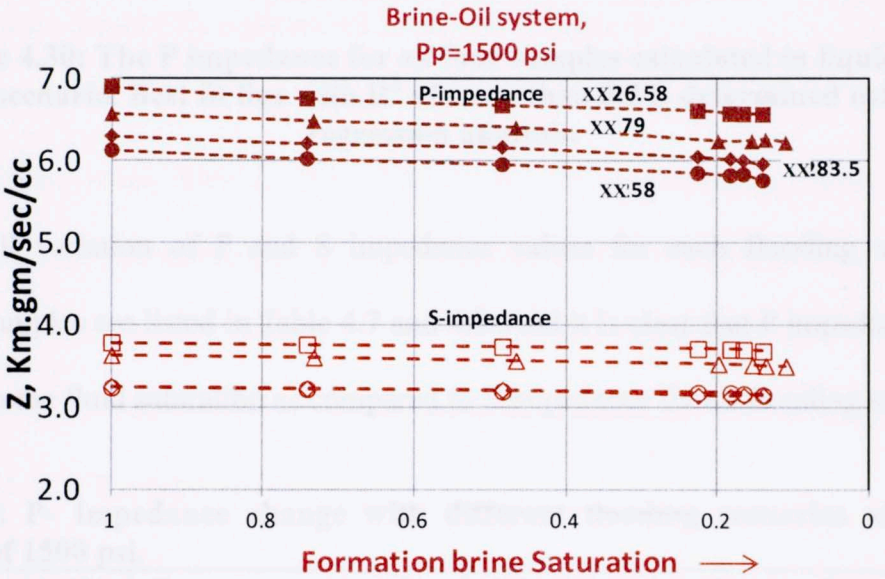

Figure 4.29: The P and S impedance for all four samples calculated in oil flooding scenario

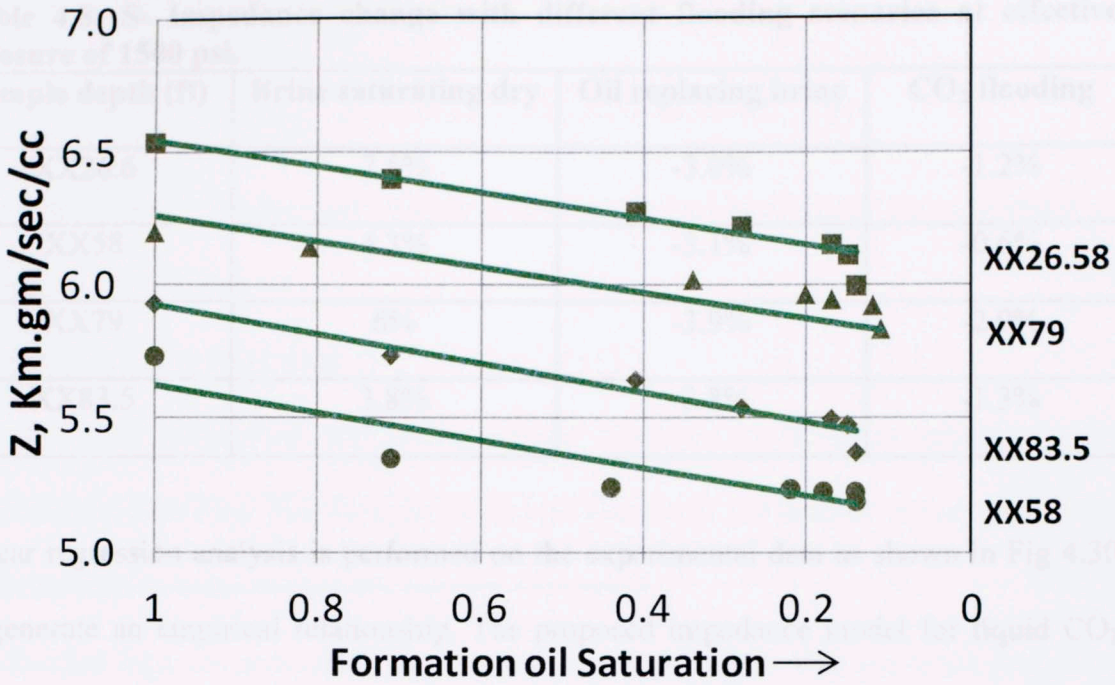

Figure 4.30: The P impedance for all four samples calculated in liquid CO_2 flooding scenario. Best fit line with R^2 of more than 0.9 is determined using linear regression analysis.

The overall variation of P and S impedance values for each flooding scenario in different samples are listed in Table 4.7 and 4.8. And it is clear that P impedance is nore sensitive to the fluid saturation as compared to S impedance for all flooding scenarios.

Table 4.7: P- Impedance change with different flooding scenarios at effective pressure of 1500 psi.

Sample depth (ft)	Brine saturating dry	Oil replacing brine	CO_2 flooding
XX26.6	25%	-5.3%	-8.4%
XX58	27%	-6.3%	-9.6%
XX79	21%	-5.6%	-5.9%
XX83.5	25%	-5.8%	-9.5%

Table 4.8: S- Impedance change with different flooding scenarios at effective pressure of 1500 psi.

Sample depth (ft)	Brine saturating dry	Oil replacing brine	CO_2 flooding
XX26.6	7.5%	-3.0%	-1.2%
XX58	4.3%	-3.1%	-0.6%
XX79	6%	-3.9%	-2.9%
XX83.5	3.8%	-3.8%	-1.3%

Linear regression analysis is performed on the experimental data as shown in Fig 4.30 to generate an empirical relationship. The proposed impedance model for liquid CO_2 flooding where liquid CO_2 replaces oil in sample is given as:

$$\boldsymbol{I_c = rS_o + I_{co}} \qquad \ldots (4.2)$$

Where, r is the slope between P-impedance and oil saturation, $\boldsymbol{S_o}$ (with irreducible water saturation). The intercept, I_{co} is the impedance of CO_2 saturated rock (with some immovable oil and water). Values of r for all the four plugs are found to be close to 0.5.km.gm/cc/sec. The R-squared for the linear fit is found to be more than 90% which shows good fit to the experimental data.

Since it is not feasible to determine the intercept ($\boldsymbol{I_{co}}$) in Eq. 4.2 as it requires a considerable amount of time for a well to reach CO_2 flooded state with immovable oil/brine, we consider a boundary condition for a region with no CO_2 in order to eliminate the intercept. Therefore, in this region, $S_o = 1$, $I_c = I_o$, where I_o is the impedance of the sample saturated with oil and water (preferably oil).

The above condition is applied to Eq. (4.2).

$$\Rightarrow \quad I_o = r + I_{co} \qquad \ldots (4.3)$$

Using Eq. (4.2) and (4.3), the saturation of CO_2 is determined as

$$S_{CO_2} = \frac{[I_o]_{preflooded} - [I_c]_{postflooded}}{r} \ldots (9)$$

This empirical relationship can be applied to acoustic logs or seismic data to estimate the saturation of CO_2.

4.8 Application to field data

The empirical correlation and patchy model confirms to be more reliable to the experimental data than Biot-Gassmann theory. Therefore, the models are applied to the available logs in order to quantify the CO_2 saturation.

Pre flooded logs are available from a well from Delhi field. The expected formation fluids are brine and oil. The available field pre flooded logs are the basis of substituting oil/brine by CO_2.

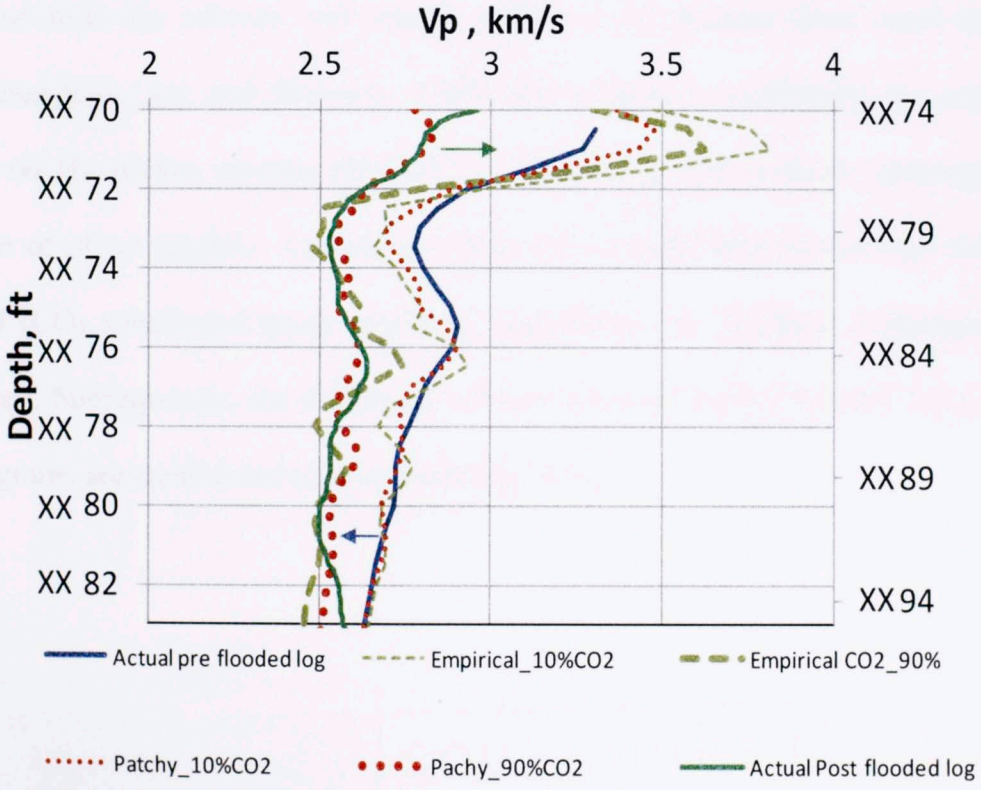

Figure 4.31: Field pre-flooded and post-flooded Vp and Vs logs

as a function of depth. Predicted Vp from patchy saturation condition (red) and our correlation (green) are computed by 10% and 90% CO_2 replacements. This is compared to available post-flooded logs.

We use Eq. 2.6 (patchy model) and Eq. 4.2 (empirical correlation) to estimate the P and S wave velocity values at CO_2 saturation of 10% and 90%. Fig 4.31 clearly shows that both equations 2.6 (patchy) and 4.2 (empirical) estimate the CO_2 saturation to be around 90% in the Paluxy region. The irregularities in the empirical predicted velocity above depth XX72 ft in Fig 4.31 is caused due to bulk density measured in log. It is found that the estimated velocities from the empirical correlations are highly sensitive to density, unlike patchy saturation conditions.

These logs are used to create 2D synthetic seismic as mentioned in chapter 3 sec 3.7. The 2D synthetic seismic is created from the reflection coefficient values which are estimated from the velocity and density values of pre flooded (base case) and CO_2 substituted logs (Aki and Richards, 1980). The reflection coefficients are convolved with a 60 Hz Ricker wavelet (Fig 4.32) to generate a 2D synthetic seismogram as function of offset (angles). Therefore, a base 2D synthetic seismogram and three post flooded (CO_2 substituted using empirical correlation) 2D synthetic seismograms are generated. Subsequently, the difference between the post and pre flooded 2D synthetic seismograms are created and plotted (refer Fig. 4.33)

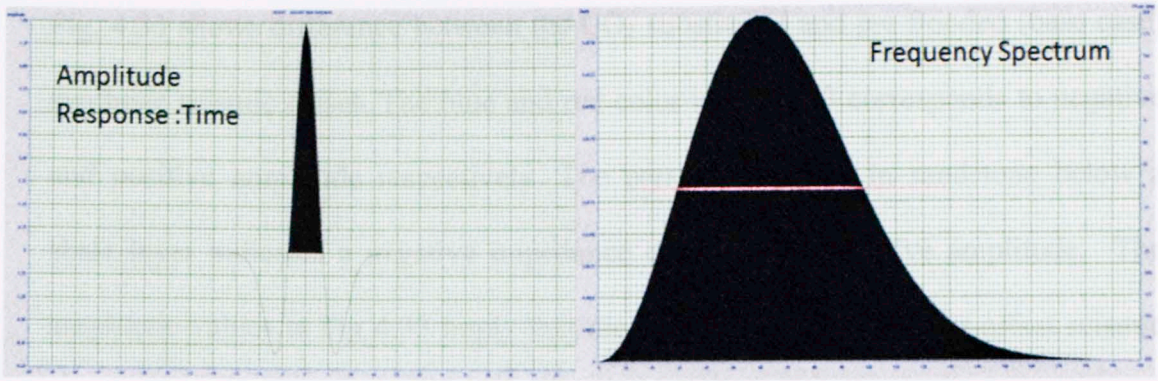

Figure 4.32: Ricker wavelet of 60 Hz frequency and 120 ms length used to create Aki Richard synthetic seismogram

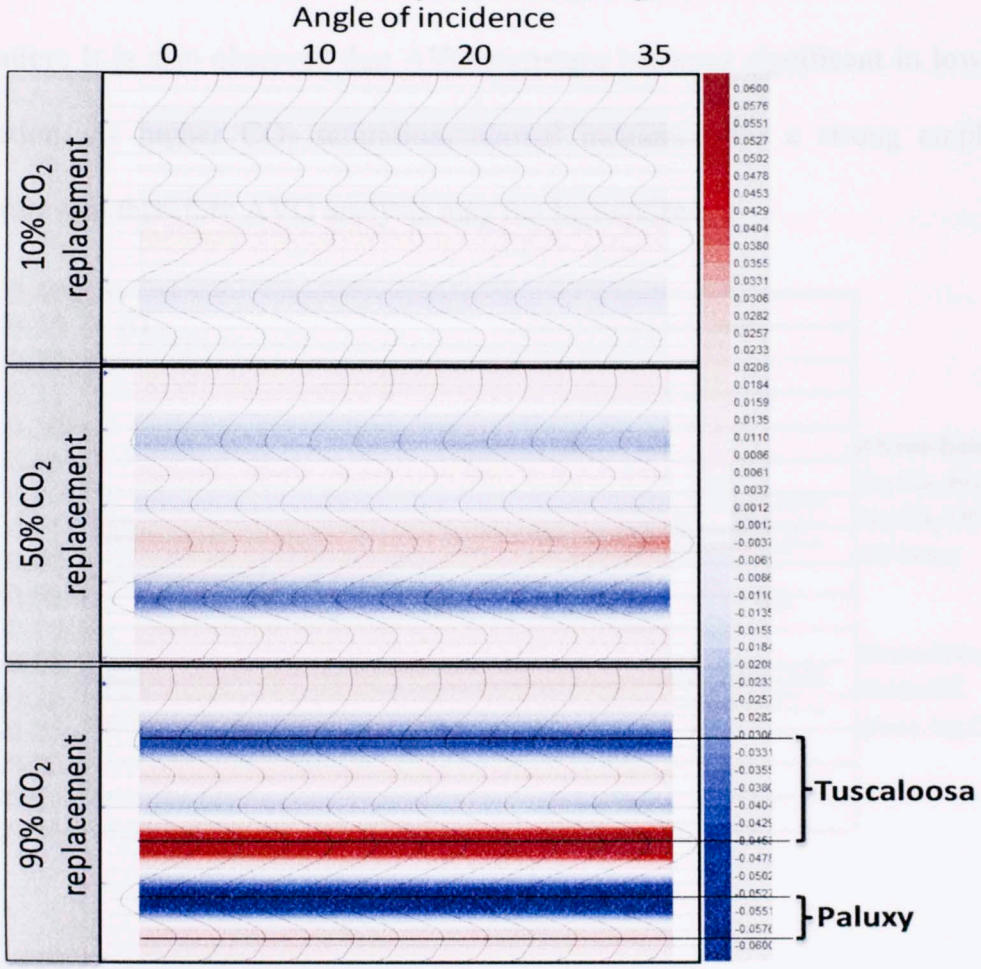

Figure 4.33: Seismic amplitude difference as function of offset and CO_2 saturation for reflection from Tuscaloosa and Paluxy interfaces. The base case is pre CO_2 flood condition when the formation is saturated with oil and water.

Fig. 4.33 shows difference between the CO_2 substituted and pre flooded (base case) synthetic seismic offset. The blue and red color in Fig 4.33 corresponds to negative and positive amplitude respectively. The presence of CO_2 in sandstone below a shale layer indicates a negative impedance contrast and negative amplitude. The amplitude values in Fig 4.33 imply that the normal incidence and far offset seismic can detect CO_2 saturation of 50% or more at the Tuscaloosa and Paluxy interfaces. This confirms the feasibility of 4D seismic to map CO_2 flood front above mentioned saturation. It is also observed that AVO signature becomes significant in low CO_2 saturation. At higher CO_2 saturation, normal incidence has a strong amplitude signature and therefore AVO analysis may not be required.

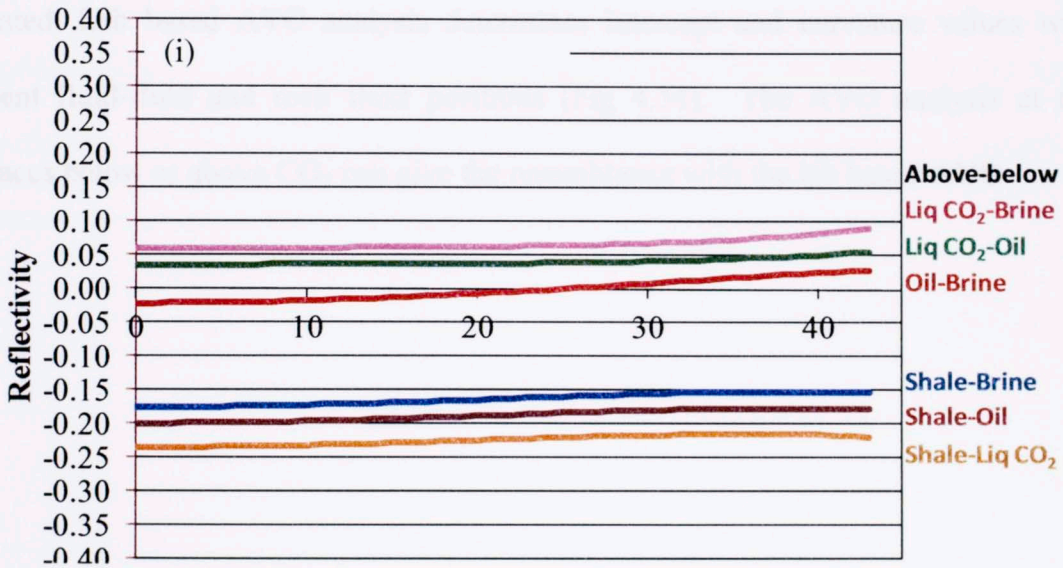

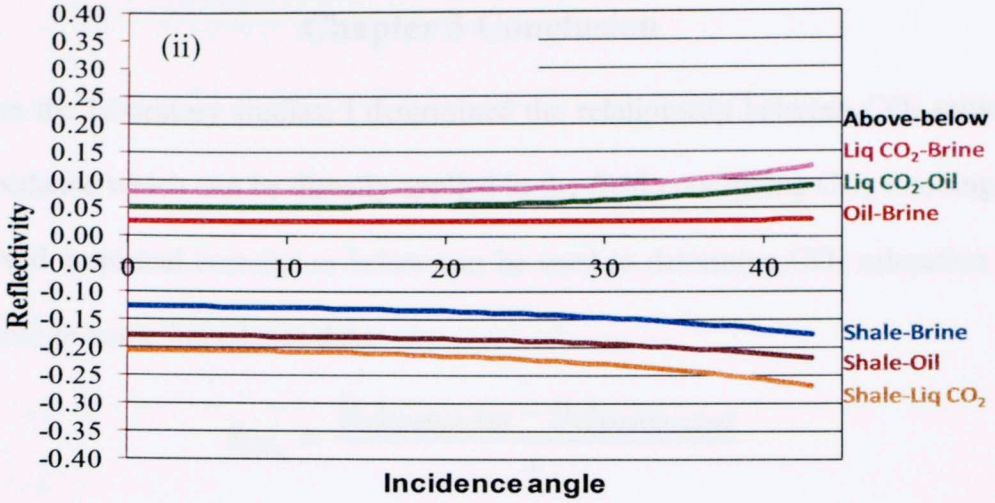

Figure 4.34: Lab based AVO analysis created for different fluid and rock scenarios in Tuscaloosa (i) and Paluxy (ii) formation

After the AVO analysis on field data, AVO signature from laboratory measurements is estimated. Lab based AVO analysis determines intercept and curvature values with different fluid-fluid and rock fluid positions (Fig 4.34). The AVO analysis at the interfaces below or above CO_2 can give the resemblance with the lab based AVO.

Chapter 5 Conclusion

Based on the laboratory studies, I determined the relationship between CO_2 saturation and impedance which can be directly applied in the field undergoing CO_2 flooding. The lab derived empirical correlation below can be used to determine CO_2 saturation from the seismic or sonic impedance data.

$$S_{CO_2} = \frac{[I_o]_{preflooded} - [I_c]_{postflooded}}{r}$$

The other conclusions from this study:

5.1 Compressional velocity behavior with CO_2 flooding cannot be adequately described by Biot-Gassmann theory. Patchy saturation condition fits better with the experimental data.

5.2 Velocity behavior in effective pressure study indicates that the Biot effective stress coefficient, 'n' is less than unity in liquid CO_2 saturated sandstone in contrary to previous published n values on brine saturated Berea sandstones where $n \geq 1$.

References

1. Advanced Resources International, 2006, Undeveloped domestic oil resources: the foundation for increased oil production and a viable domestic oil industry. US DOE, http://www.fossil.energy.gov/programs/oilgas/publications/eor_co2/Undeveloped_Oil_Document.pdf , February 2006.
2. Aki, K., and Richards, P., G. 1980. Quantitative Seismology. New York: Freeman and Co.
3. Alsos, T., Eide, A.L., Hegstad, B. K., Najjar N. F., Astratti, D., Doyen, P., and Psaila, D. 2002. From quantitative to quantitative 4D seismic analysis of the Gullfaks field. 64th conference and exhibition, EAGE, Extended Abstracts
4. Arts, R., Eiken, O., Chadwick, A., Zweigel, P., Van der Meer, L. and Zinszner, B. 2004. Monitoring of CO_2 injected at Sleipner using time-lapse seismic data. *Elsevier* **29** (9-10): 1383-1392. http://dx.doi.org/10.1016/j.energy.2004.03.072.
5. Ballard B.D. 2007. Quantitative mineralogy of reservoir rocks using Fourier Transform Infrared Spectroscopy, SPE 113023-STU, Presented at Annual Technical Conference and Exhibition, Anaheim, California, 11-14 November.
6. Batzle, M. and Christiansen, R. 1998. Reservoir recovery processes and geophysics. *The Leading Edge* **17** (10): 1444-1447.
7. Batzle, M., Christiansen, R. and Han, D-H., 1998, Reservoir recovery processes and geophysics: The leading Edge 17: 1444-1447.
8. Batzle, M. and Wang, Z. 1992. Seismic properties of pore fluids. *Geophysics* **57** (11): 1396-1408.

9. Barclay, S.A. and Worden, R.H. 2000. Geochemical modeling of digenetic reactions in a sub-arkosic sandstones. *Clay Minerals* **35**: 57-67.

10. Benson, S.M. and Cole, D.R. 2008. CO_2 Sequestration in deep sedimentary formations. *ELEMENTS* **4** (5): 325-331.

11. Berryman, J. G., and Wang, H. F., 2000, Elastic wave propagation and attenuation in a double-porosity dual-permeability medium: Int. J. of Rock Mech. and Min. Sci. **37**(1-2): 63–78.

12. Biot, M. A. 1956. Theory of propagation of elastic waves in a fluid saturated porous solid. I. Low frequency range and II. Higher-frequency range: Acoust. Soc. Am. **28**: 168–191.

13. Bui, L. H. 2010. Near-Miscible CO_2 application to improve oil recovery. MS thesis, University of Kansas, Lawrence, Kansas (July 2010).

14. Chadwick, A., Williams, G., Delepine, N., Clochard, V., Labat, K., Sturton, S., Buddensiek, M., Dillen, M., Nickel, M., Lima, A. L., Arts, R., Neele, F., Rossi, G. 2010. Quantitative analysis of time-lapse seismic monitoring data at the Sleipner CO_2 storage operation. *The Leading Edge* **29** (2): 170-177.

15. Christensen, N. I. 1984. Pore pressure and oceanic crustal seismic structure. Geophysical Journal of the Royal Astronomical Society **79** (2): 411-423.

16. Cosentino, L. 2001. Integrated Reservoir Studies. Paris. Institut Francais Du Petrole Publications. Page-189.

17. Christensen, N. I. and Wang H. F. 1985. The influence of pore pressure and confining pressure on dynamic elastic properties of Berea sandstone. *Geophysics* 50 (2): 207-213.

18. Dana, E. and Skoczylas, F. 1999. Gas relative permeability and pore structure of sandstones. *Int. J. Rock Mech. Min. Sci.* **36**: 613-625

19. Davis, T. L., Terrell, M. J. and Benson, R. D. 2003. Multi-component seismic characterization and monitoring of the CO_2 flood at Weyburn Field, Saskatchewan. *The Leading Edge* **22** (7): 696-697.

20. Dean E.A. 1979. Atmospheric effects on the speed of sound. Technical Report ASL-CR-79-0100-4, Atmospheric Science Laboratory (Aug 1979)

21. Dobrin, M. B. and Savit, C. H. 1988. *Introduction of Geophysical Prospecting.* New York: McGraw-Hill Book Co. page 357-358

22. Domenico, S. N. 1976. Effect of brine-gas mixture on velocity in an unconsolidated sand reservoir. *Geophysics* **41** (5): 882-894.

23. Endres, A., L. and Knight, R. 1989. The effect of microscopic fluid distribution on Elastic wave velocities. *The Log Analyst* **30** (6): 437-445.

24. Fessenden, R.A. 1917. Method and apparatus for locating Ore-bodies. US patent No. 1240328.

25. Gasrcia, J., E. and Pruess, K. 2003. Flow instabilities during injection of CO_2 into saline aquifers. TOUGH symposium 2003. Lawrence Berkeley National Laboratory, California:1-9

26. Gassmann, F. 1951. Uber die Elastizität poröser Medien: Vier. Der Natur. Gesellschaft in Zürich **96**:1-23.

27. Gaus, I., Azaroual, M. and Lauriol, I. C. 2005. Reactive transport modeling of the impact of CO_2 injection on the clayey cap rock at Sleipner (North Sea). *Chemical Geology* **217** (3-4): 319-337.

28. Gupta, N. 2012. Multi-scale characterization of the Woodford shale in west-central Oklahoma: from scanning electron microscope to 3D seismic. PhD thesis, University of Oklahoma, Norman, Oklahoma (April 2012).

29. Han, D. H., Sun, M. and Batzle, M. 2010. CO_2 velocity measurement and models for temperatures up to 200°C and pressures up to 100 MPa. *Geophysics* **75** (3): E123 - E129.

30. Hoffman, R., Xu, X., Batzle, M., Prasad, M., Furre A. K., and Pillitteri, A. 2005. Effective pressure or what is the effect of pressure? *The Leading Edge* 24 (12): 1256-1260.

31. Holm, L.W. and Josendal, V.A. 1974. Mechanism of oil displacement by carbon dioxide. *JPT* **26** (12): 1427-1438.

32. Hornby, B. E. 1996. An experimental investigation of effective stress principles for sedimentary rocks. SEG Expanded Abstracts. 1707- 1710.

33. Hovorka, S. and Tinker, S.W. 2010. EOR as sequestration: Geoscience perspective. The Symposium on the role of enhanced oil recovery in accelerating the deployment of carbon capture and storage, Cambridge, MA, July 23, 2010. GCCC Digital Publication Series #10-12.

34. International Energy Agency (IEA). 2012. Electricity/Heat in United States in 2009, http://www.iea.org/stats/electricitydata.asp?COUNTRY_CODE=US, downloaded 25 January 2012.

35. Jinfeng, M. and Morozov, I. 2010. AVO modeling of pressure-saturation effects in Weyburn CO_2 sequestration. *The Leading Edge* **29** (2): 178-183.

36. Kharaka, Y.K., Cole, D.R., Hovorka, S.D., Gunter, W.D., Knauss, K.G. and Friefeld, B.M. 2006. Gas-water-rock interactions in Frio formation following CO_2 injection: implications for the storage of greenhouse gases in sedimentary basins. *Geology* **34**: 577-580.

37. Kim, J., Matsuoka, T. and Xue, Z. 2011. Monitoring and detecting CO_2 injected into water-saturated sandstone with joint seismic and resistivity measurements. *Exploration Geophysics* **42** (1): 58-68.

38. King M. S. 1966. Wave velocities in rocks as a function of changes in overburden pressure and pore fluid saturants. *Geophysics* **XXXI** (1): 50-73.

39. Knight, R. and Hoeksema, R. N. 1990. A laboratory study of the dependence of elastic wave velocities. *GRL* **17** (10): 1529-1532.

40. Kwon, O., Kronenberg, A. K., Gangi, A. F. and Johnson, B. 2001. Permeability of Wilcox shale and its effective pressure law. *J. Geo. Res.* **106** (B9): 19339-19353.

41. Lumley, D. 2010. 4D seismic monitoring of CO_2 sequestration. *The Leading Edge* **29**(2): 150-155.

42. Lumley, D., Adams, D., Meadows, M., Cole, S. and Ergas, R. 2003. 4D seismic pressure-saturation inversion at Gullfaks field, Norway. *First Break* **21**(9): 3-9.

43. Lumley, D., Adams, D., Wright, R., Markus, D. and Cole, S. 2008. Seismic monitoring of CO_2 geo-sequestration: realistic capabilities and limitations. SEG Las Vegas 2008 Annual meeting: 2841- 2845.

44. Maes, R., Rousseaux, G., Scheid, B., Mishra, M., Colinet, P. and Wit, A. D. 2010. Experimental study of dispersion and miscible viscous fingering of

initially circular samples in Hele-Shaw cells. *AIP-Phy. of Fluids* **22** (12): 123104-1:12.

45. Mohapatra, A., Rai, C. S., Sondergeld, C. H., Richards, T. L. 2012. Seismic signature of CO_2 flooding in Tuscaloosa sandstone. Presented at the 2012 Annual Convention and Exhibition, AAPG Long Beach.

46. Murphy, W. F. 1982. Effect of partial water saturation on attenuation in Massilon sandstone and Vycor porous glass. *J. Acou. Soc.* **71**: 1458-1468.

47. National Energy Technology Laboratory (NETL). 2010. Carbon Dioxide enhanced oil recovery: Untapped domestic energy supply and long term carbon storage solution. US DOE, www.netl.doe.gov

48. Nur, A. and Simmons, G. 1969. The effect of saturation on velocity in low porosity rocks. *Ear. Plan. Sci. Let.* **7**: 183-193.

49. Powell, J. B. 1972. Exploration history of Delhi field, Northeastern Louisiana. In Stratigraphic oil and gas fields, ed. R. E. King. AAPG Memoir no. 16: 548-559.

50. Prasad, M. and Manghnani, M. H. 1997. Effects of pore and differential pressure on compressional wave velocity and quality factor in Berea and Michigan sandstones. *Geophysics* **62** (4): 1163-1176.

51. Richards, T. 2011. Lessons from 4D seismic monitoring of CO_2 injection at the Delhi field. *first break* **29**: 89-94.

52. Robin, P. Y. F. 1973. Note on effective pressure. *J. Geo. Res.* **78** (14): 2434-2437.

53. Shakhashiri, B. Z. 2008. Chemical of the Week, Carbon Dioxide, CO_2. University of Wisconsin-Madison. http://scifun.chem.wisc.edu/chemweek/pdf/CarbonDioxide.pdf (downloaded 7 September 2011)

54. Siggins, A. F. and Dewhurst, D. N. 2003. Saturation, pore pressure and effective stress from sandstone acoustic properties. *GRL* **30** (2).

55. Smith, T. M., Sondergeld, C. H. and Rai, C. S. 2003. Gassmann fluid substitutions: A tuitorial. *Geophysics* **68** (2): 430-440.

56. Sondergeld, C. H., and Rai, C. S. 1993. A new exploration tool: Quantitative core characterization. *Pageoph* **141**, 249–268.

57. Tinni, A., Sondergeld, C. H., Rai, C., and Simo, H. 2011. Effective pressure and microstructure control on resistivity formation factor and seismic waves velocities, SPE 147432, Presented at Annual Technical Conference and Exhibition, Denver, Colorado, 30 Oct-2 Nov.

58. Thakur, G.C. 1996. What is Reservoir Management? *JPT* **48** (6): 520-525.

59. The Environmental Integrity Project (EIP). 2011. Getting Warmer: US CO_2 Emissions from Power Plants Emissions Rise 5.6% in 2010. http://www.environmentalintegrity.org/documents/CO2Report_2011RJD21811final.pdf , 18 February 2011.

60. Todd, T. and Simmons, G. 1972. Effect of pore pressure on the velocity of Compressional waves in low porosity rocks. *JGR* **77** (20): 3731-3743.

61. Urosevic, M., Pevzner, R., Kepic, A., and Wisman, P. 2010. Time-lapse seismic monitoring of CO_2 injection into a depleted gas reservoir Naylor Field, Australia. *The Leading Edge* **29**(2): 164-169.

62. US DOE. 2011. Stripper Well Revitalization. Fossil Energy office of communication, http://www.fossil.energy.gov/programs/oilgas/marginalwells/oil_stripper_wells_2010.pdf.

63. Vanorio, T., Mavko, G., Vialle, S. and Spratt, K. 2010. The rock physics basis for 4D seismic monitoring of CO_2 fate: Are we there yet? *The Leading Edge* **29** (2): 156-162.

64. Wang, Z. and Nur, A. M. 1982. Effects of CO_2 flooding on wave velocities in rocks with hydrocarbons. *SPE* **4** (4): 429-436.

65. White, D. 2009. Monitoring CO_2 storage during EOR at the Weyburn-Midale Field. *The Leading Edge* 28 (7): 838-842.

66. White, C.M., Strazisar, B.R., Granite, E.J., Hoffman, J.S., and Pennline, H.W. 2003. Separation and capture of CO_2 from large stationary sources and sequestration in geological formations— Coalbeds and deep saline aquifers: *J. of the Air and Waste Man. Ass.* **53**: 645–715.

67. Whorten, L.P., Brownscombe, E.R., Dyes, A.B. 1952. Method for producing oil by means of carbon dioxide. US patent No. 2623596.

68. Wightman, W. E., Jalinoos, F., Sirles, P., and Hanna, K. 2003. Application of Geophysical Methods to Highway Related Problems. *Federal Highway Administration*, Lakewood, CO. http://www.epa.gov/esd/cmb/GeophysicsWebsite/pages/reference/methods/Surface_Geophysical_Methods/Seismic_Methods/Seismic_Reflection_Methods.htm

69. Worden, R.H. and Barclay, S.A. 2000. Internally-sourced quartz cement due to externally-derived CO_2 in sub-arkosic sandstones, North Sea. *J. Geo Exp.* **69-70**: 645-649. http://dx.doi.org/10.1016/S0375-6742(00)00104-7.

70. Winkler, K. W. 1986. Estimates of velocity dispersion between seismic and ultrasonic frequencies. *Geophysics* **51** (1): 183-189.

71. Wyllie, M. R. J., Gregory, A. R., and Gardner, L. W. 1956. Elastic wave velocities in heterogeneous and porous media. *Geophysics* **XXI** (1): 41-70.

72. Xue, Z. and Ohsumi, T. 2004 Seismic wave monitoring of CO_2 migration in water-saturated porous sandstone. *Exploration Geophysics* **7** (1): 25 – 32.

Nomenclature

C = Concentration of the minerals

f = Volumetric concentration of minerals

G = Shear modulus of the rock, Gpa

I_c = Impedance values in oil saturated rock flooded with CO_2, km.gm/cc/sec

I_{co} = Impedance values in CO_2 saturated rock (with irreducible water and oil), km.gm/cc/sec

I_o = Impedance values in oil saturated rock with irreducible water, km.gm/cc/sec

K = Bulk modulus of a component, GPa

K_{dry} = Dry bulk modulus of the rock, GPa

K_e = Effective bulk modulus of the rock, GPa

K_f = Fluid bulk modulus of the fluid, GPa

K_g = Grain bulk modulus, GPa

K_{isat} = Bulk modulus of rock saturated with fluid i, GPa

K_m = Mineral bulk modulus, GPa

K_{Ruess} = Ruess average of the components, GPa

K_{VRH} = Voigt-Ruess-Hill average of the mineral components, GPa

K_{Voigt} = Voigt average of the components, GPa

n = Biot effective stress coefficient

P_c = Confining Pressure, GPa

P_d = Differential Pressure, GPa

P_e = Effective Pressure, GPa

P_p = Pore Pressure, GPa

φ = Porosity

ρ_{bulk} = Bulk density, g/cc

ρ_{CO2} = Carbon dioxide density, g/cc

ρ_f = Fluid density, g/cc

ρ_g = Grain density, g/cc

ρ_o = Oil density, g/cc

ρ_w = Water density, g/cc

ρ_1 = density of the top layer, g/cc

ρ_2 = density of the bottom layer, g/cc

r = Slope between impedance saturation relationships, km.gm/cc/sec

R = Reflection coefficient

S = concentration of fluid

S_o = Saturation of oil (with irreducible water saturation), fraction

S_{CO2} = Saturation of Carbon dioxide, fraction

S_w = Saturation of water, fraction

v_b = Bulk volume, cc

v_g = Grain volume, cc

v_p = Pore volume, cc

V_p = Compressional wave velocity, km/sec

V_s = Shear wave velocity, km/sec

V_1 = velocity in the top layer, km/sec

V_2 = velocity in the bottom layer, km/sec

Z_1 = acoustic impedance for top layer, km.g/cc/sec

Z_2 = acoustic impedance for bottom layer, km.g/cc/sec

Appendix A

Velocity Equilibrium study on coal and shale:

Velocity equilibrium study was performed on coal and shale samples similar to fused glass beads and Berea sandstone. The P and S wave velocity (Fig A.1) were measured as a function of time across sample saturated with gaseous and liquid CO_2.

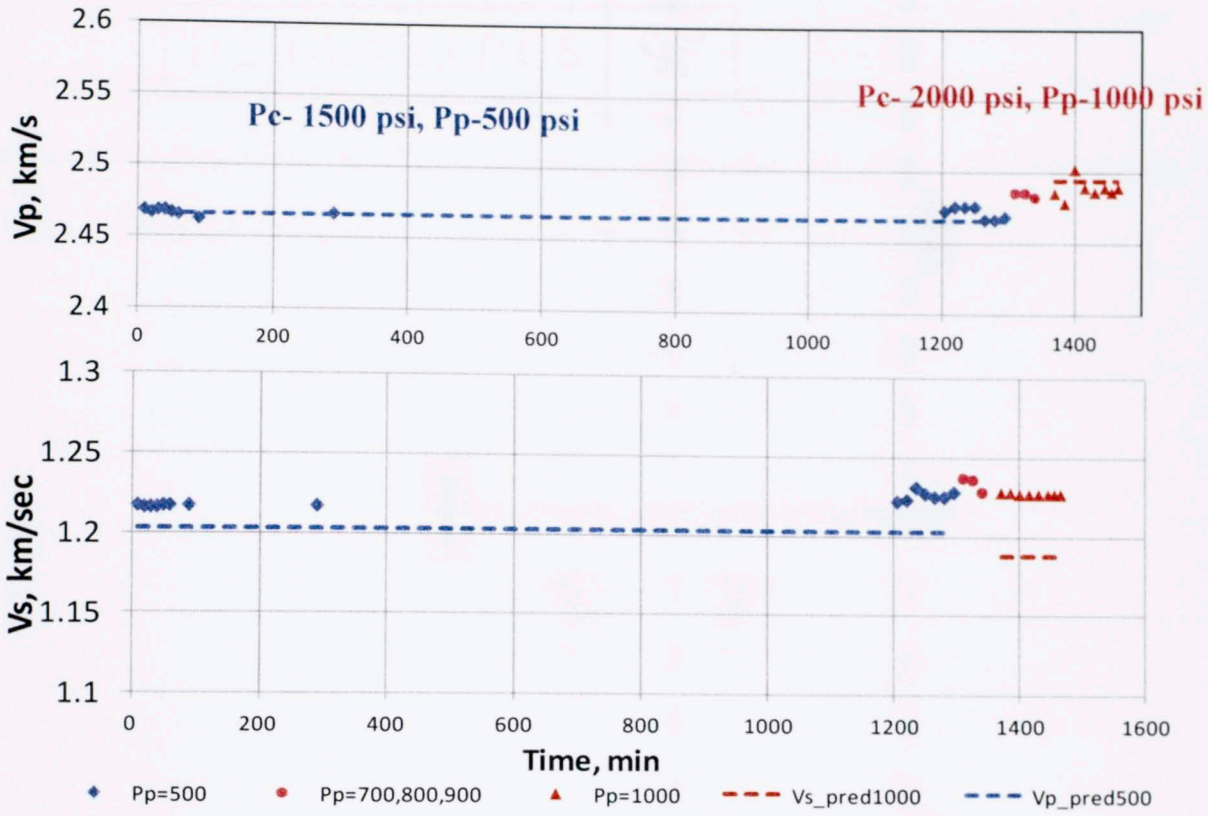

Figure A.0.1 Measured V_p and V_s equilibrating with gaseous CO_2 (blue) and liquid state CO_2 (red) in coal. The V_p and V_s, shown with dotted line, are predicted from dry measurements.

The time required for gaseous CO_2 to stabilize in the pore spaces of coal remains undetermined as I observe some perturbations after 1200 minutes. The reason behind such behavior may be due to the dual porosity that exists in coal. CO_2 initially fills up the pore spaces in cleats and then gets adsorbed in the surfaces after sometime.

The second observation is the increase in Vp after CO_2 phase change. This increase is predicted reasonably by Biot-Gassmann theory. Coal has a low bulk modulus (~5 GPa), low grain density (~1.35) and a low porosity (5%). Therefore, V_p is more sensitive to change in bulk modulus.

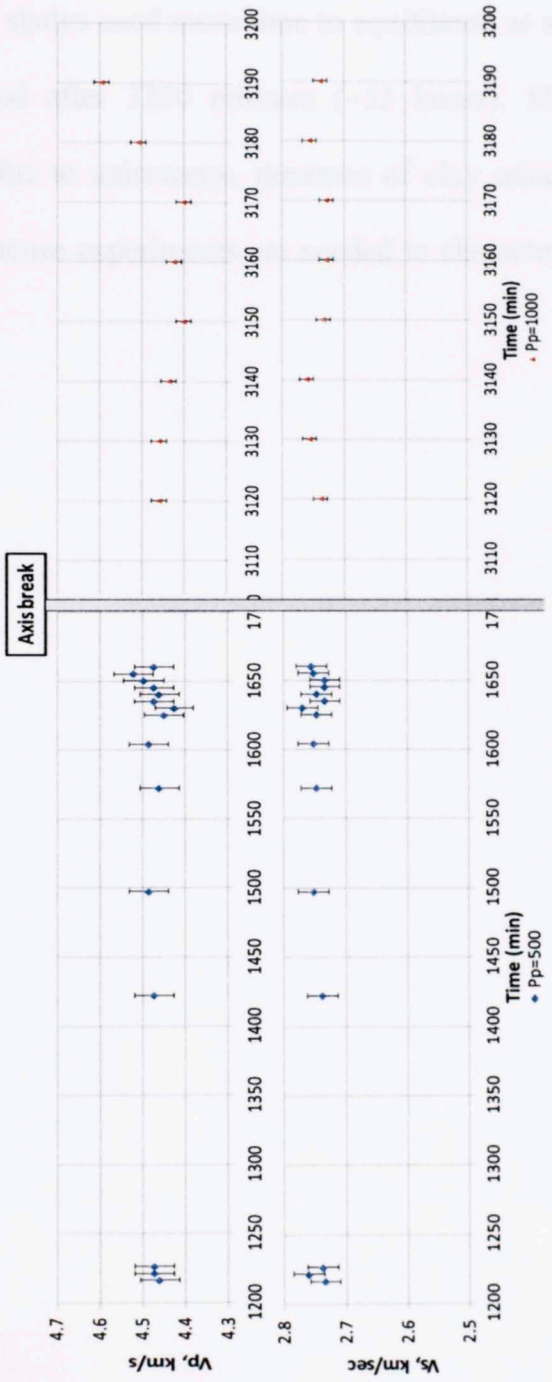

Figure A.0.2: Measured P (i) and S (ii) wave velocity equilibrating with gaseous CO_2 (blue) and liquid state CO_2 (red) in Woodford shale

Shales are high in total organic content (TOC) and this shale has 40% TOC (Gupta, 2012). Fig A.2 shows measured Vp and Vs recorded with time at confining and pore pressure same as mentioned in sec 3.5.1. An increasing trend is observed in P velocity when sample is saturated with gaseous and liquid CO_2. This increase is steeper when pore fluid is liquid CO_2. Thus, shales need more time to equilibrate as seen in Fig A.2. The measurements are stopped after 3200 minutes (~53 hours). Shales are more complicated than sandstones due to anisotropy, presence of clay minerals, TOC and adsorption. Therefore, more intense experiments are needed to characterize its velocity behavior with CO_2 flooding.